

REPORT DOCUMENTATION PAGE

AFRL-SR-BL-TR-98-

ved  
1-0188

Public reporting burden for this collection of information is estimated to average 1 hour per response and maintaining the data needed, and completing and reviewing the collection of information. Send information, including suggestions for reducing this burden, to Washington Headquarters Services, Directorate for Information Operations and Reports, 1204, Arlington, VA 22202-4302, and to the Office of Management and Budget, Paperwork Reduction Project (0704-0188) Washington, DC 20503.

0378

sources, gathering  
of this collection of  
Davis Highway, Suite

1. AGENCY USE ONLY (Leave Blank)		2. REPORT DATE August 1996	3. REPORT TYPE AND DATES COVERED Final	
4. TITLE AND SUBTITLE Large Static and Dynamic Deformation of Beams: The Inverse Problem			5. FUNDING NUMBERS	
6. AUTHORS Matilda Wilson McVay				
7. PERFORMING ORGANIZATION NAME(S) AND ADDRESS(ES) Texas A&M University			8. PERFORMING ORGANIZATION REPORT NUMBER	
9. SPONSORING/MONITORING AGENCY NAME(S) AND ADDRESS(ES) AFOSR/NI 110 Duncan Avenue, Room B-115 Bolling Air Force Base, DC 20332-8080			10. SPONSORING/MONITORING AGENCY REPORT NUMBER	
11. SUPPLEMENTARY NOTES				
12a. DISTRIBUTION AVAILABILITY STATEMENT Approved for Public Release			12b. DISTRIBUTION CODE	
13. ABSTRACT (Maximum 200 words) See attached.				

19980505 143

This Document Contains Missing Page/s That Are Unavailable In The Original Document

OFFICE OF TECHNICAL SERVICES

14. SUBJECT TERMS			15. NUMBER OF PAGES	
			16. PRICE CODE	
17. SECURITY CLASSIFICATION OF REPORT Unclassified	18. SECURITY CLASSIFICATION OF THIS PAGE Unclassified	19. SECURITY CLASSIFICATION OF ABSTRACT Unclassified	20. LIMITATION OF ABSTRACT UL	

0378

**LARGE STATIC AND DYNAMIC DEFORMATION OF BEAMS:**

**THE INVERSE PROBLEM**

A Dissertation

by

MATILDA WILSON MCVAY

Submitted to the Office of Graduate Studies of  
Texas A&M University  
in partial fulfillment of the requirements for the degree of

DOCTOR OF PHILOSOPHY

August 1996

Major Subject: Aerospace Engineering

LARGE STATIC AND DYNAMIC DEFORMATION OF BEAMS:  
THE INVERSE PROBLEM

A Dissertation

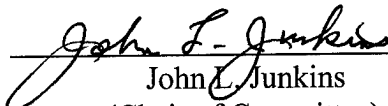
by

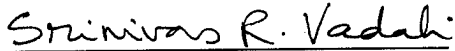
Matilda Wilson McVay

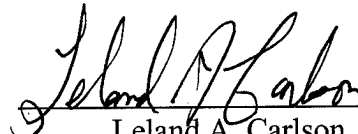
Submitted to the Office of Graduate Studies of  
Texas A&M University  
in partial fulfillment of the requirements for the degree of


DOCTOR OF PHILOSOPHY

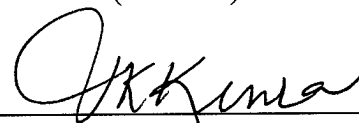
Approved as to style and content by:

  
John L. Junkins  
(Chair of Committee)

  
Srinivas R. Vadali  
(Member)

  
Leland A. Carlson  
(Member)

  
Richard M. Alexander  
(Member)

  
Donald T. Ward  
(Head of Department)

August 1996

Major Subject: Aerospace Engineering

**ABSTRACT**

Large Static and Dynamic Deformation of Beams:

The Inverse Problem. (August 1996)

Matilda Wilson McVay, B.S., Colorado School of Mines;

M.S., Texas A&M University

Chair of Advisory Committee: Dr. John L. Junkins

The primary objective of this study is to establish a methodology for validating a dynamical model of a flexible two beam system undergoing large deformations.

This dissertation presents a systematic approach for using a series of experiments to estimate mathematical model parameters and correct them to match the measured response. The study of any dynamical system has a natural partition between the kinetic energy terms and the potential energy terms. By using this natural partition to design a sequence of experiments, it is shown that the number of unknown parameters affecting the system response for any given experiment is greatly reduced. First, a set of static deformations are used to determine beam parameters such as the stiffness coefficients and allow modeling of nonlinear effects. Then, free response experiments are used to determine some motion parameters such as the mass per unit length of each beam and the parameters associated with natural environmental forces such as friction effects. This separation of static and free response measurements allows the recovery of model parameters without being corrupted by other forced system model errors such as joint dynamics and motor modeling which are present in a full dynamic response. A set of dynamic forced response experiments are used to determine motor parameters which model the inputs to the structure. Appropriate statistical estimation methods are utilized to forward propagate *a priori* and measurement covariance estimates through the sequence of nonlinear estimation processes.

Before the parameters can be updated, a novel mathematical model of the system is developed and verified based on an arc length approach to beam deflections. This model accounts for large deformation effects such as foreshortening and is used in the static analysis. A nonlinear finite element model is developed to allow modeling of the free vibration and forced vibration response. This model also allows large deformations of the beam system by defining the deformation of a point in terms of an axial displacement and a transverse displacement. Although it is a computationally intensive program, it yields accurate results and is well suited to the estimation of parameters affecting the dynamic motion.

## ACKNOWLEDGEMENTS

I would like to thank Dr. John L. Junkins, my advisory committee chairman, for all of his guidance and support during my graduate studies. His sense of humor and positive attitude have made these years enjoyable and I admire his breadth of knowledge and communication skills. I would also like to thank Dr. Srinivas R. Vadali, Dr. Leland A. Carlson and Dr. Richard M. Alexander for their service as members of my advisory committee. Appreciation is also extended to Dr. Oliver G. Aberth for his service as my graduate council representative.

I am grateful for the financial support of my graduate education given by the United States Air Force through the USAF Laboratory Graduate Fellowship Program. I am also grateful for the financial support provided by a Department of Education funded fellowship administered by Dr. Karan Watson.

I am especially grateful to my family for their encouragement and support of my graduate studies. The encouragement, support and love from my husband Duane has helped me during my course work and through the completion of this dissertation. My mother and father have inspired me and helped me persevere through everything. I am also very grateful to my three children for their patience, understanding and love.

## TABLE OF CONTENTS

	Page
ABSTRACT .....	iii
ACKNOWLEDGEMENTS.....	v
TABLE OF CONTENTS.....	vi
LIST OF TABLES .....	viii
LIST OF FIGURES .....	ix
 CHAPTER	
I INTRODUCTION.....	1
1.1 Motivation.....	1
1.2 Dissertation Outline .....	3
II LITERATURE REVIEW .....	4
III NONLINEAR STATIC ANALYSIS .....	10
3.1 Model Development - Arc Length Approach .....	10
3.1.1 Model Validation.....	14
3.1.2 Application to Two Beam Model.....	16
3.1.3 Wire Constraint Experiment.....	19
3.1.4 Boundary Value Problem .....	23
3.1.5 Simulations.....	27
3.2 Static Parameter Estimation.....	30
3.2.1 Least Squares Estimation .....	31
3.2.2 Results - Static Deformation Parameters.....	39
IV NONLINEAR FREE VIBRATION ANALYSIS .....	43
4.1 Model Development .....	43
4.1.1 Arc Length Approach.....	43
4.1.2 Finite Element Approach.....	44
4.1.3 Model Validation.....	57
4.1.4 Model Refinement.....	68
4.1.5 Simulations.....	77
4.2 Free Vibration Parameter Estimation .....	81
4.2.1 Least Squares Estimation .....	82
4.2.2 Results - Free Vibration Parameters.....	88

	Page
CHAPTER	
V NONLINEAR FORCED VIBRATION ANALYSIS .....	97
5.1 Development.....	97
5.1.1 Motor Modeling .....	97
5.1.2 Model Validation.....	99
5.1.3 Simulations.....	99
5.2 Forced Vibration Parameter Estimation .....	102
5.2.1 Least Squares Estimation .....	103
5.2.2 Results - Forced Vibration Parameters.....	107
VI CONCLUSIONS .....	109
REFERENCES .....	112
VITA.....	114



## LIST OF TABLES

	Page
Table 1. Material properties for PACE.....	2
Table 2. Material nonlinearity results .....	29
Table 3. Parameter recovery for wire constraint.....	39
Table 4. Parameter recovery for directed force.....	40
Table 5. Parameter recovery for directed force with measurement errors.....	41
Table 6. Axial strain comparison.....	62
Table 7. Linear model natural frequencies .....	64
Table 8. Transverse tip deflections at given time intervals .....	65
Table 9. Natural frequencies for $w$ modes .....	70
Table 10. Natural frequencies for $u$ modes.....	71
Table 11. Beam deflection for tip moment = 18.0.....	71
Table 12. Beam deflection for transverse tip force = 8.0.....	72
Table 13. Energy balance for a period .....	81
Table 14. Parameter recovery for perfect measurements.....	89
Table 15. Parameter recovery over 1/4 cycle with measurement errors .....	90
Table 16. Parameter recovery over 1/2 cycle with measurement errors .....	91
Table 17. Effects of parameter values on tip transverse deflections.....	92
Table 18. Parameter recovery with <i>a priori</i> information.....	94
Table 19. Friction coefficient recovery with <i>a priori</i> information .....	95
Table 20. Friction coefficient recovery with larger <i>a priori</i> variance.....	95
Table 21. Effects of <i>a priori</i> determined friction parameters .....	96
Table 22. Recovery of torque constant ratio.....	107
Table 23. Recovery of ratio with measurement errors.....	108

## LIST OF FIGURES

	Page
Figure 1. Planar Articulating Controls Experimental test article.....	2
Figure 2. Foreshortening due to transverse displacement.....	6
Figure 3. Transverse displacement in arc length coordinates .....	10
Figure 4. Element freebody diagram.....	11
Figure 5. Comparison of cantilever beam deflections from tip weights.....	15
Figure 6. Deflection of cantilever beam due to tip moment .....	16
Figure 7. Two beam configuration.....	17
Figure 8. Radial wire constraint.....	21
Figure 9. Effect of wire constraint length .....	27
Figure 10. Effect of material nonlinearity.....	28
Figure 11. Deformation shapes for series of transverse forces .....	30
Figure 12. Finite element variables.....	45
Figure 13. Element, node and displacement numbering.....	49
Figure 14. Comparison of deflections due to tip moment .....	58
Figure 15. Finite element solutions for tip force .....	60
Figure 16. Comparison of methods for tip loading.....	61
Figure 17. Free vibration comparison of methods.....	66
Figure 18. Beam shapes for truncated and full order models .....	74
Figure 19. Rotational inertia effects .....	77
Figure 20. Tip transverse deflection over a period .....	78
Figure 21. Tip longitudinal deflection over a period .....	79
Figure 22. Beam profiles for 1/4 period.....	80
Figure 23. Effect of gain values on tip transverse displacements.....	100
Figure 24. Effect of gain values on tip longitudinal displacements.....	101
Figure 25. Control and tip displacements for control gain of 0.2.....	102

## CHAPTER I

### INTRODUCTION

#### 1.1 Motivation

Most of the parameters involved in a mathematical model of a dynamical system can be naturally grouped into three major subsets. The first logical subset would include parameters affecting the storage of potential energy which can be estimated from a family of static measurements on the system displacements. The second subset would include inertia type parameters which affect the free response of the system to prescribed initial conditions. These could be found by deforming the structure to a measured static shape and releasing the constraining force and measuring the free response of the system. The third subset would contain the actuator model parameters which could be found from a set of forced response experiments. This parameterization reduces the number of poorly known parameters to be determined from each identification experiment and typically improves observability. For high dimensioned nonlinear systems, the approach would seem likely to greatly enhance convergence. These qualitative ideas are the basis for the methodology studied in this dissertation.

These ideas are studied in the context of large deformations of a two beam system that is similar to the flexible manipulator arm developed at the United States Air Force (USAF) Phillips Laboratory called the Planar Articulating Controls Experiment (PACE)<sup>1</sup>. This structure, illustrated in Figure 1, consists of two flexible beams connected to each other by an elbow joint and mounted to an air bearing table by a shoulder hub. The primary beam material properties and the tip and elbow mass properties are listed in Table 1. The structure is constrained to move horizontally along a polished granite table. Air bearings are used to greatly reduce the friction forces between the table and the support

---

This dissertation follows the style and format of the AIAA *Journal of Guidance, Control and Dynamics*.

plates. PACE is designed to experimentally test control theories and validate nonlinear structural modeling techniques. A similar structure is being developed in the Dynamics and Controls Laboratory of the Aerospace Engineering Department at Texas A&M University.

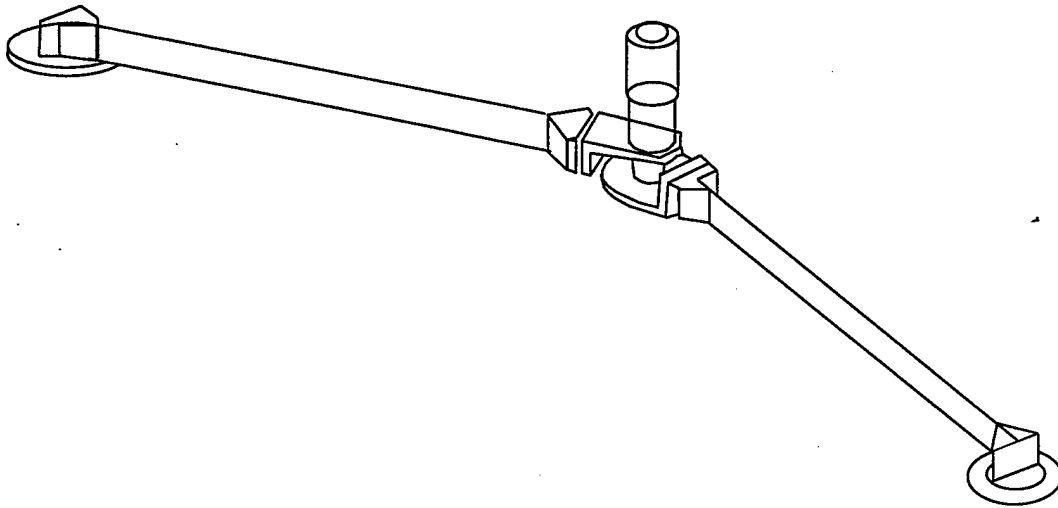


**Figure 1. Planar Articulating Controls Experimental test article**

<b>Table 1. Material properties for PACE</b>	
<b>Beam 1</b>	<b>Beam 2</b>
L=0.776 m	L=0.714 m
EI=11.413 N·m <sup>2</sup>	EI=11.275 N·m <sup>2</sup>
$\rho$ =0.532 kg/m	$\rho$ =0.530 kg/m
Elbow mass=4.280 kg	Tip mass=1.038 kg
Elbow inertia=122.982E-4 kg·m <sup>2</sup>	Tip inertia=15.244E-4 kg·m <sup>2</sup>

## 1.2 Dissertation Outline

This dissertation begins in Chapter II with a review of the literature for the modeling of large deformations, with a specific focus on two beam systems. The next three chapters correspond to three divisions of the system identification process into the static, free vibration, and forced response analysis. Each chapter is divided into two main sections. The first section develops the mathematical model for simulating the response and the second section develops the parameter estimation technique. Some highlights of each chapter are discussed. Chapter III develops a new approach to the nonlinear static beam flexure problem. This model is used in estimating the beam parameters that affect the potential energy by using a series of simple static experiments designed to deform the system using a wire constraint force. An unusual application of the implicit function theorem is used in this recovery process. Chapter IV develops and validates a nonlinear finite element model for the dynamic analysis of the system. This model is used to estimate the parameters contributing to the free response of the system upon release of the force applied by the wire. Chapter V develops the additions to the mathematical model for including a motor in the dynamic response and recovers the motor parameters. A method is presented for propagating the estimated parameters and associated errors forward through each level of parameter estimation. Finally, Chapter VI presents the conclusions of the system modeling and parameter estimation technique studied in this dissertation.

## CHAPTER II

### LITERATURE REVIEW

As a specific example, this research considers the PACE flexible multibody configuration shown in Figure 1. We are interested in the "forward" problem of mathematical modeling such systems, and the "inverse" problem of estimating model parameters from response measurements.

Kwak and Meirovitch<sup>2</sup> employ Lagrange's equations in terms of general quasicordinates to develop models for multibody systems. In this approach, the equations of motion for each individual flexible body are derived in terms of quasicordinates. A recursive kinematic description of the velocity vector of a point in each body in a multibody chain is expressed in terms of the velocity vector of the preceding body in the chain. The set of equations are assembled globally using the kinematical relationships and the redundant coordinates are eliminated. The resulting equations consist of nonlinear ordinary differential equations describing translations and rotations and partial differential equations describing elastic motions. The elastic displacements are discretized using a finite element method to approximate the solution of partial differential equations using a finite system of ordinary differential equations. Kwak and Meirovitch developed a perturbation approach to control this high order nonlinear system. The perturbation approach assumes the rigid body motions are large compared to the elastic motions allowing the problem to be separated into two parts. The problem is divided into a low dimensional set of nonlinear zero order equations for rigid body motion and first order linear equations of high dimensionality for elastic motions.

A similar structure to PACE is studied by Meirovitch and Lim<sup>3</sup>. It consists of two hinge connected flexible arms with one end mounted on a rigid platform and the other rigid end holding a payload. The equations of motion for this system are derived using the standard Lagrange's equations. The partial differential equations describing the elastic

motions are discretized using a Ritz type approach using shape functions called quasi-comparison functions. Quasi-comparison functions are linear combinations of admissible functions and in this case are linear combinations of clamped-free and clamped-clamped shape functions. Essentially the same perturbation approach is used to separate the problem into a zero order problem for rigid body maneuvering and a first order problem for the control of elastic motion. The elastic motions are assumed to be small in this study as well.

The large deformation of beams has been studied extensively by D.H. Hodges for use in rotorcraft applications. In one study, Hinnant and Hodges<sup>4</sup> modeled a constitutive nonlinear effect on static deformations. They analyzed actual experimental data for a cantilever beam undergoing large deformations. One part of the experiment consisted of measuring the static deformation of a uniform cantilever beam with a mass attached to the tip. The static behavior of the beam is sensitive to the value of the stiffness coefficient and the classical linear model gave incorrect results. When the beam deformations are large, the linear theory is typically too soft. To account for material nonlinear effects, a simple nonlinear planar elastic model is used which introduced a large deformation material nonlinearity coefficient  $\alpha$ . The strain energy with this model is:

$$U = \frac{1}{2} E (I_2 \kappa^2 + I_4 \alpha \kappa^4 / 2) \quad (1)$$

where  $\kappa$  is the planar curvature of the beam and  $I_2$  and  $I_4$  are area moments of inertia for flatwise transverse deflection:

$$I_2 = bt^3 / 12 \quad (2)$$

$$I_4 = bt^5 / 80 \quad (3)$$

In another study published by Hodges<sup>5</sup> the curvature of beams undergoing large deformations is examined. He developed a formulation which accounted for the effective shortening of a beam due to transverse deflections. Figure 2 shows the foreshortening effect where the distance  $x$  is to a point on the beam before deformation and the distance  $\bar{x}$  is the same point after deformation.

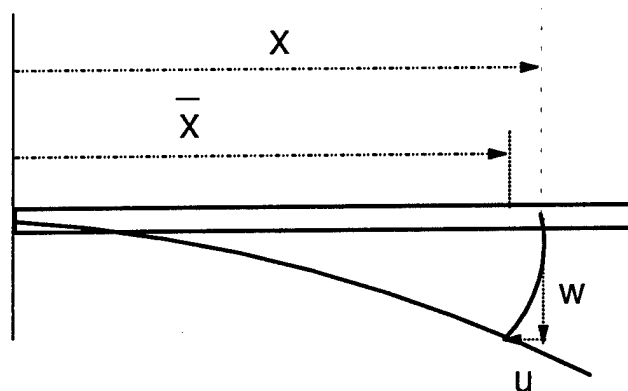


**Figure 2. Foreshortening due to transverse displacement**

The expression for curvature he derived is:

$$\kappa = \frac{\frac{d^2 w}{dx^2}}{\sqrt{1 - \left(\frac{dw}{dx}\right)^2}} \quad (4)$$

This formula is exact for an elastic beam undergoing a planar deflection with small axial strain compared to unity and is valid for any size deformation.

Monasa and Lewis<sup>6</sup> also studied the large deformation behavior of beams. They included the geometric nonlinear effect due to the curvature of the beam but used a different expression for curvature which is frequently found in some calculus texts<sup>7</sup>:



$$\kappa = \frac{\frac{d^2 w}{dx^2}}{\left(1 + \left(\frac{dw}{dx}\right)^2\right)^{3/2}} \quad (5)$$

The coefficient of the nonlinear term in Eq. (5) is of opposite sign and the denominator is of higher order than the terms in Eq. (4). This difference is due to the fact that in the formulation of Eq. (5),  $x$  is defined as the distance along the deformed curve whereas in Eq. (4),  $x$  is measured along the original position of the beam. The curvature formula, Eq. (5), must be corrected when applied to the physical beam curvature for the shortened value of  $x$  due to the deflection  $w$ . The authors used an iterative process to adjust the deflection  $w$  and the  $u$  change in  $x$ . First they assumed small loads and no shortening and solved for the deflection  $w$  using Eq. (5) and the moment curvature relationship and corrected the change  $u$  using the arc length formula. The calculations are repeated until the solution converged on  $u$ . Then the loads are gradually increased and the iterative process repeated for each step until the final load is reached. The curvature formula caused a further problem during the Runge-Kutta integration of Eq. (5) and the moment curvature expression. The limits of integration over the beam,  $x_i$  and  $x_{i+1}$ , are functions of the beam deformation and unknown.

Reddy and Singh<sup>8</sup> used the same definition of curvature (Eq. 5) in their study of large deflection and free vibration behaviors of elastic beams. It does not appear they accounted for the foreshortened value of  $x$  in their solution. They compared two finite element solutions of the differential equations of motion and solved a number of beam problems with various boundary conditions. They used a conventional finite element method which used cubic interpolating functions to approximate axial displacement, transverse displacement and slope. They also use a finite element method called a mixed method which is based on including the bending moment with the deflections  $u$  and  $w$  as the dependent variables. By using the bending moment as a variable, the order of the

differential equation is reduced and therefore linear polynomials could be used to approximate the transverse deflection instead of cubic polynomials. They compared the results of their methods to several analytic and numeric solutions of single beams with various boundary conditions.

Epstein and Murray<sup>9</sup> defined the deformation of a beam using two variables, axial displacement  $u$  and transverse displacement  $w$ . They derived the following expression for the physical curvature of the beam which is used for large deformations and axial strains:

$$\kappa = \left(1 + \frac{du}{dx}\right) \left(\frac{d^2w}{dx^2}\right) - \left(\frac{dw}{dx}\right) \left(\frac{d^2u}{dx^2}\right) \quad (6)$$

They developed the equations of motion for the beam deformation using the principle of virtual work. They discretized the displacements  $u$  and  $w$  using a finite element approach with cubic interpolating functions. They verified their formulation worked for large deformations by computing the displacements from a thin cantilever strip bent by a moment into a complete circle and comparing the results to the exact solution. They only developed the equations for the static deformation of the beam.

Several methods for solving static and dynamic responses with large deformations of single beams has been discussed with various ways of accounting for geometric (foreshortening) and constitutive nonlinear effects. The modeling of two beam systems have typically not included these effects. A new approach is developed in this dissertation to model large deformation and nonlinear effects on a flexible two beam system and this model is used to recover some of the beam parameters. This methodology can be generalized for use in other studies based upon these developments.

First an alternative approach for solving large static deformations of beams is developed. This approach accounts for the foreshortening of beams in a manner consistent

with the exact curvature relationships of Hodges Eq. (4) and Epstein and Murray Eq. (6). However, this approach leads to a new nonlinear differential equation model and an associated method for solving the resulting two point boundary value problem. Next a nonlinear finite element model is developed for solving the free vibration and dynamic response of the beam system. The beam parameters affecting the deformation shapes are recovered separately for the static, free response and dynamic response of the system.

## CHAPTER III

### NONLINEAR STATIC ANALYSIS

The static analysis of beam deformation would be the first logical step in isolating beam properties. Beam parameters such as the stiffness coefficient and parameterization of the material nonlinear effects can be recovered. A mathematical model of the system must be developed before an algorithm can be posed for recovering the beam parameters. For the static analysis, a new approach for solving large beam deformations is developed.

#### 3.1 Model Development - Arc Length Approach

A novel coordinate system is used to develop the equation of motion for an elastic beam undergoing transverse vibration. This approach is designed to accommodate geometric nonlinearities associated with large deformations. In the conventional analysis the deformation is expressed by defining the transverse displacement at a point  $x$  by  $w(x,t)$  and  $u(x,t)$  shown in Figure 2. In the approach of this dissertation, arc length  $s$  is used as the independent distance coordinate and the slope angle  $\Psi(s,t)$  is used as the instantaneous generalized coordinate shown in Figure 3.

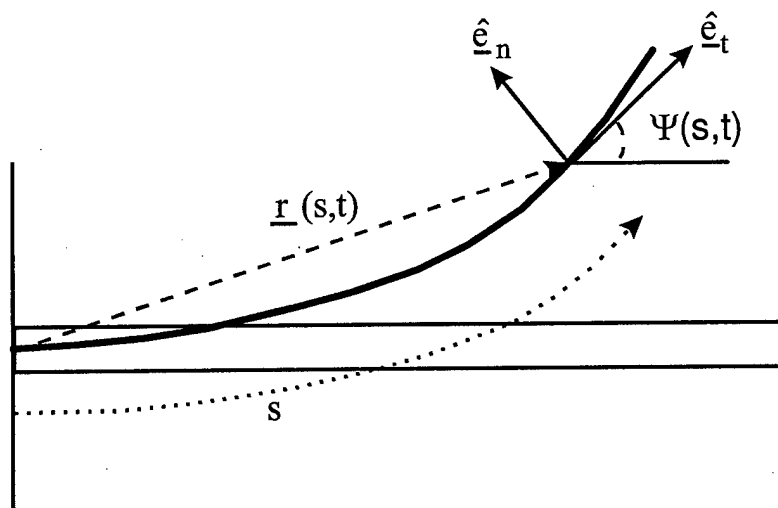


Figure 3. Transverse displacement in arc length coordinates

The arc length is the distance measured along the instantaneous deformation curve from the origin and  $\Psi(s,t)$  is the angle of the local tangent vector  $\hat{e}_t$ . The vector  $\underline{r}(s,t)$  is the inertial position of a typical mass element. A tangent and normal vector is defined at each point along the curve. Figure 4 shows the free body diagram for a beam element of length  $ds$ .

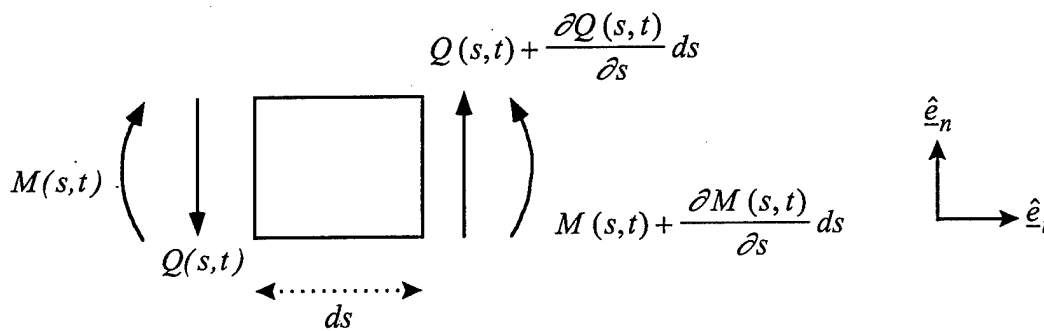


Figure 4. Element freebody diagram

The normal force equation of motion for this element is

$$\left[ Q(s,t) + \frac{\partial Q(s,t)}{\partial s} ds \right] - Q(s,t) = m(s) ds \frac{\partial^2 \underline{r}(s,t)}{\partial t^2} \cdot \hat{e}_n \quad (7)$$

and the moment equation of motion is

$$\left[ M(s,t) + \frac{\partial M(s,t)}{\partial s} ds \right] - M(s,t) + \left[ Q(s,t) + \frac{\partial Q(s,t)}{\partial s} ds \right] ds = I(s) \frac{\partial^2 \Psi(s,t)}{\partial t^2} ds \quad (8)$$

In the statics case, Eq. (7) can be reduced to

$$\frac{\partial Q(s,t)}{\partial s} = 0 \quad (9)$$

and by ignoring second order terms and rotatory inertia  $I(s)$ , Eq. (8) can be reduced to the familiar result

$$Q(s,t) = -\frac{\partial M(s,t)}{\partial s} \quad (10)$$

The bending moment can be related to the curvature of the beam by the Euler Bernoulli constitutive model

$$M(s,t) = EI(s) \frac{1}{\beta(s,t)} \quad \text{where } \beta \text{ is the local radius of curvature} \quad (11)$$

From calculus<sup>7</sup>, the curvature at a point on a curve is the derivative of the tangent angle  $\Psi(s,t)$  with respect to the arc length  $s$ . For the statics case, the angle is denoted as  $\Psi(s)$  and the curvature is the reciprocal of  $\beta$ .

$$\frac{1}{\beta} = \frac{d\Psi(s)}{ds} \quad (12)$$

In the developments that follow, no small deformation approximations are used. This exact curvature formula is combined with Eq. (9) - Eq. (11) to yield the elegantly simple, exact differential equation for the static deformation of an Euler Bernoulli beam

$$\frac{d}{ds} \left( EI \frac{d^2\Psi(s)}{ds^2} \right) = 0 \quad (13)$$

The (x,y) shape of the beam is obtained by solving the exact geometric differential equations

$$\frac{dy(s)}{ds} = \sin(\Psi(s)) \quad (14)$$

$$\frac{dx(s)}{ds} = \cos(\Psi(s)) \quad (15)$$

The choice of  $\Psi$  as the dependent variable and  $s$  as the independent variable has two advantages. The first is the "foreshortening" of the beam is automatically and exactly accounted for. This allows large deformations without having to introduce approximate corrections in the length of the beam, and furthermore, simplifies the numerical integration since the arc length is varied between zero and the length of the beam regardless of the projected  $x$  direction length. The second advantage is that it allows the Euler Bernoulli based development to extend over much larger geometrically nonlinear deformations since the curvature of the beam is not approximated.

The behavior of any beam will exhibit some material nonlinearity. A representative nonlinear term is included in the governing differential equation to illustrate how such constitutive nonlinearities are accounted for. The form of the nonlinear term adopted is consistent with the model proposed by Hinnant and Hodges<sup>4</sup>. The bending moment that corresponds to the potential energy term in Eq. (1) is

$$M = EI \frac{d\Psi}{ds} + C \left( \frac{d\Psi}{ds} \right)^3 \quad (16)$$

Using this definition of the moment  $M$  and Eq. (9) and Eq. (10), the static equilibrium equation becomes

$$EI \frac{d^3\Psi}{ds^3} + 6C \frac{d\Psi}{ds} \left( \frac{d^2\Psi}{ds^2} \right)^2 + 3C \left( \frac{d\Psi}{ds} \right)^2 \frac{d^3\Psi}{ds^3} = 0 \quad (17)$$

This cubic nonlinear effect corresponds to a 'hard' ( $C > 0$ ) or 'soft' ( $C < 0$ ) nonlinear stiffening with large deformations.

### 3.1.1 Model Validation

During the 1970's, Dowell, Traybar and Hodges<sup>10</sup> performed a series of experiments at Princeton University on the large deformation of a cantilevered beam with a mass attached to the tip. They were primarily interested in helicopter rotor blade stability, and carried out several experiments on a cantilever beam by rotating the beam root at various angles with respect to the beam principal axis and varying the tip weight. They compared their results to the Hodges and Dowell<sup>11</sup> nonlinear theory of rotor blade dynamics, and presented some results for pitch angles of 90 degrees which corresponds to planar deflection. The arc length approach can be checked against the transverse deflection results. Figure 5 shows tip deflections recovered using the present arc length approach along with those predicted by the Hodges and Dowell theory; and the deflections obtained experimentally.



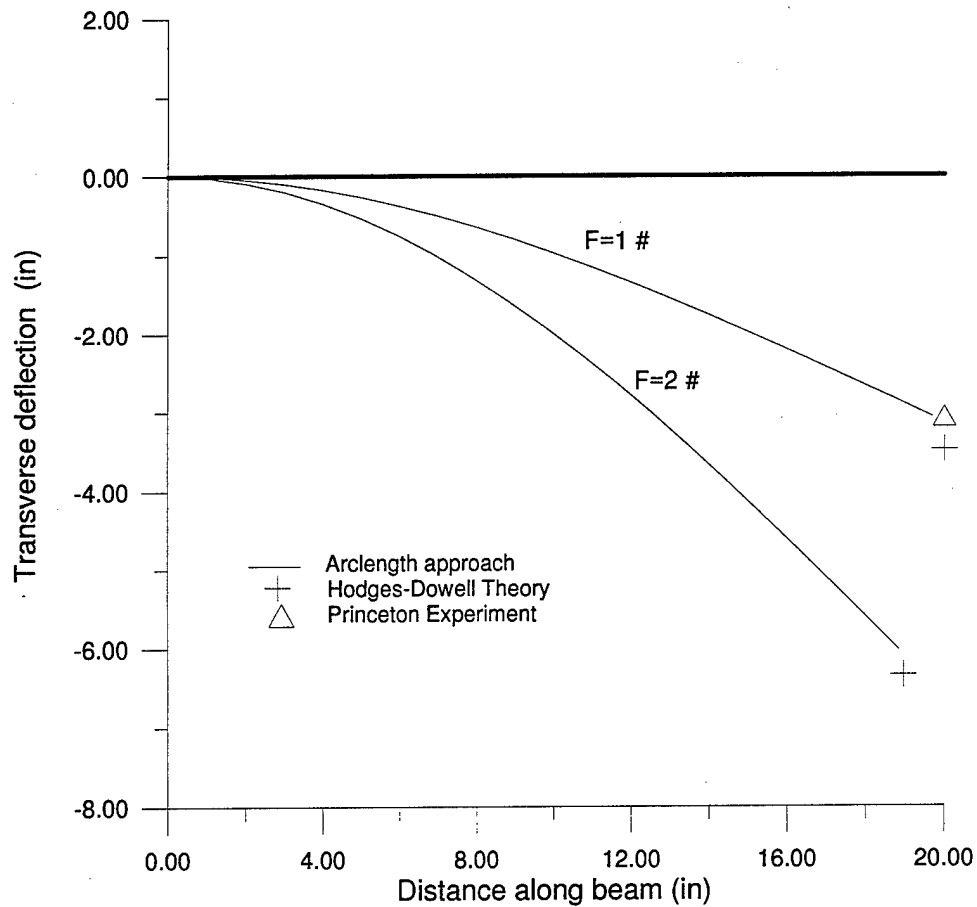


**Figure 5. Comparison of cantilever beam deflections from tip weights**

Unfortunately Dowell, Traybar and Hodges did not report results of beams at a 90 degree pitch angle for larger tip loads, so we cannot compare against their data for larger deflections.

However, published “exact” results are available for large deformation of cantilever beams for the special case of a pure moment applied to the free end. Figure 6 shows the displacement profile of the beam subjected to different moments from the arc length approach and from the exact solution<sup>9</sup>. These solutions allow the beam to be deformed to a complete circle.

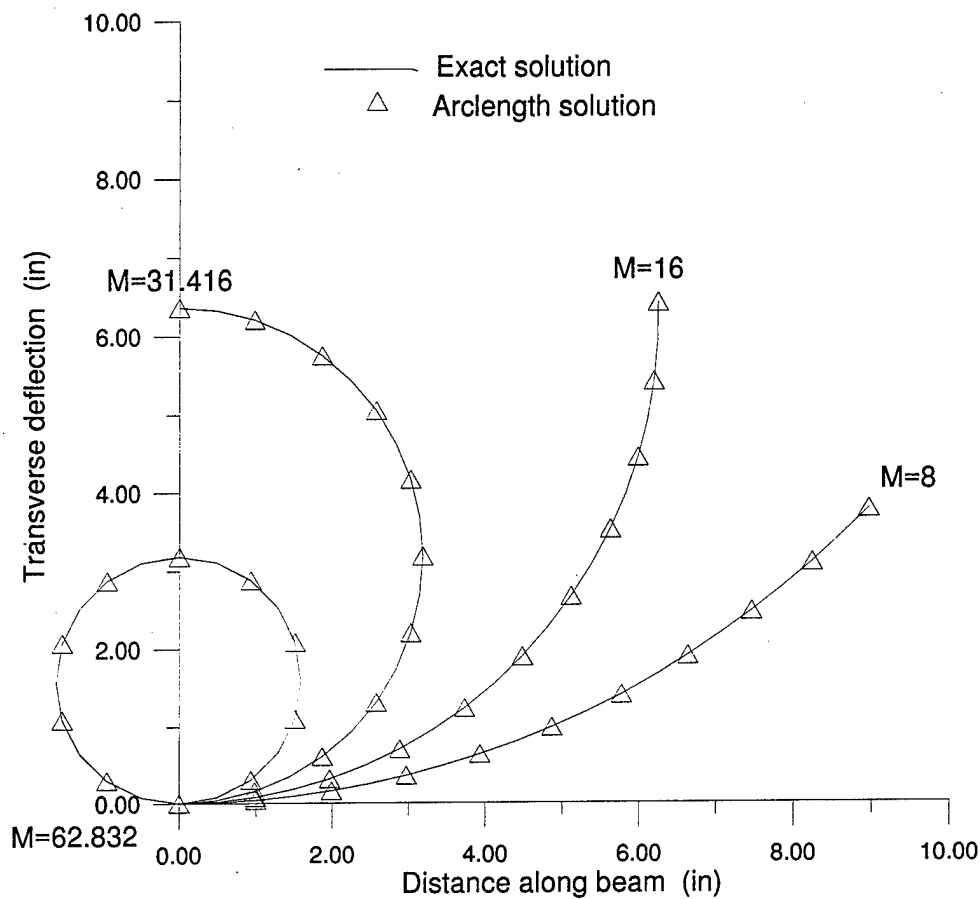


**Figure 6. Deflection of cantilever beam due to tip moment**

The arc length approach for small and large deformations due to end moments is in very good agreement both with available independent experiments and with the pure moment exact solutions from reference 9.

### 3.1.2 Application to Two Beam Model

The arc length approach is applied to a two beam system similar to the PACE structure in Figure 1. The geometry of this two beam system is illustrated in Figure 7. The PACE structure is simplified in that the shoulder hub, elbow connection and tip masses are treated as point masses. In this discussion, the shoulder hub is locked and the elbow angle is constrained to be zero (in the 'elbow locked' configuration). The arc length of the first

beam is measured from the shoulder hub and the first beam's tangent angle  $\Psi_1(s)$  is measured relative to a horizontal. For the second beam, the arc length is measured from the elbow connection of the two beams and the tangent angle  $\Psi_2(s)$  is measured relative to a vector tangent to the tip of beam 1 (vector has angle  $\Psi_1(L_1)$  relative to the horizontal). The choice of these coordinates simplifies the equation development of beam 2 and also permits automatic matching of the displacements and slopes at the connections of the two beams (for a "locked" elbow with zero elbow angle). This choice of coordinates allows the Euler Bernoulli beam theory to apply over large deformations. Notice that the angle  $\Psi_2(s)$  is measured relative to the tip of the first beams' tangent vector, whose elevation angle is  $\Psi_1(L_1)$  and is not measured relative to the horizontal.

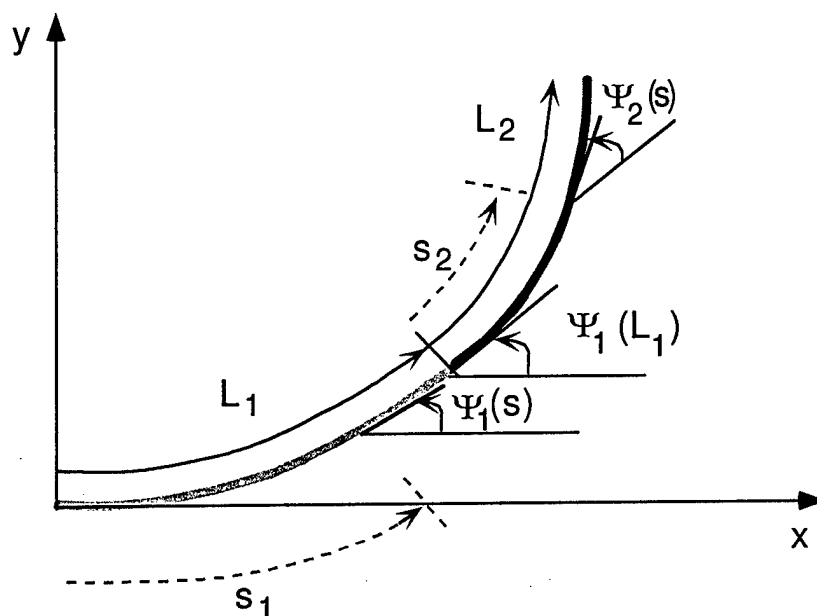


Figure 7. Two beam configuration

The static equilibrium equations are derived for each beam and differential equations for the coordinates  $x$  and  $y$  are included since they are needed in the enforcement of a boundary condition:

Beam 1

$$EI_1 \frac{d^3\Psi_1(s_1)}{ds_1^3} + 6C_1 \frac{d\Psi_1(s_1)}{ds_1} \left( \frac{d^2\Psi_1(s_1)}{ds_1^2} \right)^2 + 3C_1 \left( \frac{d\Psi_1(s_1)}{ds_1} \right)^2 \frac{d^3\Psi_1(s_1)}{ds_1^3} = 0 \quad (18a)$$

$$\frac{dy_1(s_1)}{ds_1} = \sin(\Psi_1(s_1)) \quad (18b)$$

$$\frac{dx_1(s_1)}{ds_1} = \cos(\Psi_1(s_1)) \quad (18c)$$

Beam 2

$$EI_2 \frac{d^3\Psi_2(s_2)}{ds_2^3} + 6C_2 \frac{d\Psi_2(s_2)}{ds_2} \left( \frac{d^2\Psi_2(s_2)}{ds_2^2} \right)^2 + 3C_2 \left( \frac{d\Psi_2(s_2)}{ds_2} \right)^2 \frac{d^3\Psi_2(s_2)}{ds_2^3} = 0 \quad (19a)$$

$$\frac{dy_2(s_2)}{ds_2} = \sin(\Psi_2(s_2)) \quad (19b)$$

$$\frac{dx_2(s_2)}{ds_2} = \cos(\Psi_2(s_2)) \quad (19c)$$

There are a total of ten boundary conditions that the solution of the above tenth order system of differential equations must satisfy. Six boundary conditions apply at the origin of each beam ( $s = 0$ ) where the angle  $\Psi(s)$  and the coordinates  $x(0)$ ,  $y(0)$  must equal zero. Two boundary conditions apply at the elbow connection of the beams where the bending moments must be equal Eq. (20) and the shear forces must be equal Eq. (21).

$$EI_1 \frac{d\Psi_1(L_1)}{ds_1} + C_1 \left( \frac{d\Psi_1(L_1)}{ds_1} \right)^3 = EI_2 \frac{d\Psi_2(0)}{ds_2} + C_2 \left( \frac{d\Psi_2(0)}{ds_2} \right)^3 \quad (20)$$

$$EI_1 \frac{d^2\Psi_1(L_1)}{ds_1^2} + 3C_1 \left( \frac{d\Psi_1(L_1)}{ds_1} \right)^2 \frac{d^2\Psi_1(L_1)}{ds_1^2} = EI_2 \frac{d^2\Psi_2(0)}{ds_2^2} + 3C_2 \left( \frac{d\Psi_2(0)}{ds_2} \right)^2 \frac{d^2\Psi_2(0)}{ds_2^2} \quad (21)$$

Two final boundary conditions must be enforced at the tip of the beam system depending on how the boundary forces are applied. The wire constraint experiment provides the final two boundary conditions needed to solve for the beam deformation shape.

### 3.1.3 Wire Constraint Experiment

A nonlinear static deformation experiment has been conceived to simplify testing of the two beam system and allow recovery of beam properties which contribute to the potential energy of the system. The idea of the experiment is to attach a wire to the tip of the beam system and measure the force required to deform the beam. A series of experiments with different measured tensions in the wire would yield a family of measured deformation shapes from which beam parameters such as the stiffness coefficients could be recovered. In most cases, only the tip and elbow deflections need to be measured for estimating the static parameters. The use of a wire with negligible bending stiffness has several advantages. From the beam standpoint, the wire provides a point force but no moment which acts on the tip of the beam. Along the wire, this one dimensional force can be measured anywhere using a load cell. The unit that holds the load cell and the end of

the wire would be attached to the tip of the beam and to the horizontal table using suction cups or electromagnets. This would also allow the beam to be released quickly without interfering with the free response of the beam. Once release occurs, the wire could be removed quickly allowing a free vibration of the two beam system and the recovery of some dynamic properties. Thus, the release mechanism serves two functions: (i) measurement of static deformation forces and (ii) a release mechanism for free dynamic response experiments. A prototype mechanism which measures the static tip force and permits easy release of the wire has been designed and tested by I. Romero<sup>12</sup>.

#### *Radial Wire Constraint*

One proposed experiment uses the wire to connect the tip of the beam to the shoulder hub. The wire would attach to a slip collar around the shoulder hub and only the magnitude of the force would be measured. A series of experiments with different wire lengths and corresponding required forces would be used to recover the parameters. For this static experiment, the two beam system must satisfy the geometric constraint due to the fixed length of the wire. This fixed wire length has an associated radial constraint force (wire tension) required for the beam deformation. Figure 8 illustrates the geometry of the wire length constraint for the special case that the opposite end of the wire with the measurement load cell is attached to the shoulder joint. This "bow" setup is but one of an infinite number of choices.

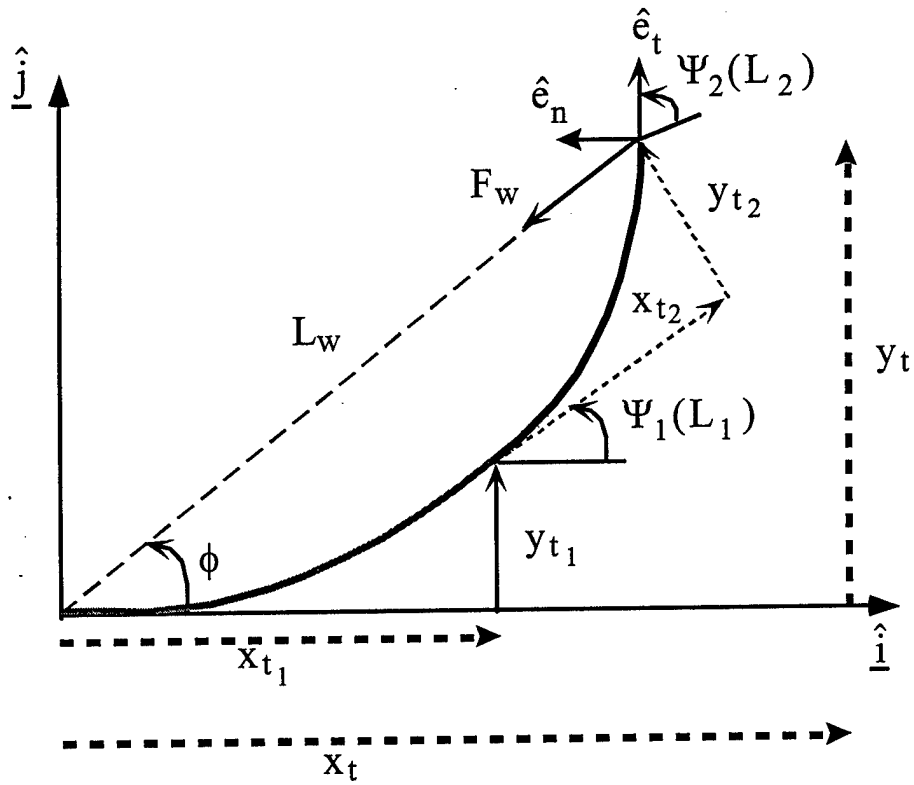


Figure 8. Radial wire constraint

The following equations define the geometric constraint

$$x_t^2 + y_t^2 - L_w^2 = 0 \quad (22a)$$

where

$$x_t = x_{t1} + x_{t2} \cos(\Psi_1(L_1)) - y_{t2} \sin(\Psi_1(L_1)) \quad (22b)$$

and

$$y_t = y_{t1} + x_{t2} \sin(\Psi_1(L_1)) + y_{t2} \cos(\Psi_1(L_1)) \quad (22c)$$

The radial wire provides the final two boundary conditions; the geometric constraint Eq. (22a) - Eq. (22c) must be satisfied and the bending moment at the tip of the second beam must be zero.

generated by simply deforming the beam with different wire tensions. Applying a directed force would be more difficult to implement experimentally since the shoulder hub must be constrained and the alignment of the force would have to be done carefully. For this experiment, the final two boundary conditions would require the shear force in the wire to match the shear force in the beam

$$F_{sh} = F_w \sin(\Psi_2(L_2) + \Psi_1(L_1)) = EI_2 \frac{d^2\Psi_2(L_2)}{ds_2^2} + 3C_2 \left( \frac{d\Psi_2(L_2)}{ds_2} \right)^2 \frac{d^2\Psi_2(L_2)}{ds_2^2} \quad (27)$$

and the bending moment at the tip is zero, Eq. (23).

#### 3.1.4 Boundary Value Problem

Satisfying the set of equilibrium equations Eq. (18a) - Eq. (19c) is a nonlinear two-point boundary value problem where some initial conditions are unknown. An algorithm for the solution of this boundary value problem is established as follows. The first beam differential equations Eq. (18a) - Eq. (18c) are integrated using the Runge Kutta technique along the length of the beam, then the second beam equations Eq. (19a) - Eq. (19c) are integrated. A second order Newton's method is used to iteratively adjust approximate initial conditions to match the boundary conditions. The initial conditions are summarized below

#### Initial Conditions - Beam 1

$$\Psi_1(0) = 0 \quad (28a)$$

$$\frac{d\Psi_1(0)}{ds_1} = \textit{unknown} \quad (28b)$$



$$\frac{d\Psi_1^2(0)}{ds_1^2} = \text{unknown} \quad (28c)$$

$$y_1(0) = 0 \quad (28d)$$

$$x_1(0) = 0 \quad (28e)$$

### Initial Conditions - Beam 2

$$\Psi_2(0) = 0 \quad (29a)$$

$$\frac{d\Psi_2(0)}{ds_2} = \text{unknown} \quad (29b)$$

$$\frac{d\Psi_2^2(0)}{ds_2^2} = \text{unknown} \quad (29c)$$

$$y_2(0) = 0 \quad (29d)$$

$$x_2(0) = 0 \quad (29e)$$

In order to determine the unknown initial conditions ( $\Psi_1'(0)$ ,  $\Psi_1''(0)$ ,  $\Psi_2'(0)$ ,  $\Psi_2''(0)$ ) using Newton's method, the derivatives of the boundary conditions [Eq. (20), Eq. (21), Eq. (22), Eq. (23)] with respect to these parameters are taken. The four boundary equations are rewritten so that all the terms are collected on one side and then the equations are represented by the variables  $\Gamma_1$ ,  $\Gamma_2$ ,  $\Gamma_3$ ,  $\Gamma_4$ . The derivatives of these boundary conditions are taken with respect to the initial conditions and the results are rearranged and written in matrix form to solve for approximate initial boundary condition corrections as

$$\begin{Bmatrix} \Delta\Psi_1'(0) \\ \Delta\Psi_1''(0) \\ \Delta\Psi_2'(0) \\ \Delta\Psi_2''(0) \end{Bmatrix} = \begin{bmatrix} \frac{\partial\Gamma_1}{\partial\Psi_1'(0)} & \frac{\partial\Gamma_1}{\partial\Psi_1''(0)} & \frac{\partial\Gamma_1}{\partial\Psi_2'(0)} & \frac{\partial\Gamma_1}{\partial\Psi_2''(0)} \\ \frac{\partial\Gamma_2}{\partial\Psi_1'(0)} & \frac{\partial\Gamma_2}{\partial\Psi_1''(0)} & \frac{\partial\Gamma_2}{\partial\Psi_2'(0)} & \frac{\partial\Gamma_2}{\partial\Psi_2''(0)} \\ \frac{\partial\Gamma_3}{\partial\Psi_1'(0)} & \frac{\partial\Gamma_3}{\partial\Psi_1''(0)} & \frac{\partial\Gamma_3}{\partial\Psi_2'(0)} & \frac{\partial\Gamma_3}{\partial\Psi_2''(0)} \\ \frac{\partial\Gamma_4}{\partial\Psi_1'(0)} & \frac{\partial\Gamma_4}{\partial\Psi_1''(0)} & \frac{\partial\Gamma_4}{\partial\Psi_2'(0)} & \frac{\partial\Gamma_4}{\partial\Psi_2''(0)} \end{bmatrix}^{-1} \begin{Bmatrix} 0-\Gamma_1 \\ 0-\Gamma_2 \\ 0-\Gamma_3 \\ 0-\Gamma_4 \end{Bmatrix}_n \quad (30)$$

The new values of the initial conditions are determined and the numerical solution of the equilibrium equations is repeated until the unknown initial conditions have converged. In the derivatives of these boundary conditions, the sensitivity of the solution variables, ( $\Psi_1$ ,  $\Psi_2$ ) with respect to the unknown initial conditions are contained. For example, one of the terms needed in Eq (30) is

$$\frac{\partial\Gamma_4}{\partial\Psi_2'(0)} = EI_2 \frac{\partial\Psi_2'(L_2)}{\partial\Psi_2'(0)} + 3C_2\Psi_2'(L_2) \frac{\partial\Psi_2'(L_2)}{\partial\Psi_2'(0)} \quad (31)$$

The sensitivities of the solution variables with respect to the initial conditions (like  $\partial\Psi_2'(L_2)/\partial\Psi_2'(0)$ ) must be numerically integrated. This is done using a state transition matrix approach. One can write Eq. (18a) - Eq. (18c) in first order form using the vector  $z(s)$  [where  $z(s)^T = \{\Psi_1(s), \Psi_1'(s), \Psi_1''(s), y_1(s), x_1(s)\}$ ] and by defining the derivative equations as the vector  $f(z(s))$  so that

$$\frac{dz(s)}{ds} = f(z(s)) \quad (32)$$

By manipulating this equation, the following differential equation is developed which governs the spatial evolution of the "transition matrix" (partial derivatives of  $z(s)$  with respect to  $z(0)$ ):

$$\frac{d}{ds} \left[ \frac{\partial z(s)}{\partial z(0)} \right] = \left[ \frac{\partial f(z(s))}{\partial z(s)} \right] \left[ \frac{\partial z(s)}{\partial z(0)} \right] \quad (33)$$

The initial ( $s=0$ ) condition for this matrix of equations is the identity matrix and these equations can be numerically integrated simultaneous with Eq. (18a) - Eq. (18c) over the arc length to yield the sensitivities to  $\Psi_1'(0)$  and  $\Psi_1''(0)$ . The same approach can be taken for the second beam equations [Eq. (19a) - Eq. (19c)] using the analogous state vector  $w(s)$  and defining the derivative equations as the vector  $g(w(s))$

$$\frac{dw(s)}{ds} = g(w(s)) \quad (34)$$

Manipulation of this equation yields

$$\frac{d}{ds} \left[ \frac{\partial w(s)}{\partial w(0)} \right] = \left[ \frac{\partial g(w(s))}{\partial w(s)} \right] \left[ \frac{\partial w(s)}{\partial w(0)} \right] \quad (35)$$

The initial condition of this set of equations is the identity matrix and the equations are numerically integrated along the beam length. Values for the terms  $\partial z(L_1) / \partial z(0)$  and  $\partial w(L_2) / \partial w(0)$  are used in the derivatives of the boundary equations (in terms like Eq. (31)), and the changes to the unknown initial conditions are calculated.

### 3.1.5 Simulations

#### *Radial Wire Constraint*

The deformation of the two beam system with beam properties from the PACE model is studied for various lengths of the wire constraint and values of the nonlinear coefficients  $C_1$  and  $C_2$ . The iterative solution process outlined in the previous section converges very rapidly and without any numerical singularities for wire lengths ranging from 98% to 42% of the total beams length. Obviously the traditional Euler Bernoulli beam theory would not apply to some of these large deformations but it does show the robustness of the solution technique. Figure 9 shows the deformation of four cases with different wire constraints.

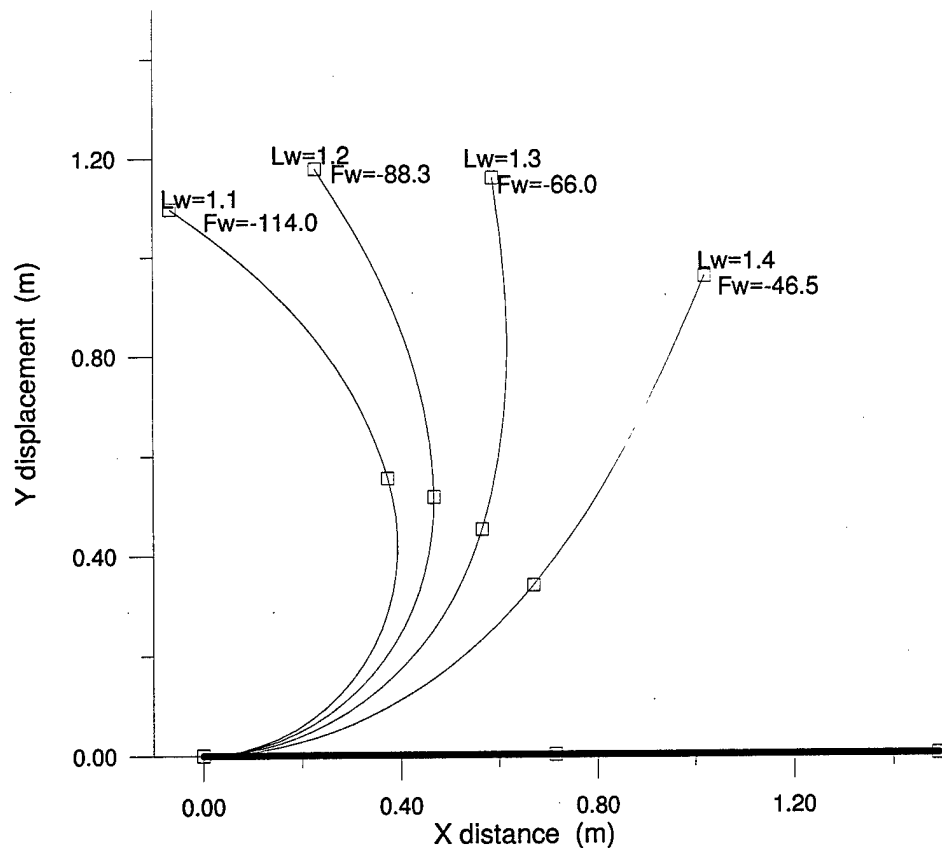


**Figure 9. Effect of wire constraint length**

The force in the wire increases dramatically with successively smaller wire lengths. Figure 10 shows the change in deformation shape for a given length of wire with increases in the nonlinear coefficients. These results are for positive C's which correspond to beam stiffening.

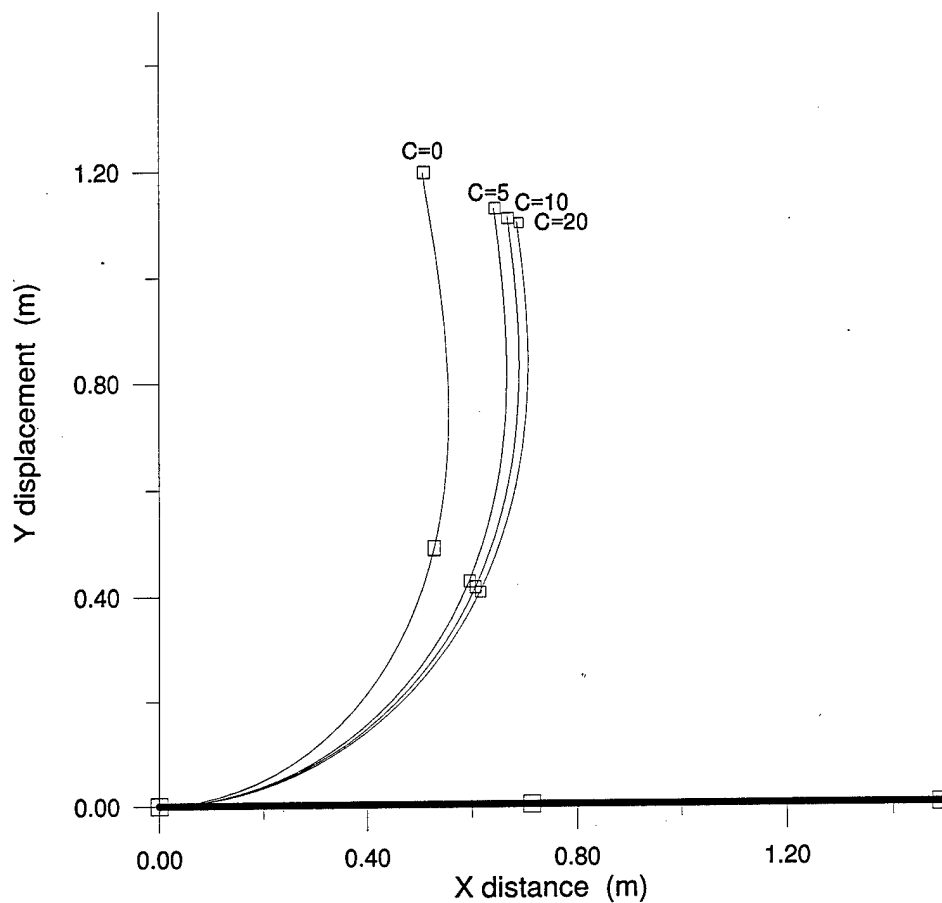


Figure 10. Effect of material nonlinearity

The first increase in the coefficients of the nonlinear terms results in the largest change in the deformation shape of the system. Larger increases in the coefficients slightly change the deformation shape but the effects of the increases are mainly felt in the wire force

calculations which involves higher derivatives of the angle  $\Psi_2(s)$ . Table 2 shows the trend of larger increases in the wire force and smaller effects on the systems tip location.

Coefficient $C_1, C_2$	Force in wire	Tip x location	Tip y location
0 (No nonlinearity)	33.3	.506	1.197
1, 1	37.6	.573	1.167
5, 5	53.3	.643	1.130
10, 10	72.1	.668	1.115
20, 20	109.3	.686	1.104
30, 30	145.3	.693	1.100

#### *Directed Force*

In this experiment, the force on the tip of the system is directed perpendicular to the undeformed axis (the  $y$  direction shown in Figure 8). This force will be referred to as a transverse force. The deformation of the two beam system with beam properties from the PACE model is studied for different values of wire forces. To be consistent with the initial deformation shape used in the dynamic analysis, the nonlinear coefficients are set to zero. This removes the constitutive nonlinearity from the model but leaves the geometric nonlinearity due to the trigonometric functions involved in the solution. The deformation shapes for four wire tensions are shown in Figure 11.

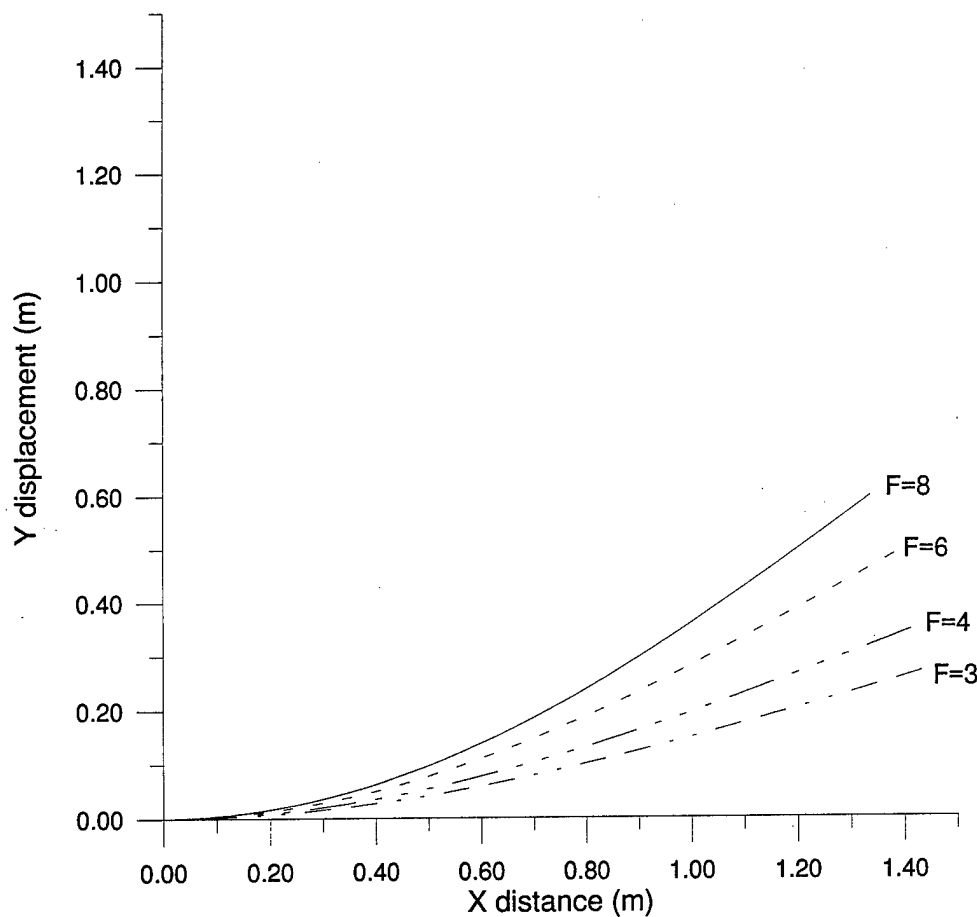


**Figure 11. Deformation shapes for series of transverse forces**

The solution of the boundary value problem quickly recovers the unknown initial conditions and the deformation shapes for the different force boundary conditions.

### **3.2 Static Parameter Estimation**

If the beam properties are uncertain, the parameters affecting the static deformation shape can be recovered using measurements from two or more experiments. The effective stiffness and nonlinear coefficients for each beam are some of the parameters that may not be well known.

### 3.2.1 Least Squares Estimation

A least squares analysis is used to recover the best fit parameters for the arc length models represented by Eqs. (18a) - (18c) and Eqs. (19a) - (19c). This is a nonlinear estimation problem and the least square differential correction technique<sup>13</sup> is used to successively approximate the parameters. The error between the measured values and those predicted by the model using the updated parameters are minimized

$$e = \tilde{Y}_{meas} - \hat{Y}_{model}(p_{n+1}) \quad (36)$$

The parameter vector  $p$  represents the variables to be recovered. Measurements at different time intervals are represented by the vector  $\tilde{Y}_{meas}$ . The model values cannot be written as explicit functions of the parameters since determining the model values involves the numerical solution of the differential arc length equations. The values from the nonlinear model for a given set of parameters can be calculated and a new set of parameters can be approximated using a first order Taylor series expansion

$$\hat{Y}_{model}(p_{n+1}) = \hat{Y}_{model}(p_n) + \Omega(p_{n+1} - p_n) \quad , \quad \text{where} \quad \Omega = \left. \frac{\partial \hat{Y}}{\partial p} \right|_n \quad (37)$$

This is substituted into the error expression giving

$$e = \tilde{Y}_{meas} - \hat{Y}_{model}(p_n) - \Omega(p_{n+1} - p_n) \quad (38)$$

The sum square of the error is minimized and the new approximation for the parameter  $p$  is solved

$$p_{n+1} = p_n + (\Omega^T \Omega)^{-1} \Omega^T (\tilde{Y}_{meas} - \hat{Y}_{model}(p_n)) \quad (39)$$



Each column of the sensitivity matrix  $\Omega$  represents the derivative of the corresponding measurements with respect to one parameter. The rows of the matrix represent the values of the gradients at each measurement time.

This estimation procedure is complicated by the fact that the governing equations are nonlinear differential equations and further complicated by the fact any trial solution requires solution of a two point boundary value problem. In order to establish the needed sensitivities, we introduce a novel method for differentiating an implicit function<sup>7</sup>.

#### *Implicit Function Theorem*

The differential equations must first be solved for the initial values of  $\Psi$  for a given set of parameters  $p$  and then repeated for updated values of the parameters until the method converges. A more subtle question arises, what is the sensitivity of the solution ( $\Psi_1'(0)$ ,  $\Psi_1''(0)$ ,  $\Psi_2'(0)$ ,  $\Psi_2''(0)$ ) of the boundary value problem with respect to a parameter  $p$ ? Therefore the boundary value problem must be solved for each iteration of the parameters. In order to calculate the changes in the parameters using the least squares method, the derivatives of the measurements (such as  $x_t$ ) with respect to the parameters must be calculated. To fill this derivative matrix, the equations defining the measurements (Eq. (22b) for  $x_t$ ) must be differentiated with respect to the parameters  $p$ . These derivative equations contain terms such as  $\partial x_1(L_1)/\partial p$ ,  $\partial \Psi_1(L_1)/\partial p$  which must be determined and integrated along the arc length. Again a state transition approach is taken but in this case we are concerned with the model parameters  $p$  instead of the initial conditions  $z(0)$ . The governing differential equations for the first beam Eq. (18a) - Eq. (18c) can be written

$$\frac{d}{ds}(z(s)) = f(z, p) \tag{40}$$

and by manipulation, we can derive a differential equation for the needed partial derivatives:

$$\frac{d}{ds} \left[ \frac{\partial z(s)}{\partial p} \right] = \left[ \frac{\partial f}{\partial z} \right] \left[ \frac{\partial z}{\partial p} \right] + \frac{\partial f}{\partial p} \quad (41)$$

Similarly the governing equations for the second beam Eq. (19a) - Eq. (19c) can be written

$$\frac{d}{ds} (w(s)) = g(w, p) \quad (42)$$

and

$$\frac{d}{ds} \left[ \frac{\partial w(s)}{\partial p} \right] = \left[ \frac{\partial g}{\partial w} \right] \left[ \frac{\partial w}{\partial p} \right] + \frac{\partial g}{\partial p} \quad (43)$$

To integrate these matrix differential equations to compute the derivatives  $(\partial x_1(L_1)/\partial p$ ,  $\partial \Psi_1(L_1)/\partial p$ , etc), the initial conditions  $\partial z(0)/\partial p$  and  $\partial w(0)/\partial p$  must first be determined. The main difficulty lies in determining  $\partial \Psi_1'(0)/\partial p$ ,  $\partial \Psi_1''(0)/\partial p$ ,  $\partial \Psi_2'(0)/\partial p$  and  $\partial \Psi_2''(0)/\partial p$  which are the initial conditions of these sensitivity matrices in Eq. (41) ( $\partial z(0)/\partial p$ ) and Eq. (43) ( $\partial w(0)/\partial p$ ). The initial values  $\Psi_1'(0)$ ,  $\Psi_1''(0)$ ,  $\Psi_2'(0)$  and  $\Psi_2''(0)$  must first be determined to match the boundary conditions as specified in section 3.1.4 (using the differential equations Eq. (18a) - Eq(19c)). Then the initial conditions for the state transition matrices Eq. (41) and Eq.(43) can be determined. To find the initial conditions for  $\partial \Psi_1'(0)/\partial p$ ,  $\partial \Psi_1''(0)/\partial p$ ,  $\partial \Psi_2'(0)/\partial p$  and  $\partial \Psi_2''(0)/\partial p$  we will apply the implicit function theorem to the boundary condition equations. The boundary condition equations [Eq. (20), Eq. (21), Eq. (22) and Eq. (23)] can be written as functions of the initial conditions and the parameters  $p$

$$\Gamma_1(\Psi_1'(0), \Psi_1''(0), \Psi_2'(0), \Psi_2''(0), EI_1, K_1, EI_2, K_2) = 0 \quad (44)$$

$$\Gamma_2(\Psi_1'(0), \Psi_1''(0), \Psi_2'(0), \Psi_2''(0), EI_1, K_1, EI_2, K_2) = 0 \quad (45)$$

$$\Gamma_3(\Psi_1'(0), \Psi_1''(0), \Psi_2'(0), \Psi_2''(0), EI_1, K_1, EI_2, K_2) = 0 \quad (46)$$

$$\Gamma_4(\Psi_1'(0), \Psi_1''(0), \Psi_2'(0), \Psi_2''(0), EI_1, K_1, EI_2, K_2) = 0 \quad (47)$$

We can treat the initial conditions  $\Psi_1'(0)$ ,  $\Psi_1''(0)$ ,  $\Psi_2'(0)$ ,  $\Psi_2''(0)$  as the dependent variables and the parameters  $p$  as the independent variables. The implicit function theorem is used to determine derivatives of these functions. This is an unusual application of the theorem since the variables in the boundary condition equations are obtained from a solution of a two point boundary value differential equation. Using the derivative of an implicit function<sup>7</sup>, the partial derivatives of the functions with respect to each parameter  $p_i$  is

$$\frac{\partial \Gamma_1}{\partial p_i} + \frac{\partial \Gamma_1}{\partial \Psi_1'(0)} \frac{\partial \Psi_1'(0)}{\partial p_i} + \frac{\partial \Gamma_1}{\partial \Psi_1''(0)} \frac{\partial \Psi_1''(0)}{\partial p_i} + \frac{\partial \Gamma_1}{\partial \Psi_2'(0)} \frac{\partial \Psi_2'(0)}{\partial p_i} + \frac{\partial \Gamma_1}{\partial \Psi_2''(0)} \frac{\partial \Psi_2''(0)}{\partial p_i} = 0 \quad (48)$$

$$\frac{\partial \Gamma_2}{\partial p_i} + \frac{\partial \Gamma_2}{\partial \Psi_1'(0)} \frac{\partial \Psi_1'(0)}{\partial p_i} + \frac{\partial \Gamma_2}{\partial \Psi_1''(0)} \frac{\partial \Psi_1''(0)}{\partial p_i} + \frac{\partial \Gamma_2}{\partial \Psi_2'(0)} \frac{\partial \Psi_2'(0)}{\partial p_i} + \frac{\partial \Gamma_2}{\partial \Psi_2''(0)} \frac{\partial \Psi_2''(0)}{\partial p_i} = 0 \quad (49)$$

$$\frac{\partial \Gamma_3}{\partial p_i} + \frac{\partial \Gamma_3}{\partial \Psi_1'(0)} \frac{\partial \Psi_1'(0)}{\partial p_i} + \frac{\partial \Gamma_3}{\partial \Psi_1''(0)} \frac{\partial \Psi_1''(0)}{\partial p_i} + \frac{\partial \Gamma_3}{\partial \Psi_2'(0)} \frac{\partial \Psi_2'(0)}{\partial p_i} + \frac{\partial \Gamma_3}{\partial \Psi_2''(0)} \frac{\partial \Psi_2''(0)}{\partial p_i} = 0 \quad (50)$$

$$\frac{\partial \Gamma_4}{\partial p_i} + \frac{\partial \Gamma_4}{\partial \Psi_1'(0)} \frac{\partial \Psi_1'(0)}{\partial p_i} + \frac{\partial \Gamma_4}{\partial \Psi_1''(0)} \frac{\partial \Psi_1''(0)}{\partial p_i} + \frac{\partial \Gamma_4}{\partial \Psi_2'(0)} \frac{\partial \Psi_2'(0)}{\partial p_i} + \frac{\partial \Gamma_4}{\partial \Psi_2''(0)} \frac{\partial \Psi_2''(0)}{\partial p_i} = 0 \quad (51)$$

The implicit and explicit derivatives are computed and inserted into this set of equations which are used to solve for  $\partial\Psi_1'(0)/\partial p_i$ ,  $\partial\Psi_1''(0)/\partial p_i$ ,  $\partial\Psi_2'(0)/\partial p_i$ ,  $\partial\Psi_2''(0)/\partial p_i$ . These are needed along with other initial conditions to integrate the sensitivity matrices Eq. (41) and Eq. (43) over the arc lengths  $s$ . After this integration, the recovered derivatives such as  $\partial x_1(L_1)/\partial EI_1$  are used in computing the measurement equation derivatives.

The computation of the derivatives in the sensitivity matrix can now be carried out knowing the partials of the first and second beam variables from the process outlined above. With this derivative matrix we can compute the needed corrections to the parameters  $p$  using Eq. (39). This whole process must be repeated until the parameters  $p$  are recovered which yield the measurement values for each test. As will be evident in the numerical studies, the domain of practical convergence is usually large, tolerating up to 40% errors in the starting estimates.

#### *Radial Wire Constraint*

The radial wire experiment permits us to estimate the effective stiffness and nonlinear coefficients ( $p = EI_1, C_1, EI_2, C_2$ ) using as few as two experiments with different wire lengths. There are two independent measurements taken during each test. In this development, the force in the constraining wire and the global  $x$  location of the tip of the second beam are assumed to be measured. Any  $x$  or  $y$  measurement would also work, but  $x_t$  is chosen for experimental simplicity. For this determined system, the sensitivity matrix for the two experiment case is

$$\Omega = \begin{bmatrix} \frac{\partial x_t^a}{\partial EI_1} & \frac{\partial x_t^a}{\partial \mathcal{X}_1} & \frac{\partial x_t^a}{\partial EI_2} & \frac{\partial x_t^a}{\partial \mathcal{X}_2} \\ \frac{\partial F_w^a}{\partial EI_1} & \frac{\partial F_w^a}{\partial \mathcal{X}_1} & \frac{\partial F_w^a}{\partial EI_2} & \frac{\partial F_w^a}{\partial \mathcal{X}_2} \\ \frac{\partial x_t^b}{\partial EI_1} & \frac{\partial x_t^b}{\partial \mathcal{X}_1} & \frac{\partial x_t^b}{\partial EI_2} & \frac{\partial x_t^b}{\partial \mathcal{X}_2} \\ \frac{\partial F_w^b}{\partial EI_1} & \frac{\partial F_w^b}{\partial \mathcal{X}_1} & \frac{\partial F_w^b}{\partial EI_2} & \frac{\partial F_w^b}{\partial \mathcal{X}_2} \end{bmatrix} \quad (52)$$

( where: superscript <sup>a</sup> denotes data from the 1st test, and <sup>b</sup> denotes data from the 2nd test)

The derivatives of the equations for  $x_t$  [Eq. (22b)] and the  $F_w$  [Eq.(26)] equations are taken with respect to the parameters. The partials of the first and second beam variables contained in those equations are determined from the process outlined in the previous section. These derivatives are used to populate the sensitivity matrix and the changes to the beam parameters  $p$  are determined using the least squares method.

#### *Measurement Errors*

Often the measurements in  $\hat{Y}_{meas}$  are made with unequal precision and approximate weighting should be included in the parameter updating. The reciprocal of the error variance is the conventional "optimal" choice for the weight and is qualitatively correct since a measurement with a small error would have a large weight and one with a large error would have a very small weight. The error variance,  $\sigma^2$  is approximated in practice as the square of the standard deviation, representing the theoretical squared sums of the differences between a large number of measurements and the mean value. The least squares function of the residual error including a positive definite weight matrix  $W$  becomes

$$J = \frac{1}{2} \left[ \tilde{Y}_{meas} - \hat{Y}_{model}(p_{n+1}) \right]^T W \left[ \tilde{Y}_{meas} - \hat{Y}_{model}(p_{n+1}) \right] \quad (53)$$

$$\text{where } W = \begin{bmatrix} \frac{1}{\sigma_1^2} & 0 & \dots & 0 \\ 0 & \frac{1}{\sigma_2^2} & \dots & 0 \\ \vdots & \vdots & \ddots & \vdots \\ 0 & 0 & \dots & \frac{1}{\sigma_{\#meas}^2} \end{bmatrix}$$

Substituting in for  $\hat{Y}_{model}(p_{n+1})$  and minimizing the function  $J$ , the parameter update becomes

$$p_{n+1} = p_n + (\Omega^T W \Omega)^{-1} \Omega^T W (\tilde{Y}_{meas} - \hat{Y}_{model}(p_n)) \quad (54)$$

The measurement errors are mapped through the estimation algorithm into associated errors in the estimated parameters. This relationship is developed in reference 13. The covariance matrix of the parameters is related to the variance matrix of the measurements by the following

$$E_s = (\Omega^T W \Omega)^{-1} = \begin{bmatrix} \sigma_{p1}^2 & \tau_{12} \sigma_{p1} \sigma_{p2} & \dots & \tau_{1\#} \sigma_{p1} \sigma_{p\#} \\ \tau_{21} \sigma_{p2} \sigma_{p1} & \sigma_{p2}^2 & \dots & \tau_{2\#} \sigma_{p2} \sigma_{p\#} \\ \vdots & \vdots & \ddots & \vdots \\ \tau_{\#1} \sigma_{p\#} \sigma_{p1} & \tau_{\#2} \sigma_{p\#} \sigma_{p2} & \dots & \sigma_{p\#}^2 \end{bmatrix} \quad (55)$$

The diagonal elements of the error covariance matrix gives an indication of how accurately the parameters are estimated. Each of the 'true' parameters should be typically contained within three times the standard deviation  $\sigma_p$  of the recovered parameter. The  $\tau_{ij}$ 's are measures of correlation of the estimation errors.

### *Directed Force*

The directed force experiment recovers the effective stiffness coefficients ( $p = EI_1, EI_2$ ) using a number of measurements. In this development, the global  $y$  location of the tip of the second beam is assumed to be measured. The  $y$  measurement is chosen since the stiffness coefficients clearly have a large affect on this variable. A number of measurements are used to over determine the parameters. The sensitivity matrix for this problem becomes

$$\Omega = \begin{bmatrix} \frac{\partial y_t^1}{\partial EI_1} & \frac{\partial y_t^1}{\partial EI_2} \\ \frac{\partial y_t^2}{\partial EI_1} & \frac{\partial y_t^2}{\partial EI_2} \\ \frac{\partial y_t^3}{\partial EI_1} & \frac{\partial y_t^3}{\partial EI_2} \\ \vdots & \vdots \\ \frac{\partial y_t^N}{\partial EI_1} & \frac{\partial y_t^N}{\partial EI_2} \end{bmatrix} \quad (56)$$

( where the superscript number refers to the measurement number from 1 to  $N$  )

The derivatives of the equation for  $y_t$  [Eq. (22c)] are taken with respect to both stiffness parameters. The partials of the first and second beam variables contained in those equations are determined from the implicit differentiation process outlined previously. These derivatives are used in the sensitivity matrix and changes to the beam parameters  $p$  are determined using the least squares method.

The parameter estimation method for the directed force experiment is enhanced to include measurement errors and their associated variance in the least squares determination of the parameters. A weight matrix is included in the parameter updating and reflects the uncertainties in the measurements. The parameters recovered have associated error variances which indicates how well the experiment determines the parameters.

### 3.2.2 Results - Static Deformation Parameters

The approach for estimation of parameters affecting the static deformation of the beam system is tested using a computer simulation of measured data for two types of experiments.

#### *Radial Wire Constraint*

We first consider the determined case, a radial wire experiment to determine the static potential energy parameters, assuming the system measurements are accurate. This proposed experiment uses a wire to connect the tip of the beam to the shoulder hub which provides a geometric constraint on the solution. To generate simulated measurements, the two beam forward solution using the arc length approach is computed for two different wire lengths and a given set of 'true' parameters. The deformation shapes of the two wire lengths,  $L_w=1.4$  and  $L_w=1.3$ , are shown in Figure 9. The resulting values of  $x_t$  and  $F_w$  are used as measurements in the inverse solution to see if the program can recover the 'true' values given poor starting estimates. An approximation of the true model is constructed by increasing the parameter errors from 8% to 11% and is used to start the parameter estimation process. Table 3 summarizes the input and recovered values of the parameters. The program converges rapidly to the values in the last column which are virtually identical to the 'true' values. The calculated values of  $x_t$  and  $F_w$  are matched exactly with the input measured values.

Parameters	True Values	Input Values	Converged Values
$EI_1$	11.413	10.400	11.415
$C_1$	5.000	4.550	5.000
$EI_2$	11.275	10.175	11.276
$C_2$	20.000	17.800	19.991



The parameter recovery method based on this series of static measurements converges rapidly to the known set of parameter values. The parameter  $C_2$  is less well observable, however, and the true measurement case suggest larger deformations and redundant measurements will be needed to accurately estimate  $C_2$ .

#### *Directed Force*

This experiment recovers the effective stiffness coefficients for each beam when the system is subjected to a transverse force boundary condition. Here we ignore the terms containing  $C_1$ ,  $C_2$  and estimate only  $EI_1$ ,  $EI_2$ . The static parameters are recovered when the system is statically deformed in a manner consistent with the initial conditions used in the dynamic analysis. The measurements of  $y_t$  are simulated by computing the forward solution using the arc length approach for four values of the transverse force  $F$  and a given set of 'true' parameters. This family of static deformation shapes is shown in Figure 11. Redundant measurements were used to allow the overdetermination of the parameters. Estimates of the stiffness coefficients are used to start the parameter recovery program and the results are shown in Table 4.

<b>Table 4. Parameter recovery for directed force</b>			
Parameters	True Values	Input Values	Converged Values
$EI_1$	11.413	10.750	11.413
$EI_2$	11.275	10.500	11.275

The values of the parameters are converged after five iterations and are identical to the 'true' values.

Physical measurements of  $y_t$  will have some uncertainties associated with the values and this can be reflected in the error variance of the measurements. To reflect this

in the simulated measurements, errors are introduced using a Gaussian random number generator and an associated standard deviation  $\sigma$ . For each measurement, an error is created from a random number belonging to a distribution having zero mean and the specified standard deviation  $\sigma$ . These simulated measurement errors are added to the 'true' values of the measurable quantities which are then used in the parameter recovery program. The weighted least squares function is used to minimize the errors and the parameters are determined using Eq. (54). The 'true' measurements of  $y_i$  have values ranging from 0.276332 to 0.597325. The standard deviations for the errors in these simulated measurements are input to the program and range from .0008 to .0011. The parameter recovery program is started with initial estimates of the stiffness coefficients and Table 5 shows the recovered parameters when measurement uncertainties are included.

<b>Table 5. Parameter recovery for directed force with measurement errors</b>		
	$EI_1$	$EI_2$
True values	11.413	11.275
Initial estimate	10.750	10.500
Recovered values	11.410	10.987

The stiffness coefficient recovered for the first beam is virtually identical to the uncorrupted 'true' value and has a small variance. However, the stiffness coefficient recovered for the second beam is not as well determined in the presence of measurement errors and differs by 3% to the 'true' value. The recovered parameters have associated error covariances as defined by Eq. (55). Small values indicate the parameters are well determined. The covariance matrix for these parameters are

$$E_s = \begin{bmatrix} .004497 & -.047864 \\ -.047864 & .549850 \end{bmatrix}$$

As expected, the stiffness coefficient for the second beam has a large standard deviation ( $\sigma \cong \sqrt{.55} \cong .7$ ) which indicates it is not as well determined as the first beam's value. We note the converged estimate differs from the true value of  $EI_2$  by  $\cong 0.28$  which is well within one sigma, so there is good consistency between the actual estimation error and the uncertainty estimate. The difference in the ability to estimate the first beam's stiffness coefficient better than the second beam's stiffness coefficient is due to the storage of potential energy in a cantilever beam system. When the system is subjected to a tip force, the portion of the system closest to the clamped boundary condition deforms the most (has the largest curvature and bending moment) and the parameters most affecting that response will most easily be recovered. The information on the estimated parameters and their associated covariance matrix can be "carried forward" and used in the recovery of parameters affecting the dynamic motion.

## CHAPTER IV

### NONLINEAR FREE VIBRATION ANALYSIS

#### 4.1 Model Development

A mathematical model for predicting the dynamic motion of the two beam system is developed for use in estimating the parameters affecting the free vibration response of the system. A nonlinear finite element model is developed due to difficulties encountered in the arc length approach.

##### 4.1.1 Arc Length Approach

The arc length approach can not be easily extended to the dynamic analysis due to the fact that certain integrals arise which complicate the structure of the kinetic energy and the equations which result. This can be seen by looking at the dynamic equation of motion

$$m(s)ds \frac{\partial^2 \underline{r}(s,t)}{\partial t^2} \cdot \hat{\underline{e}}_n + EI \frac{\partial^3 \Psi(s,t)}{\partial s^3} = 0 \quad (57)$$

where the global acceleration is

$$\underline{\ddot{r}}(s,t) = \underline{\ddot{x}}(s,t)\hat{\underline{i}} + \underline{\ddot{y}}(s,t)\hat{\underline{j}} \quad (58)$$

and the unit normal is

$$\hat{\underline{e}}_n = -\sin \Psi(s,t)\hat{\underline{i}} + \cos \Psi(s,t)\hat{\underline{j}} \quad (59)$$

The global  $x(s,t)$  and  $y(s,t)$  are related to the slope angle  $\Psi(s,t)$  by

$$\frac{\partial x(s,t)}{\partial s} = \cos \Psi(s,t) \quad x(s,t) = x(0,t) + \int_0^s \cos \Psi(\sigma,t) d\sigma \quad (60)$$

$$\frac{\partial y(s,t)}{\partial s} = \sin \Psi(s,t) \quad y(s,t) = y(0,t) + \int_0^s \sin \Psi(\sigma,t) d\sigma \quad (61)$$

If the second time derivatives of  $x(s,t)$  and  $y(s,t)$  in Eqs. (60) and (61) are taken, we see the transcendental integration of the unknown angle  $\Psi(s,t)$  over space will include terms with the first two time derivatives of  $\Psi(s,t)$ . This unknown angle  $\Psi(s,t)$  is also contained within trigonometric functions. The resulting  $x$  and  $y$  accelerations are dotted with the unit normal and then integrated over space  $s$  again to form the kinetic energy. This leads to a very complicated and non-standard integro-differential equation form for the equation of motion. The double spatial integrals and trigonometric functions in the kinetic energy greatly complicates any approximation of  $\Psi(s,t)$  and the resulting solution process.

#### 4.1.2 Finite Element Approach

##### *Principle of Virtual Work*

A method due to Epstein Murray<sup>9</sup> is paraphrased in this section. They developed a novel nonlinear formulation which is applied to problems involving large deformations of elastic beams. Their formulation is developed using the principle of virtual work and implemented using a finite element discretization of the beam displacements. The deformation of a beam is defined using two variables, axial displacement  $u$ , and transverse displacement  $w$ . Normal sections of the beam are assumed to remain plane undistorted and normal to the beam axis after deformation. In the equations that follow the symbol  $(\ )'$  denotes an  $s$  derivative. The position vector to a point on the axis of the beam is illustrated in Figure 12.

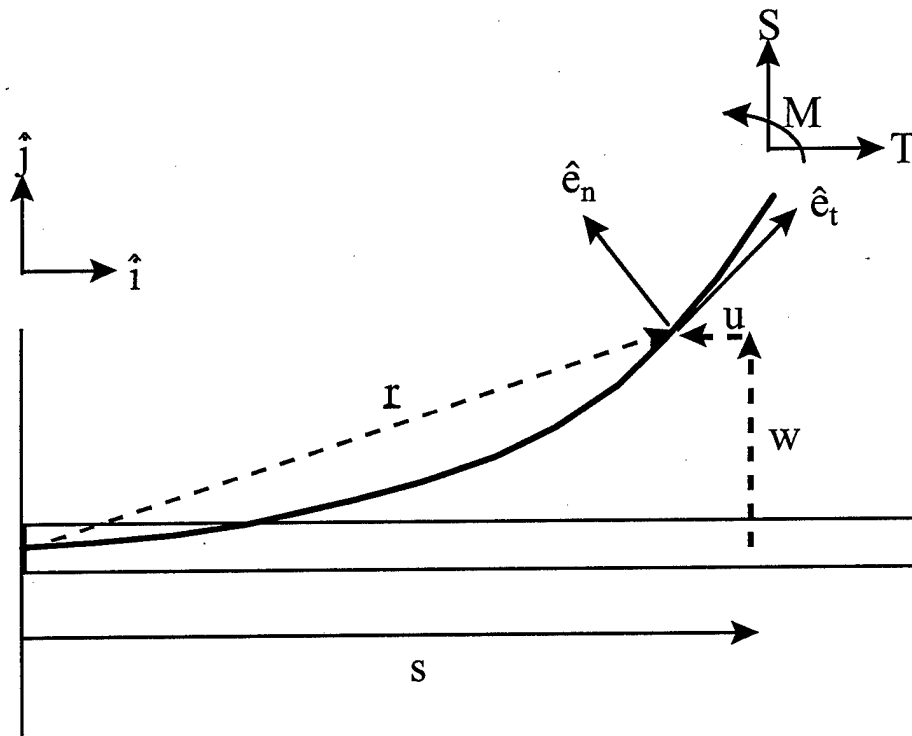


Figure 12. Finite element variables

The position vector to a point on the axis of the beam after deformation is given by

$$\underline{r} = (s + u)\underline{i} + w\underline{j} \quad (62)$$

where  $s$  is the position to the point before deformation (arclength measured along the undeformed beam). In Cartesian coordinates the position of the deformed point is,  $x = (s + u)$ , and  $y = w$ . The position of a general point not originally on the beam axis after deformation is given by

$$\underline{R} = \underline{r} + \alpha \underline{e}_n \quad (63)$$

The two dimensional Green's strain tensor is defined using derivatives of the position vector  $\underline{R}$ . The only nonzero component of the strain tensor is derived in terms of the axial strain  $e$  and curvature  $\kappa$  and the distance off the neutral axis  $\alpha$

$$\varepsilon = (1 - \kappa\alpha)^2 \left( e + \frac{1}{2} \right) - \frac{1}{2} \quad (64)$$

It is assumed that normal sections remain plane and undistorted after the deformation of the beam. The internal virtual work (IVW) is defined by the following volume integral

$$IVW = \int_{\hat{l}} \int_A \sigma \delta\varepsilon dA d\hat{l} \quad (65)$$

where  $\varepsilon$  is the 2-D Green Strain measure,  $\sigma$  is stress associated with  $\varepsilon$  and  $\hat{l}$  is the length of the beam axis after deformation. The variation of the strain component  $\varepsilon$  is taken and substituted into the above equation. The integral over the deformed length is converted to the integral over the original length using the definition of axial strain. After further algebraic manipulations, the terms are grouped into stress resultants and the following constitutive equations are used

$$\text{Modified internal force} = EAe \quad (66)$$

$$\text{Internal moment} = EI_c \bar{\chi} \quad (67)$$

The final result is

$$IVW = \int_0^l \left( EAe \delta e + EI_c \bar{\chi} \delta \bar{\chi} \right) dl \quad (68)$$

The Green Strain measure of the axis is given by

$$e = \frac{1}{2}(\hat{e}_t \cdot \hat{e}_t - \hat{i} \cdot \hat{i}) \quad (69)$$

where  $\hat{e}_t$  is the tangent vector along the beam axis after deformation and  $\hat{i}$  is the base vector along the undeformed beam axis. The tangent vector equals the derivative of the position vector given in Eq. (62). This derivative is taken and the axial strain  $e$  is written in terms of the displacements

$$e = u' + \frac{1}{2}(u'^2 + w'^2) \quad (70)$$

The Green Strain measure is also used to develop the relationship between the deformed length and the undeformed length

$$d\hat{l} = \sqrt{2e + 1} ds \quad (71)$$

The modified curvature  $\bar{\chi}$  is developed using the derivative of the normal vector  $\hat{e}_n$  and can be written in terms of the displacements  $u$ ,  $w$  and their derivatives

$$\bar{\chi} = w''(1 + u') - w'u'' \quad (72)$$

It is assumed that either end of the beam can be subjected to an external force  $T$  and  $S$  and a moment  $M$ . The external virtual work (EVW) expression for these boundary conditions would be

$$EVW_{ends} = (T \delta u + S \delta w + M \delta \Psi) \Big|_{s=0}^{s=l} \quad (73)$$



where the angle  $\Psi = \tan^{-1} \frac{w'}{1+u'}$  and its variation is  $\delta\Psi = \frac{1}{2e+1} [(1+u') \delta w' - w' \delta u']$ .

This is the same angle as the slope angle  $\Psi$  discussed in the static analysis. For small strains the denominator  $(2e+1)$  is taken equal to 1.

### Finite Element Discretization

A set of algebraic equations for Eq. (68) and Eq. (73) is developed using the finite element method of dividing the beam into elements and describing the displacement coordinates  $u$  and  $w$  in terms of shape functions and nodal (endpoint) displacements. For each element the displacements are

$$u(s,t) = \sum_{i=1}^4 f_i(s) u_i(t) \quad (74)$$

$$w(s,t) = \sum_{i=1}^4 f_i(s) w_i(t) \quad (75)$$

The shape functions chosen are the cubic polynomial functions.

$$f_1 = 1 - 3\left(\frac{s}{h}\right)^2 + 2\left(\frac{s}{h}\right)^3 \quad (76a)$$

$$f_2 = h\left(\left(\frac{s}{h}\right) - 2\left(\frac{s}{h}\right)^2 + \left(\frac{s}{h}\right)^3\right) \quad (76b)$$

$$f_3 = 3\left(\frac{s}{h}\right)^2 - 2\left(\frac{s}{h}\right)^3 \quad (76c)$$

$$f_4 = h\left(-\left(\frac{s}{h}\right)^2 + \left(\frac{s}{h}\right)^3\right) \quad (76d)$$

where  $h$  is the length of the  $I$ th element. The beam elements, nodal displacements and the numbering scheme for  $u$  and  $w$  are illustrated in Figure 13.

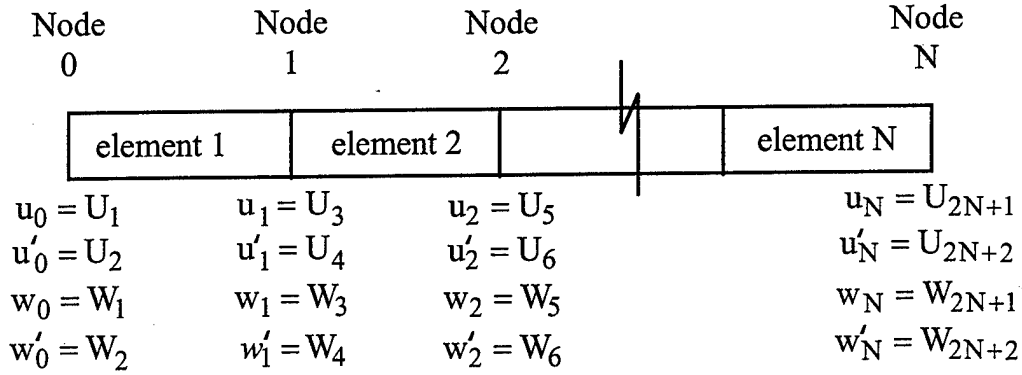


Figure 13. Element, node and displacement numbering

The displacement discretizations are used in the equations for the strain measure  $e$ , Eq. (70) and the curvature  $\bar{\chi}$ , Eq. (72) and their first variations. This is substituted into the expressions for IVW, Eq. (68) and EVW, Eq. (73). The resulting equations are

$$IVW = \sum_{I=1}^N h_I \{ N_j^* \delta U_{2(I-1)+j} + N_{jk}^{**} (W_{2(I-1)+j} \delta W_{2(I-1)+k} + U_{2(I-1)+j} \delta U_{2(I-1)+k}) + M_j^* \delta W_{2(I-1)+j} + (U_{2(I-1)+k} \delta W_{2(I-1)+j} + W_{2(I-1)+j} \delta U_{2(I-1)+k}) \times (M_{jk}^{**} - M_{kj}^{**}) \} \quad (77)$$

where

$$N_j^* = EA \left[ U_{2(I-1)+k} F'_{jk} + \frac{1}{2} (W_{2(I-1)+k} W_{2(I-1)+m} + U_{2(I-1)+k} U_{2(I-1)+m}) F'_{jkm} \right]$$

$$N_{jk}^{**} = EA \left[ U_{2(I-1)+m} F'_{jkm} + \frac{1}{2} (W_{2(I-1)+m} W_{2(I-1)+n} + U_{2(I-1)+m} U_{2(I-1)+n}) F'_{jkmn} \right]$$

$$M_j^* = EI \left[ W_{2(I-1)+k} F''_{jk} + W_{2(I-1)+k} U_{2(I-1)+m} F''_{jkmn} - W_{2(I-1)+k} U_{2(I-1)+m} F''_{jmk} \right]$$

$$M_{jk}^{**} = EI \left[ W_{2(I-1)+m} F''_{jmk} + W_{2(I-1)+m} U_{2(I-1)+n} F''_{jkmn} - W_{2(I-1)+m} U_{2(I-1)+n} F''_{jnmk} \right]$$

The upper case subscript  $I$  represents the element number. The lower case subscripts  $j$ ,  $k$ ,  $m$ , and  $n$  appearing as indices in two adjacent terms represent summations for each index from 1-4. For example the term  $W_{2(I-1)+m}U_{2(I-1)+n}F''_{jmkcn}$  represents the summation of 16 terms with  $m=1,4$  and  $n=1,4$ . The  $F$  terms represent integral evaluations of the shape functions first and second derivatives. For example

$$F''_{jmkcn} = \int_0^1 f_j'' f_m'' f_k' f_n' d\zeta \quad \text{where } \zeta = \frac{s}{h}.$$

The external virtual work expression is brought to the algebraic form

$$EVW = \sum_{I=0}^N \left\{ X_I \delta U_{2I+1} + Y_I \delta W_{2I+1} + M_I \left[ (1 + U_{2I+2}) \delta W_{2I+2} - W_{2I+2} \delta U_{2I+2} \right] \right\} \quad (78)$$

where  $Y_I$  and  $X_I$  represent the transverse force and longitudinal force respectively at node  $I$ , and  $M_I$  represents the moment at node  $I$ . The equilibrium equations are determined by assuming all but one variation of the nodal coordinates vanish. There are two contributions from adjacent elements for each nodal equilibrium equation. There are four coordinates at each node so four equations are generated at each node. The following four equations apply at each node

$\delta W_{2m+1}$ :

$$\begin{aligned} h_{m+1} \left[ M_1^* + N_{j1}^{**} W_{2m+j} + (M_{1j}^{**} - M_{j1}^{**}) U_{2m+j} \right] + \\ h_m \left[ M_3^* + N_{j3}^{**} W_{2(m-1)+j} + (M_{3j}^{**} - M_{j3}^{**}) U_{2(m-1)+j} \right] = Y_m \end{aligned} \quad (79)$$

$\delta W_{2m+2}$ :

$$h_{m+1} \left[ M_2^* + N_{j2}^{**} W_{2m+j} + (M_{2j}^{**} - M_{j2}^{**}) U_{2m+j} \right] +$$

$$h_m \left[ M_4^* + N_{j4}^{**} W_{2(m-1)+j} + (M_{4j}^{**} - M_{j4}^{**}) U_{2(m-1)+j} \right] = M_m (1 + U_{2m+2}) \quad (80)$$

$\delta U_{2m+1}$ :

$$h_{m+1} \left[ N_1^* + N_{j1}^{**} U_{2m+j} + (M_{j1}^{**} - M_{1j}^{**}) W_{2m+j} \right] +$$

$$h_m \left[ N_3^* + N_{j3}^{**} U_{2(m-1)+j} + (M_{j3}^{**} - M_{3j}^{**}) W_{2(m-1)+j} \right] = X_m \quad (81)$$

$\delta U_{2m+2}$ :

$$h_{m+1} \left[ N_2^* + N_{j2}^{**} U_{2m+j} + (M_{j2}^{**} - M_{2j}^{**}) W_{2m+j} \right] +$$

$$h_m \left[ N_4^* + N_{j4}^{**} U_{2(m-1)+j} + (M_{j4}^{**} - M_{4j}^{**}) W_{2(m-1)+j} \right] = -M_m W_{2m+2} \quad (82)$$

The subscript  $m$  in the above expressions represents a node number from 0 to  $N$ . The equations generated are nonlinear due to the multiplication of the  $U$  and  $W$  variables. Therefore a conventional linear stiffness matrix cannot be formed. The equations for all the nodes can be grouped in vector form

$$\{NLT(q)\} = \{Q(q)\} \quad (83)$$

where  $q^T = \{W_1, W_2, U_1, U_2, W_3, W_4, U_3, U_4, \dots, W_{2N+1}, W_{2N+2}, U_{2N+1}, U_{2N+2}\}$

The virtual work done by the internal forces are nonlinear terms and are denoted simply by the  $NLT$  vector. The  $Q$  vector represents the nonconservative work vector. The only solution approach known for integrating this nonlinear system is direct numerical integration. We adopt a 4<sup>th</sup> order Runge Kutta integration scheme to solve for the nodal forces and moments given a shape  $q$ . Since the usual problem is to find the static shape

given a force distribution, a Newton's method is used to solve for the roots of the set of nonlinear equations.

$$\text{Let } b(q) = \{NLT(q)\} - \{Q(q)\} \quad (84)$$

then a Taylor series expansion about the nth iteration  $q_n$  is

$$\begin{aligned} b_1(q)_{n+1} &= b_1(q)_n + \frac{\partial b_1}{\partial q_1} \Big|_n (q_{1n+1} - q_{1n}) + \dots + \frac{\partial b_1}{\partial q_{4N}} \Big|_n (q_{4Nn+1} - q_{4Nn}) \\ b_2(q)_{n+1} &= b_2(q)_n + \frac{\partial b_2}{\partial q_1} \Big|_n (q_{1n+1} - q_{1n}) + \dots + \frac{\partial b_2}{\partial q_{4N}} \Big|_n (q_{4Nn+1} - q_{4Nn}) \\ &\vdots \\ b_{4N}(q)_{n+1} &= b_{4N}(q)_n + \frac{\partial b_{4N}}{\partial q_1} \Big|_n (q_{1n+1} - q_{1n}) + \dots + \frac{\partial b_{4N}}{\partial q_{4N}} \Big|_n (q_{4Nn+1} - q_{4Nn}) \end{aligned} \quad (85)$$

This requires first order derivatives of each nonlinear equation with respect to each variable in  $q$ . The derivatives of the equations with respect to these variables can be grouped to form the Jacobian matrix. The Jacobian matrix is straightforward to program but is a computationally time consuming task due to all the summations in the multiplication of the coordinates.

### *Hamilton's Formulation*

The equations of motion are formulated using Hamilton's principle for ease of introducing the kinetic energy terms and allowing the conservation of energy to be verified. Hamilton's principle divides the energy into a potential energy  $V$ , a kinetic energy  $T$ , and a nonconservative work term  $W_{nc}$ .

$$\int_{t_1}^{t_2} \delta(T - V) dt + \int_{t_1}^{t_2} \delta W_{nc} dt = 0 \quad (86)$$

The potential energy function due to the strain energy of axial deformation and transverse deflection is

$$V = \frac{1}{2} \int_0^l \left( EAe^2 + EI_c \chi^2 \right) ds \quad (87)$$

The variation of the potential function is consistent with the variation of internal virtual work developed in Eq. (77). The resulting nodal equations Eqs.(79) - (82) can be directly imported to this development.

The kinetic energy expression can be derived using the position vector

$$\underline{r} = (s + u)\underline{\hat{i}} + w\underline{\hat{j}} \quad (88)$$

Since the components are in inertial coordinates, the velocity is simply

$$\dot{\underline{r}} = \dot{u}\underline{\hat{i}} + \dot{w}\underline{\hat{j}} \quad (89)$$

The kinetic energy expression is

$$T = \frac{1}{2} \int_0^l \rho (\dot{u}^2 + \dot{w}^2) ds \quad (90)$$

where  $\rho$  is the mass/length of the beam. The variation of the kinetic energy is

$$\delta T = - \int_0^l \rho [\ddot{u} \delta u + \ddot{w} \delta w] ds \quad (91)$$

Discretizing the variables  $u$  and  $w$  using the same finite element shape functions in Eqs. (76a) - (76d) yields

$$\delta T = \sum_{I=1}^N h_I \left[ \rho \left( \ddot{U}_{2(I-1)+j} F_{jk} \delta U_{2(I-1)+k} + \ddot{W}_{2(I-1)+j} F_{jk} \delta W_{2(I-1)+k} \right) \right] \quad (92)$$

Again the lower case subscripts represent summations from 1-4 so the group expressions for  $U$  and  $W$  represents the sum of 16 terms. The  $F_{jk}$  term represents the integral evaluations of the shape functions listed in Eq. (76)

$$F_{jk} = \int f_j f_k d\zeta \quad \text{where } \zeta = \frac{s}{h} \quad (93)$$

The dynamic equations of motion are developed from the kinetic energy variations assuming all but one of the node variations vanish. There are four equations generated for each node and in each equation there is a contribution term from each element adjoining the node.

$$\delta W_{2m+1} : h_{m+1} \rho [\ddot{W}_{2m+j} F_{j1}] + h_m \rho [\ddot{W}_{2(m-1)+j} F_{j3}] \quad (94)$$

$$\delta U_{2m+1} : h_{m+1} \rho [\ddot{U}_{2m+j} F_{j1}] + h_m \rho [\ddot{U}_{2(m-1)+j} F_{j3}] \quad (95)$$

$$\delta W_{2m+2} : h_{m+1} \rho [\ddot{W}_{2m+j} F_{j2}] + h_m \rho [\ddot{W}_{2(m-1)+j} F_{j4}] \quad (96)$$

$$\delta U_{2m+2} : h_{m+1} \rho [\ddot{U}_{2m+j} F_{j2}] + h_m \rho [\ddot{U}_{2(m-1)+j} F_{j4}] \quad (97)$$

The lower case subscript  $j$  represents a summation index from 1-4 and  $m$  represents a node number from 0 to N. An element mass matrix can be constructed by writing these expressions in matrix form and a global mass matrix is developed by combining the element matrices. Any point masses can be added to the appropriate location in the mass matrix. Combining these results with the potential energy results, the dynamic equations of motion are

$$[M]\ddot{\underline{q}} + \{NLT(\underline{q})\} = \{Q(\underline{q}, \dot{\underline{q}})\} \quad (98)$$

For this nonlinear system, the only solution approach known is some form of direct numerical integration. Numerical integration is most conveniently done in terms of first order equations, which requires Eq. (98) be rewritten in state space form.

$$\text{let } \underline{v} = \begin{Bmatrix} v_1 \\ v_2 \end{Bmatrix} = \begin{Bmatrix} \underline{q} \\ \dot{\underline{q}} \end{Bmatrix}$$

$$\text{then } \dot{\underline{v}} = \begin{Bmatrix} \dot{v}_1 \\ \dot{v}_2 \end{Bmatrix} = \begin{Bmatrix} v_2 \\ [M]^{-1} \{Q(\underline{q}, \dot{\underline{q}}) - NLT(\underline{q})\} \end{Bmatrix} \quad (99)$$

A 4<sup>th</sup> order Runge Kutta integration scheme is used to solve for the shape and velocity over time.

#### Friction Forces

The nonconservative forces and moments are included in the generalized force vector  $Q$ . Only friction forces are included as non-conservative forces in this study. The generalized force is developed for the sliding friction between a mass at a point on the beam system and the supporting surface. The variation of the nonconservative work is



$$\delta W_{nc} = \underline{F}_{fr} \cdot \delta \underline{r} \quad (100)$$

and the friction force is

$$\underline{F}_{fr} = -\mu N \text{sign}(\dot{\underline{r}}_{pt}) \quad \text{where } N = \text{mass} \cdot \text{gravity} \quad (101)$$

The variation and time derivative of  $\underline{r}$  is taken from Eq. (89). The nonconservative work becomes

$$\delta W_{nc} = -\mu N \text{sign}(\dot{u}_{pt}) \delta u_{pt} - \mu N \text{sign}(\dot{w}_{pt}) \delta w_{pt} \quad (102)$$

and the coefficients of the variations are added to the generalized force vector  $Q$  at the appropriate locations.

### Constrained Boundary Conditions

Constraint equations are introduced to impose boundary conditions and to allow the coordinates associated with a fixed support to be removed from the solution process. For a clamped boundary condition, the  $w$ ,  $w'$  and  $u$  coordinates are constrained to be zero. The constraints are written in matrix form

$$\begin{bmatrix} 1 & 0 & 0 & 0 & 0 & 0 & \dots & 0 \\ 0 & 1 & 0 & 0 & 0 & 0 & \dots & 0 \\ 0 & 0 & 1 & 0 & 0 & 0 & \dots & 0 \end{bmatrix} \left\{ \underline{q} \right\} = \begin{Bmatrix} 0 \\ 0 \\ 0 \end{Bmatrix} \quad (103)$$

Let the matrix on the left hand side be represented by  $C$ . Lagrange multipliers are introduced and used to multiply the constraint variations. This allows the constraints to be included in the equations of motion as

$$[M]\ddot{\underline{q}} + \{NLT(\underline{q})\} = \{Q(\underline{q}, \dot{\underline{q}})\} + C^T \underline{\lambda} \quad (104)$$

The Lagrange multipliers  $\lambda$  are determined by differentiating the constraint equation, substituting in the equation of motion for  $\ddot{\underline{q}}$  and solving for  $\lambda$

$$\underline{\lambda} = [CM^{-1}C]^{-1} CM^{-1} \{NLT(\underline{q}) - Q(\underline{q}, \dot{\underline{q}})\} \quad (105)$$

The expression for  $\lambda$  is now substituted into Eq. (104) and the revised equations of motion become

$$[M]\ddot{\underline{q}} + \{NLT(\underline{q})\} = \{Q(\underline{q}, \dot{\underline{q}})\} + C^T [CM^{-1}C]^{-1} CM^{-1} \{NLT(\underline{q}) - Q(\underline{q}, \dot{\underline{q}})\} \quad (106)$$

The state space form of this differential equation becomes

$$\underline{v} = \begin{Bmatrix} \underline{v}_1 \\ \underline{v}_2 \end{Bmatrix} = \begin{Bmatrix} \underline{q} \\ \dot{\underline{q}} \end{Bmatrix}$$

and

$$\underline{f} = \dot{\underline{v}} = \begin{Bmatrix} \dot{\underline{v}}_1 \\ \dot{\underline{v}}_2 \end{Bmatrix} = \left\{ [M]^{-1} \left[ \{Q(\underline{q}, \dot{\underline{q}}) - NLT(\underline{q})\} \begin{matrix} \underline{v}_2 \\ \left\{ I - C^T (CM^{-1}C^T)^{-1} CM^{-1} \right\} \end{matrix} \right] \right\} \quad (107)$$

The Runge Kutta 4th order integration technique is used to solve these equations for the displacement shape over time. The computer code developed for the forward solution of the nonlinear finite element model is listed in reference 14.

#### 4.1.3 Model Validation

Several methods are used to validate the nonlinear finite element model. These include matching the static deformation shapes obtained from the arc length model, matching

results from classical linear models with small deformations, and checking the conservation of energy.

### *Verification Using the Arc Length Approach*

The equilibrium shapes obtained from the finite element approach and the arc length approach are compared for two loading conditions. The first comparison is for the cantilever beam system acted on by a moment at the free end. This example was used in Figure 6 for comparing the arc length approach to the exact solution. Figure 14 shows the finite element solution using four elements and the arc length solution for various moments.

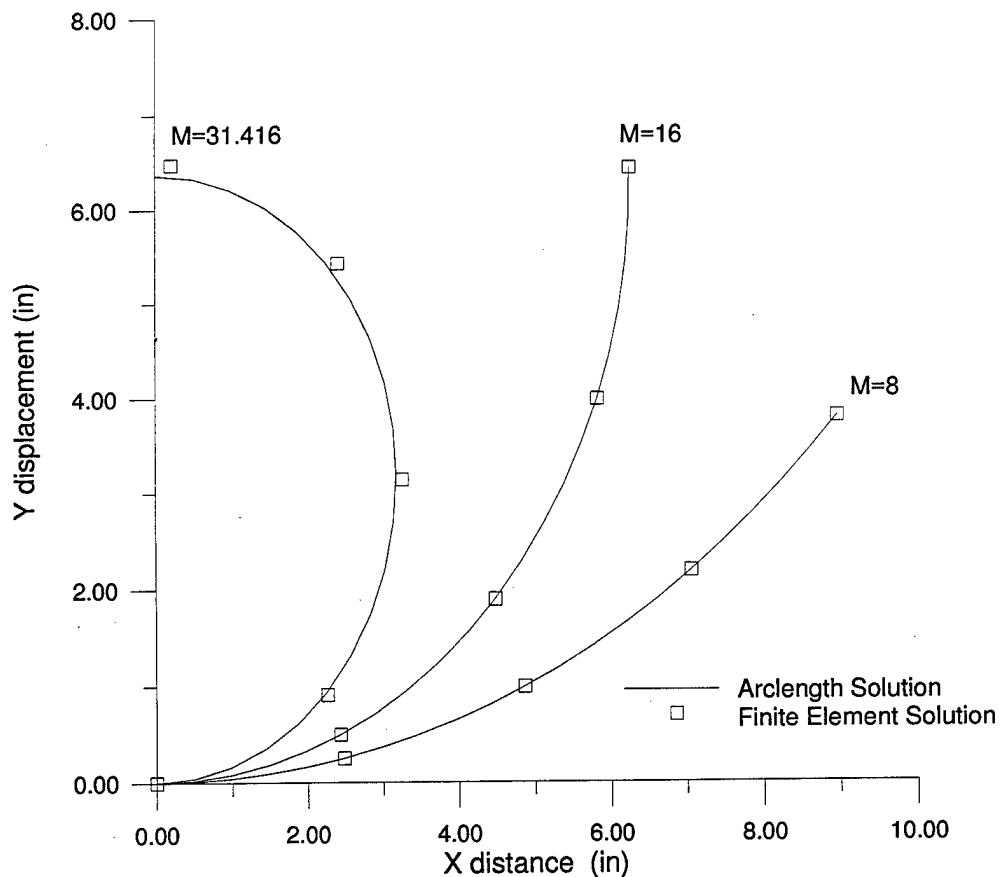


**Figure 14. Comparison of deflections due to tip moment**

The finite element approach agrees well with the arc length solution for even larger deformations caused by a pure bending moment. For a static's problem with a pure bending moment, the two methods are theoretically equivalent to within the finite element discretization and convergence errors. If the number of elements is increased to eight, the finite element method results are graphically identical to the arc length results for these bending moments. This indicates rapid convergence of the spatial discretization approximation to the arc length solution of Chapter III.

The second validation comparison makes use of the two beam PACE system with beam properties listed in Table 1. This system is subjected to an external force acting on the free end. The force has transverse and longitudinal components. The prototype mechanism designed by I. Romero allows the static tip force to be directed anywhere within the plane of the beam. The finite element approach is applied to a variety of loading configurations. For the loading condition above the buckling force, there are two solution shapes obtained from the finite element model depending on the initial conditions used to start the nonlinear iteration. This lack of uniqueness occurs only above the critical buckling load. This is demonstrated in Figure 15. The lines labeled *a* and *b* illustrate the two solutions obtained for the same transverse and longitudinal forces. The net force applied on line *b* is an axial compressive type force, where the net force on line *a* is more of a transverse compressive force. They are not mirror images of each other because of the effects of the axial versus transverse loading. The lines *a* and *a'* do represent mirror images where the longitudinal force is the same and the transverse forces are of opposite sign. Line *b'* is the other nonlinear solution corresponding to the same loading as line *a'*. It is a mirror image of line *b*. The critical buckling load is calculated to be 12.7 N, and the loads represented in Figure 15 have a longitudinal force of -15 N and a transverse force of +.9 N or -.9 N.

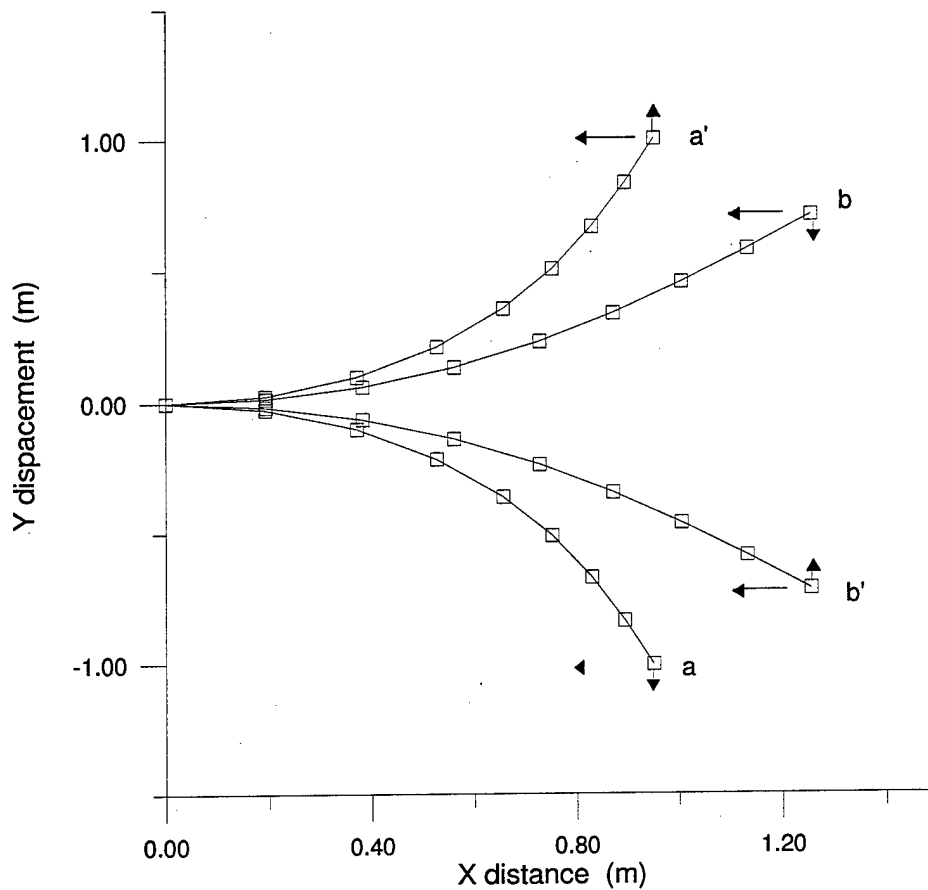


**Figure 15. Finite element solutions for tip force**

It is difficult to compare the shapes obtained from a force boundary condition on the finite element model to the arc length results since the arc length modeling approach of Chapter III does not include the effects of axial deformation. Therefore the models are compared in Figure 16 for small transverse loading configurations. It is expected that the two nonlinear solutions will converge toward each other and the classical Euler Bernoulli analytical solution for small deformations.

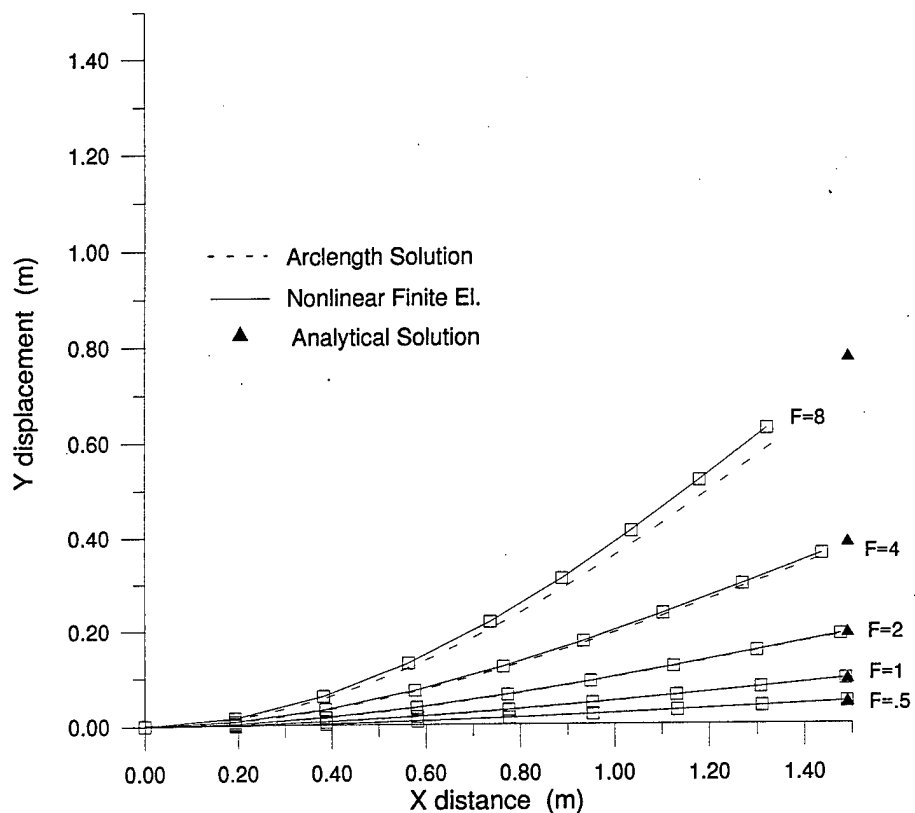


**Figure 16. Comparison of methods for tip loading**

The three methods agree well for small transverse loading but as expected, the axial effects become increasingly significant for larger deformations and the methods start to diverge.

#### *Static Verification for Linear Systems*

The nonlinear finite element model is checked to make sure it recovers the classical results of a beam undergoing axial deformation. The equilibrium equation for a linearly elastic bar is

$$\frac{d}{dx} \left( AE \frac{du}{dx} \right) = 0 \quad (108)$$

If the bar is cantilevered on one end and subjected to an axial load  $p$  on the other, the analytical solution is

$$u(x) = \frac{P}{AE} x \quad (109)$$

The axial strain  $du/dx$  is determined and compared to the results of the finite element solution for various forces. The results are listed in Table 6.

Table 6. Axial strain comparison		
Axial Force	Strain - Finite El	Strain - Analytic
-5	-.364500e-06	-.364500e-06
-12	-.874800e-06	-.874799e-06
-15	-1.093501e-06	-1.093499e-06
-20	-1.458002e-06	-1.457999e-06

The axial strain produced from the nonlinear finite element model matches the analytical solution for various compressive loads.

The nonlinear finite element model is also checked against the analytical solution for a beam with a transverse load. The equilibrium equation for the transverse deflection of an Euler Bernoulli beam is

$$\frac{d^2}{dx^2} \left( EI \frac{d^2 y}{dx^2} \right) = 0 \quad (110)$$

The analytical solution for a cantilever beam of length  $L$  subjected to a tip force  $F$  is

$$y(x) = \frac{Fx^2}{EI}(3L - x) \quad (111)$$

The two beam PACE system is subjected to various tip forces and the tip deflections are shown in Figure 16. Both the finite element and arc length methods agree with the analytical solution for small loads but as expected do not agree with it for larger deformations since the Euler Bernoulli beam does not include foreshortening effects.

#### *Linear Finite Element Dynamic Solution*

A linear finite element model is constructed for the PACE two beam system. The mathematical model is developed using the strain energy and kinetic energy of a beam undergoing axial and transverse vibration<sup>15</sup>. The potential energy function includes terms for the strain energy due to axial motion  $w$  and the bending energy due to a transverse deflection  $u$  of an Euler Bernoulli beam

$$V = \frac{1}{2} \int_0^l (EA(u')^2 + EI(w'')^2) ds \quad (112)$$

The kinetic energy due to axial and transverse displacements is

$$T = \frac{1}{2} \int_0^l \rho A (\dot{u}^2 + \dot{w}^2) ds \quad (113)$$

The beam is divided into elements and the displacement coordinates  $u$  and  $w$  are approximated using the element end displacements and shape functions. The cubic polynomial shape functions listed in Eqs. (76a) - (76d) and the four endpoint coordinates in Eq. (74) are used for the transverse displacement  $w$ . The following coordinate approximation and two linear shape functions are used for the axial displacement  $u$



$$u(s,t) = \sum_{i=1}^2 f_i(s)u_i(t)$$

$$f_1(s) = 1 - \frac{s}{h}$$

$$f_2(s) = \frac{s}{h}$$
(114)

The element mass and stiffness matrices are constructed using the element approximations in the potential and kinetic energy expressions and evaluating the integrals of the shape functions. The element matrices are combined to give the global mass and stiffness matrices and Lagrange's equations are used to derive the following equation of motion

$$M\ddot{q} + Kq = Q(q, \dot{q})$$
(115)

The analysis of this linear model is used to help verify the nonlinear model and used to give several insights to the expected behavior. The natural frequencies and mode shapes are determined for this system assuming a free vibration response. For the PACE two beam system with eight elements, there are 24 natural frequencies. Table 7 lists some of the natural frequencies of interest.

Transverse	2.4288 rad/s	Axial	16251.27 rad/s
frequencies	11.0030 rad/s	frequencies	27798.63 rad/s
	102.7105 rad/s		40387.25 rad/s
	...		....
	7011.423 rad/s		95707.21 rad/s

The lower frequencies correspond to transverse vibration and the first three have periods of 2.6 seconds, 0.57 seconds and 0.061 seconds. The higher frequencies correspond to axial vibrations and the periods range from  $3.87e-04$  seconds to  $0.657e-04$  seconds. The mode shapes  $\Phi = [\phi_1, \phi_2, \dots, \phi_n]$  and frequencies  $\omega$ , are used to transform the coordinates  $q$  to modal coordinates  $\eta$  and uncouple the linear model equations.

$$\text{Let } \underline{q}(t) = \Phi \underline{\eta}(t) \quad (116)$$

then the analytical solution becomes

$$\underline{q}(t) = \Phi \underline{\eta}(0) \cos(\omega t) \quad (117)$$

The equations are solved analytically for a free vibration problem starting from an initial deformation shape and the results are compared to the nonlinear finite element solution. A numerical solution of Eq. (115) is also determined and used to check the Runge Kutta integration algorithm. The shape used for the initial deformation corresponds to the static transverse load of  $F=8$  shown in Figure 16 for the nonlinear finite element solution is. This shape is used instead of the static solution to Eq. (115) since the same starting shape is needed to compare the free vibration response. Table 8 compares the tip transverse deflections over the time period 2.6 seconds for the three methods.

Time	Analytical-Linear FE	Integration-Linear FE	Nonlinear FE
.1 sec	.6037445 m	.6037453 m	.6046646 m
.2 sec	.5405400 m	.5405403 m	.5424933 m
1.0 sec	-.4671448 m	-.4671460 m	-.4792404 m
2.0 sec	.0799039 m	.0799040 m	.0957824 m
2.6 sec	.6083068 m	.6083096 m	.6071464 m

The numerical solution compares closely with the analytical solution. The nonlinear finite element solution agrees with both linear solutions to within small errors in the third digit. This comparison is shown graphically in Figure 17.

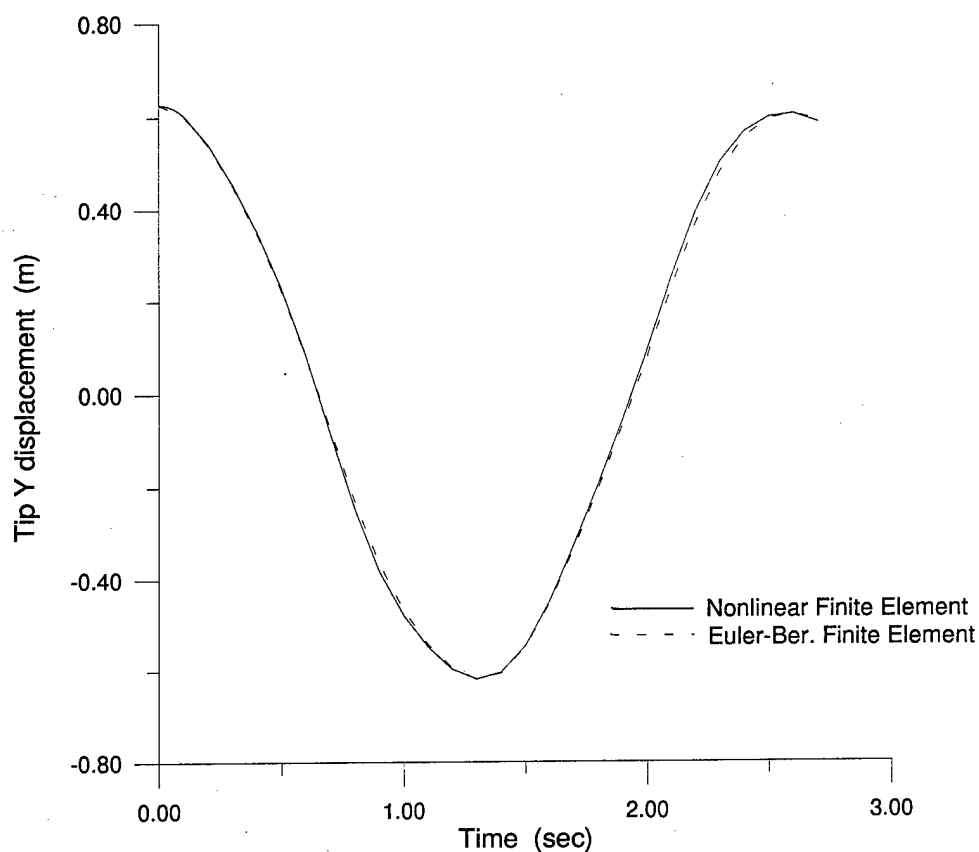


**Figure 17. Free vibration comparison of methods**

The nonlinear finite element method closely matches the transverse deflections of the linear finite element model. This graph does not reflect the axial displacements of the tip which the nonlinear model accounts for. The linear finite element model does not have the coupling between the transverse and axial motions. It is of significance, however, to note

that accurate numerical solutions require Runge Kutta time steps which are a fraction of the shortest period participating in the response.

### *Conservation of Energy*

A check of the conservation of energy for the system is another way to verify that the results of the dynamic model are logical. The sum of the potential and kinetic energy over time should be constant in the absence of nonconservative forces. If there are nonconservative forces, the change in the energy over time should equal the work done by these forces<sup>16</sup>. The potential energy expression for the nonlinear model is listed in Eq. (87), and the expressions for axial strain and curvature are listed in Eq. (70) and Eq. (72). The finite element discretizations are introduced at this level and the potential energy is written as

$$V = \frac{1}{2} \sum_{I=1}^N h_I \left\{ \begin{array}{l} \left[ \begin{array}{l} U_{2(I-1)+j} U_{2(I-1)+k} F'_{jk} + \\ \frac{1}{4} F''_{jkmn} (U_{2(I-1)+j} U_{2(I-1)+k} U_{2(I-1)+m} U_{2(I-1)+n} \\ EA + 2U_{2(I-1)+j} U_{2(I-1)+k} W_{2(I-1)+m} W_{2(I-1)+n} \\ + W_{2(I-1)+j} W_{2(I-1)+k} W_{2(I-1)+m} W_{2(I-1)+n} \\ + U_{2(I-1)+j} F'_{jkm} (U_{2(I-1)+k} U_{2(I-1)+m} + W_{2(I-1)+k} W_{2(I-1)+m}) \end{array} \right] \\ + EI \left[ \begin{array}{l} W_{2(I-1)+j} W_{2(I-1)+k} F''_{jk} + W_{2(I-1)+j} W_{2(I-1)+k} U_{2(I-1)+m} F''_{jkm} \\ + W_{2(I-1)+j} W_{2(I-1)+k} U_{2(I-1)+m} U_{2(I-1)+n} (F''_{jkmn} + F''_{mnjk}) \\ - 2(W_{2(I-1)+j} U_{2(I-1)+k} W_{2(I-1)+m} F''_{kmj}) \\ + W_{2(I-1)+j} U_{2(I-1)+k} W_{2(I-1)+m} U_{2(I-1)+n} F''_{knjn} \end{array} \right] \end{array} \right\} \quad (118)$$

where the expressions for  $F''_{jkm}$  are combinations of shape function derivatives evaluated over the integral 0 to 1, and the lower case indices represent summations from 1 to 4. The determination of the kinetic energy is simpler since the mass matrix is already determined.

$$T = \frac{1}{2} \underline{\dot{q}}^T M \underline{\dot{q}} \quad (119)$$

The dissipative work done by nonconservative forces is

$$W_{nc} = \int_0^t \underline{F} \cdot \underline{\dot{r}} dt \quad (120)$$

and taking the time derivative, the power (work rate) equation becomes

$$\dot{W}_{nc} = \underline{F} \cdot \underline{\dot{r}} \quad (121)$$

This equation can be numerically integrated over time along with the displacement variables. Friction forces are included in the finite element model and that force is described in Eq. (101). The derivative of the nonconservative work for a friction force at location  $pt$  is

$$\dot{W}_{nc} = -\mu N \left( \dot{u}_{pt} \text{sign}(\dot{u}_{pt}) + \dot{w}_{pt} \text{sign}(\dot{w}_{pt}) \right) \quad (122)$$

During the dynamic motion, the numerical value of this work should equal the change in the total energy of the system. This work integral computed energy change is used to check the instantaneous energy in all of the simulation results.

#### 4.1.4 Model Refinement

##### *Time Step Analysis*

The integration time step chosen for the Runge Kutta numerical solution is based on an analysis of a similar linear problem. The linear problem is derived by taking the

dynamic nonlinear model in Eq. (98), separating out a linear stiffness matrix operating on the displacement variables and grouping the remaining terms in a nonlinear vector.

$$M\ddot{\underline{q}} + K\underline{q} + NLT(\underline{q}) = Q(\underline{q}, \dot{\underline{q}}) \quad (123)$$

The nonlinear vector  $NLT$  is neglected in the linear analysis. The resulting linear model is qualitatively similar to the linear model used in the dynamic verification Eq. (115). The difference between the models is due to using the cubic shape functions in Eqs. (76a - 76d) for both variables  $u$  and  $w$  in Eq.(123). The natural frequencies and mode shapes are determined using the following open loop eigenvalue problem

$$K \underline{\phi}_i = \omega_i^2 M \underline{\phi}_i \quad (124)$$

The mode shapes are normalized using the mass matrix

$$\underline{\phi}_i^T M \underline{\phi}_i = 1 \quad i = 1, 2, \dots, n \quad (125)$$

and

$$\underline{\phi}_i^T K \underline{\phi}_i = \omega_i^2 \quad i = 1, 2, \dots, n \quad (126)$$

The frequencies are determined for an 8 element linear model of the two beam PACE system. The lowest frequency is 2.42882 rad/s and the highest computed frequency is 180075.56 rad/s which correspond to the periods 2.587 seconds, and 0.3489e-04 seconds respectively. Although the higher computed frequencies are poorly converged in the finite element analysis, their small participation in the solution will lead to numerical stability problems if ignored altogether. A time step of .1e-04, which is one third of the shortest period, allows a stable integration of the nonlinear finite element model to proceed. Significantly larger time steps cause the motion to diverge due to numerical instability typical of stiff differential equations. The time step must be small enough to track the high

frequency dynamics for stability of the numerical method. When accurately integrated, the higher frequencies and mode shapes do not have a large affect on the dynamic response as are seen graphically in the results. The lowest frequency corresponds to a period of 2.587 seconds. Unfortunately for a stable integration over the largest period a large number of integration steps are required. This motivated a search for an order reduction method to eliminate the high frequency coordinates.

#### *Number of Elements*

The total number of elements used in the nonlinear finite element method is based on an analysis of the linear model analogous to the preceding section and based on a convergence study of the nonlinear initial deformation. The natural frequencies for the similar linear PACE model are determined for three cases of different element numbers and are grouped according to transverse  $w$  modes or longitudinal  $u$  modes. Table 9 and Table 10 lists some of the frequencies that can be compared for different numbers of elements used in the linear model.

4 elements	8 elements	16 elements
2.42882	2.42882	2.42882
11.0030	11.0030	11.0030
103.234	102.710	102.675
165.081	163.049	162.889
419.539	373.378	371.689
586.853	472.479	469.017

4 elements	8 elements	16 elements
1711.09	1705.61	1702.87
4784.38	4732.07	4706.50
21120.4	20952.8	20854.1
24195.5	23665.4	23440.9
42434.9	41691.0	41465.0

The lower frequencies of the 8 element model agree closely with the 16 element frequencies and the higher frequencies agree within 1% or less. The frequencies for the 4 element model are not converged as well with the 16 element frequencies and the differences range from 0% to 25%. The differences between the frequencies are more pronounced for the transverse modes.

The effect of the number of elements on the initial nonlinear deformation shape is analyzed. The nonlinear static deformation shape is solved using Eq. (83) for two different tip loading conditions. Table 11 lists the tip displacement variables for different numbers of elements due to a moment applied at the tip.

# Elements	$W_{tip}$	$W'_{tip}$	$u_{tip}$	$u'_{tip}$
4	1.0772644	.7176522	-1.027003	-1.696657
8	1.0777037	.7018290	-1.043144	-1.712356
16	1.0776955	.7017399	-1.043231	-1.712428
32	1.0776949	.7017383	-1.043232	-1.712429



The 8 element model agrees well with the 16 element model. The values of the displacements for the 8 element model agree to within 4 digits of the higher element models. Another deformation shape is analyzed for models with different numbers of elements. In this case a static transverse force is applied to the beam tip. The resulting tip displacements are shown in Table 12.

# Elements	$w_{tip}$	$w'_{tip}$	$u_{tip}$	$u'_{tip}$
4	.620976	.610819	-.167227	-.208298
8	.627036	.611709	-.169576	-.208926
16	.628348	.612011	-.170073	-.209151
32	.628433	.612040	-.170106	-.209172

The displacements for all the different element models agree to within 2 digits. The biggest improvement appears to be between increasing from 4 elements to 8 elements. For the 8 element model the values of the  $w$  and  $u$  coordinates are within .0003 to .0014 of the coordinate values for the 32 element model.

Based on the results of the linear frequencies and the static deformation shapes, the 8 element model is chosen for the simulation study and parameter recovery method.

#### *Modal Truncation*

For the 8 element nonlinear model, a small time step is needed for the stability of the integration method. In an effort to allow larger time steps, an attempt is made to truncate the finite element model. This order reduction is motivated by a conventional method used for linear problems. The most common order reduction method for structural dynamics is the modal truncation technique. The linear finite element model is transformed to modal coordinates and the high frequency low amplitude modes which do

not contribute significantly to the dynamics are partitioned out. Skelton's<sup>17</sup> idea of a modal cost function is used to rank the modes' relative importance to the dynamic solution depending, in essence, on the fractional distribution of the system energy among the modes. The mode shapes and frequencies obtained in Eq. (124) are used for a coordinate transformation similar to the one in Eq. (116). The modal coordinate nonlinear equation assumes the transformed structure below

$$\begin{aligned} \tilde{M} \ddot{\underline{\eta}} + \tilde{K} \underline{\eta} + \Phi^T \{NLT(\Phi \eta)\} &= \Phi^T Q \\ \text{where } \tilde{M} &= \Phi^T M \Phi = I \\ \text{and } \tilde{K} &= \Phi^T K \Phi = \text{diag}(\omega_1^2, \omega_2^2, \dots, \omega_n^2) \end{aligned} \quad (127)$$

The first order form of Eq. (127) is integrated in time using a subset of the modal coordinates. The solution is then transformed back to spatial coordinates. The cost function used to rank the modal coordinates is the contribution of each modal coordinate to the energy of the linear system. The nonlinear model is used to solve for the dynamic response but the linear form of the energy is used for ranking the modal contributions. The kinetic and potential energy in modal coordinates is

$$E = \int_{t_1}^{t_2} (\dot{\underline{\eta}}^T \tilde{M} \dot{\underline{\eta}} + \underline{\eta}^T \tilde{K} \underline{\eta}) dt \quad (128)$$

The transverse modes dominate the kinetic energy contributions and the axial modes dominate the potential energy contributions. The first mode #1 with a frequency of 2.4288 rad/s is the largest contributor to the kinetic energy and mode #15 with a frequency of 4732.06 rad/s is the largest contributor to the potential energy of the model. Using Skelton's modal cost idea, fifteen modes are chosen to be the subset of coordinates which represent most of the dynamic motion. These modes are listed below

$$\Phi_{Tr} = [\phi_1, \phi_2, \phi_3, \phi_4, \phi_5, \phi_{10}, \phi_{15}, \phi_{19}, \phi_{20}, \phi_{21}, \phi_{22}, \phi_{23}, \phi_{24}, \phi_{25}, \phi_{28}] \quad (129)$$

The last mode included in the subset has a frequency of 115665.15 rad/s and period of .000054 sec. Truncating above this mode would only allow the integration time step to be doubled from .00001 sec to .00002 sec. The solution to a free vibration case is compared for the truncated model and the full order model for a time interval of .65 sec. The initial deformation shape is due to the transverse tip force of 8 N. A comparison of the beam deformation shapes for the truncated model and the full order model is shown in Figure 18. The shapes at two times are compared.

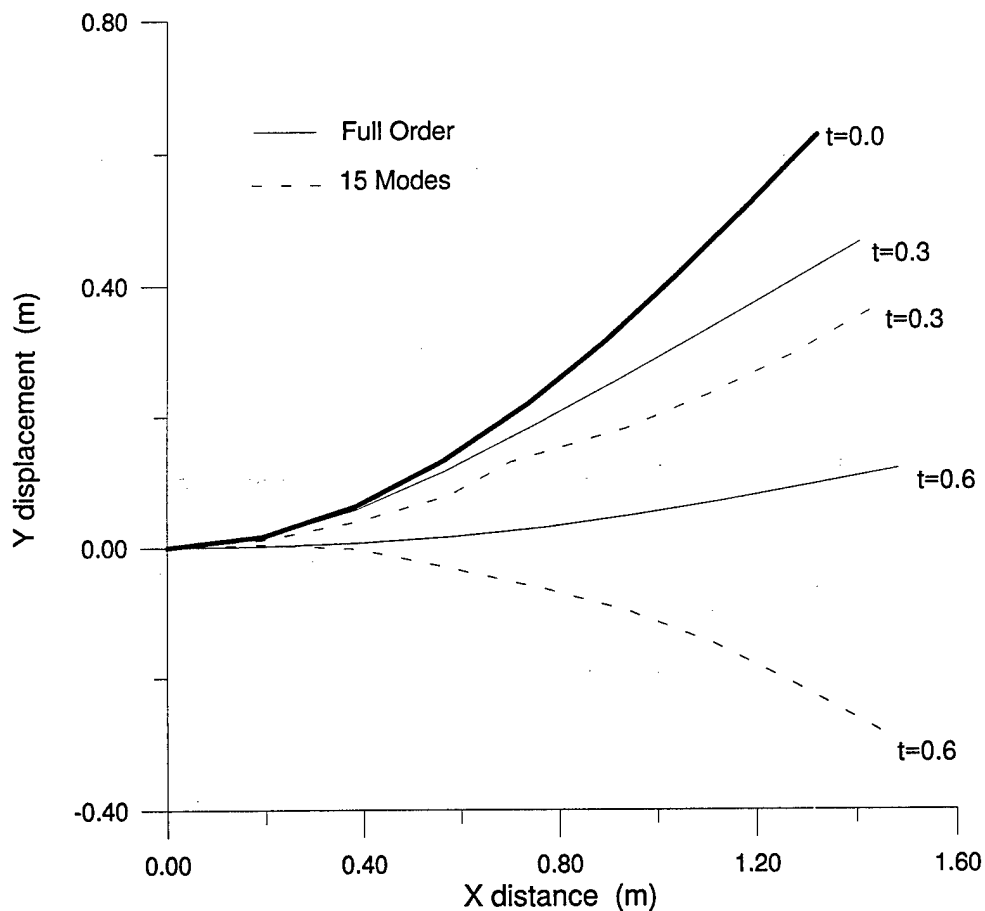


Figure 18. Beam shapes for truncated and full order models

The displacements for the truncated model are found to be significantly different than the displacements of the full order model. In comparing the output, the differences between the models are contained in the nonlinear vector term  $NLT(\phi\eta)$ . The small differences in the modal coordinates are summed many times and multiplied by large constants,  $EA_1$ ,  $EA_2$ . The modal truncation is tested for neglecting only one mode, #8, which is the lowest contributor for the transverse deflection. The displacements obtained after one quarter cycle agree to within 6 digits to the displacements of the full order model. The displacements at node 2 and node 3 are slightly different (agree to 4 digits) than the full order model. Neglecting mode #8 appears to have a very small affect on the motion of the beam system and appears to affect the middle of beam 1. Other transverse deflection modes which have a small cost contribution can be neglected, however this does not allow a larger time step since these frequencies are much smaller than the axial mode frequencies. Modal truncation is tested for neglecting the three highest axial modes, #31, #32, #33. The highest frequency remaining in the model is 142621.9 rad/s and the time step is increased to .000015. The displacements obtained after one quarter cycle agree only to within 1 digit to the displacements of the full order model. The increase in the time step does not justify the truncation of the highest modes since the results are not in very good agreement, especially since our analysis indicates the full order model is needed as a reference to confidently truncate any modes. Thus, unfortunately, modal truncation does not appear attractive as a means to enhance the solution efficiency or accuracy for this particular nonlinear finite element model.

#### *Rotational Inertia*

The contributions to the kinetic energy of the rotational motion of the beams and the tip and elbow masses are analyzed to see if the rotational inertia should be included in the model. The rotational kinetic energy for a body is

$$T = \frac{1}{2} \dot{\Psi}^T [I] \dot{\Psi} \quad (130)$$

where  $\dot{\Psi} = [(1+u')\dot{w}' - w'\dot{u}']$  and  $I$  is the mass moment of inertia about the center of mass. The moment of inertia about the  $z$  axis for a beam of differential cross section  $dx$  and thickness  $a$  is

$$I_z = \frac{1}{12} \rho a^2 dx \quad (131)$$

For the PACE system, the thickness of each beam is .00315976 m. The moment of inertia for the differential cross section is computed to be 4.426E-07 kg-m. This value is small and the angular velocity is typically 1.85 s<sup>-1</sup>. Therefore the rotational inertia for the beams are not included. The inertias for the elbow and tip masses are 122.98E-04 kg-m<sup>2</sup> and 15.244E-04 kg-m<sup>2</sup> respectively. The angular velocity is substituted into Eq. (130) and the first variation is taken. The results are added to the nonlinear finite element equations for  $\delta u'$  and  $\delta w'$  at the elbow and tip node locations. The  $\delta u'$  and  $\delta w'$  equations can be written in matrix form

$$I \begin{bmatrix} (1+u')^2 & -w'(1+u') \\ -w'(1+u') & w'^2 \end{bmatrix} \begin{Bmatrix} \dot{w}' \\ \dot{u}' \end{Bmatrix} + I \begin{Bmatrix} 2\dot{u}'(\dot{w}'(1+u') - w'\dot{u}') \\ 2\dot{w}'(\dot{w}'(1+u') - w'\dot{u}') \end{Bmatrix} \quad (132)$$

The first nonlinear matrix part of the above equation is added to the mass matrix and the second nonlinear vector is added to the  $NLT$  vector. The free vibration of the finite element model is integrated over half a cycle using the initial condition due to a tip transverse force of 8 N. The velocities of the elbow and tip angles range from -.23 s<sup>-1</sup> to -1.85 s<sup>-1</sup> over half the cycle. The rotational kinetic energy is small due to these small velocities and the small moments of inertia. The tip transverse deflections are compared in Figure 19 for the model including rotary inertia and without it.

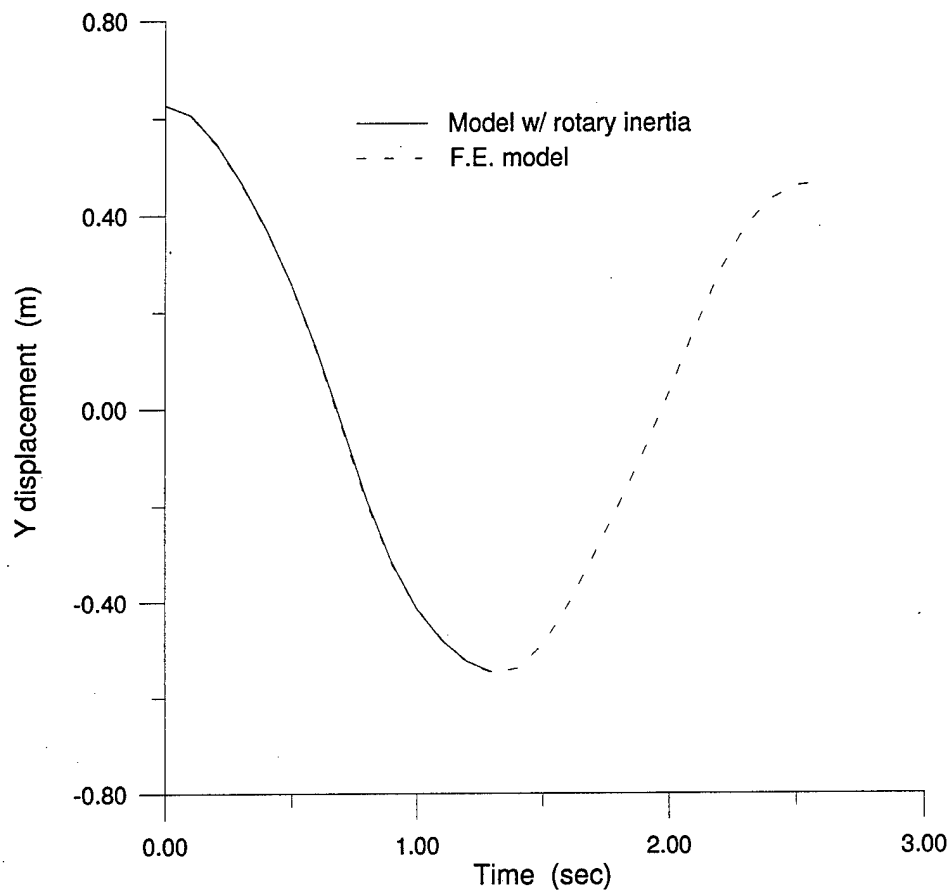


**Figure 19. Rotational inertia effects**

The deflections of the beam model including rotational inertia effects follows almost exactly the deformation history of the beam model without these effects. The rotational motion caused by a free vibration of the PACE two beam system does not significantly affect the results. Furthermore including the rotational kinetic energy complicates the model since it results in a nonconstant and nonlinear mass matrix. Therefore the rotational dynamics of the tip and elbow masses are not included in the model.

#### 4.1.5 Simulations

A free vibration analysis is presented for the nonlinear finite element model of the PACE two beam system. This is the base solution for the parameter recovery method. The

deformation shape associated with a tip force of 8 N is used as the initial condition. Each beam is divided into four elements, giving a total of eight elements. The equation of motion, Eq. (106), for the system is integrated in time using a Runge Kutta scheme. The system is studied with the tip mass and elbow mass values listed in Table 1 and includes sliding friction effects. The values for the coefficient of kinetic friction between metal and metal surfaces range from 0.11 to 0.45.<sup>18</sup> For the PACE two beam system, the supporting surface is an air bearing table and the values of the friction coefficients will be significantly less. A friction coefficient of  $\mu_e=0.01$  is used for the elbow mass and  $\mu_t=0.02$  is used for the tip mass. Figure 20 and Figure 21 show the time history of the  $w_{tip}$  and  $u_{tip}$  deflections over a cycle.

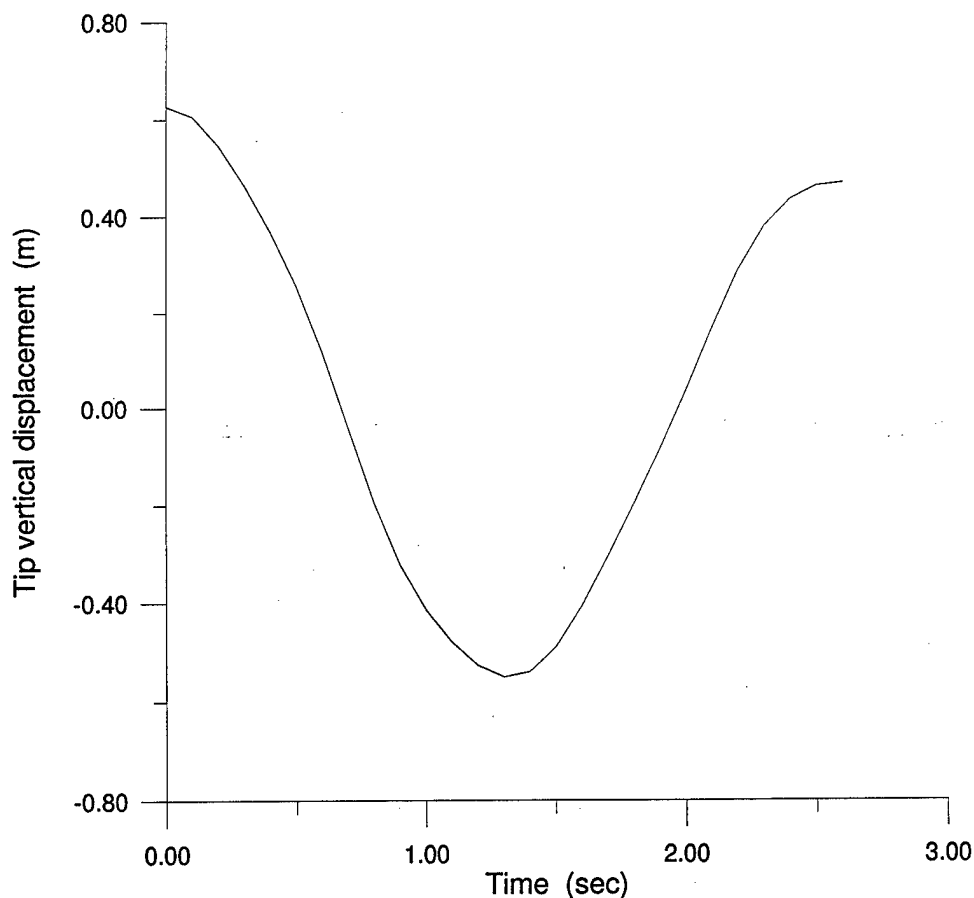


**Figure 20. Tip transverse deflection over a period**

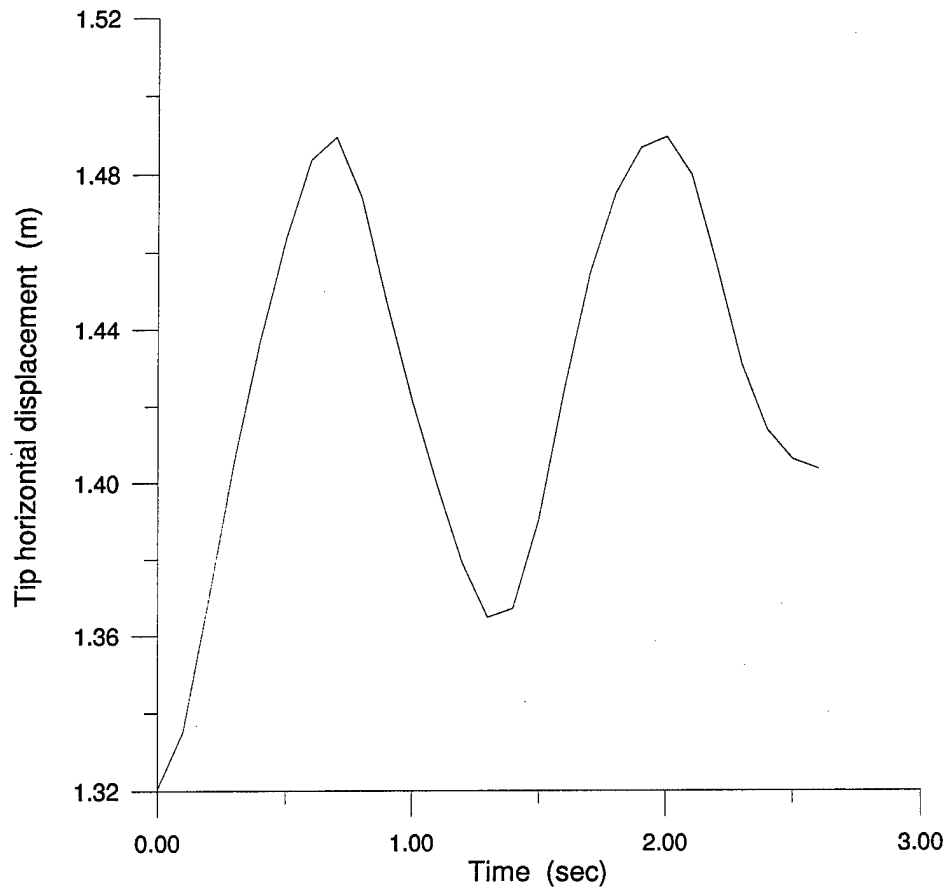


**Figure 21. Tip longitudinal deflection over a period**

The period for the nonlinear model of 2.6 seconds is shown in the transverse tip deflections and corresponds to the lowest period for the similar linear problem. The damping shown in the tip deflection is due to the work done by friction. Figure 22 shows the whole deformation shape of the two beam system for one quarter of a cycle.



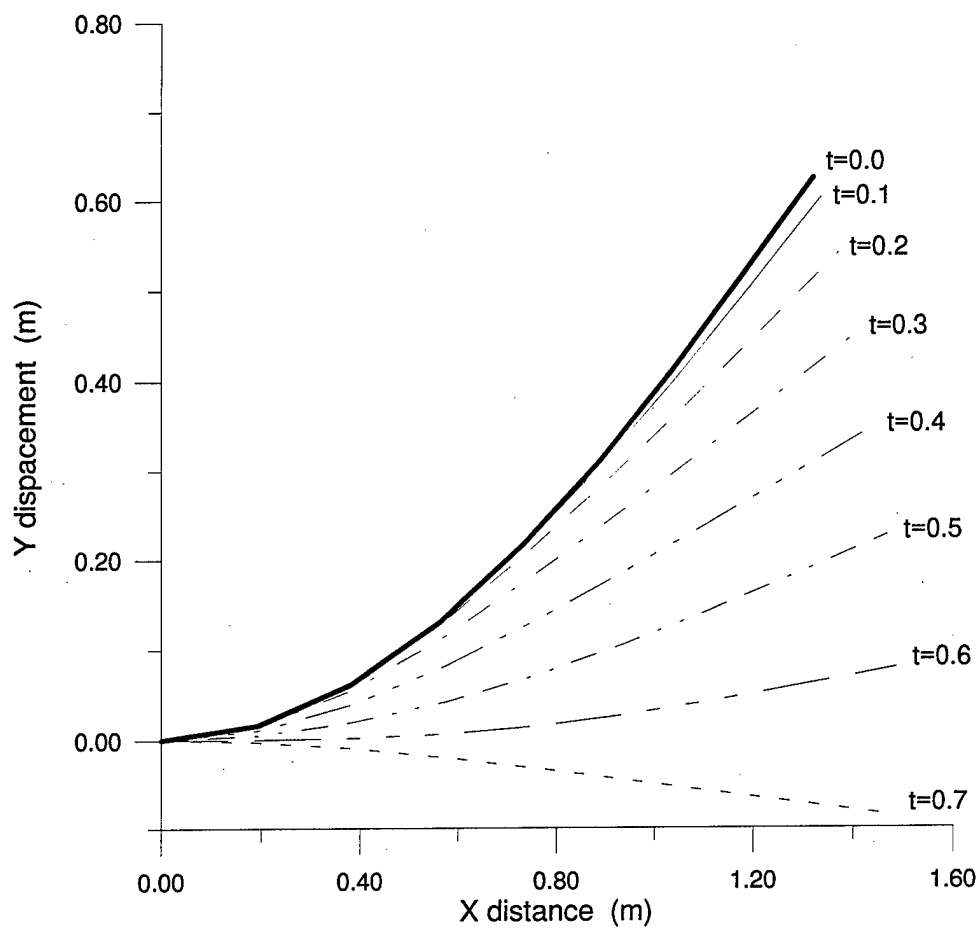


**Figure 22. Beam profiles for 1/4 period**

An energy balance is done at each time step to verify the change in the system's potential and kinetic energy equals the work done by the friction forces. The initial energy of the system is 2.25257 N·m. Table 13 summarizes the energy check.

Time	$\Delta$ Energy	Work
0.1	-.00821430	-.00821428
0.5	-.17588910	-.17588908
1.0	-.44118282	-.44118282
1.5	-.54355840	-.54355839
2.0	-.76443096	-.76443094
2.6	-.94819115	-.94819112

The change in energy differs negligibly from the work done by the friction forces and verifies the programming of the friction forces is consistent in the model.

The finite element model is also integrated over time without the friction forces to ensure the energy of the system is constant. The potential energy is largest at the highest and lowest transverse deflection shapes while the kinetic energy is largest when the beam passes through the axis where the transverse deflection is zero. The value of the total energy is constant and agrees to within 9 digits over time to the initial value of 2.25257295 N·m. These tests verify the nonlinear finite element model is correct from a conservation of energy perspective and provides a basis for confidence that the formulation is valid and correctly programmed.

#### **4.2 Free Vibration Parameter Estimation**

The beam parameters affecting the free response characteristics of the system are recovered using a set of measurements. There are several parameters that may not be well known such as the friction coefficients or the mass per unit length of each beam.

#### 4.2.1 Least Squares Estimation

The least squares analysis developed for the inverse static analysis is used to recover the best fit parameters for the free response motion. The free vibration parameters are represented by a vector  $p$ . Measurements at different time intervals are represented by the vector  $\tilde{Y}_{meas}$ . The least square differential correction formula for updating the parameters is repeated below

$$p_{n+1} = p_n + (\Omega^T \Omega)^{-1} \Omega^T (\tilde{Y}_{meas} - \hat{Y}_{model}(p_n)) \quad \text{where } \Omega = \left. \frac{\partial \hat{Y}}{\partial p} \right|_n \quad (133)$$

The sensitivity matrix will obviously change since the nonlinear model and the parameters are different for the free response solution. The sensitivity matrix is developed using the parametric differentiation technique<sup>13</sup>.

The first order form of the nonlinear finite element model given in Eq. (107) is

$$\dot{v} = f(t, v, p) \quad (134)$$

The time derivative of the sensitivity matrix becomes

$$\frac{d}{dt} [\Omega(t, t_0)] = \frac{d}{dt} \left[ \frac{\partial v(t)}{\partial p} \right] = \frac{\partial f}{\partial p} + \frac{\partial f}{\partial v(t)} \frac{\partial v(t)}{\partial p} \quad (135)$$

This matrix has both an explicit and implicit dependence on the parameters  $p$  since the displacement and velocity variables  $v$  depend on  $p$ . This differential equation is integrated simultaneously with the solution to Eq. (107). The entire sensitivity matrix is integrated but only a portion is used in Eq. (133) for the variables in  $v$  that correspond to the variables that are measured.

The derivatives in Eq. (135) depend on the parameters chosen for recovery and are described in the following section for friction coefficients and mass density parameters. For the case where the nonconservative force vector  $Q$  is only dependent on friction forces, Eq. (107) becomes

$$f = \dot{v} = \begin{Bmatrix} \dot{v}_1 \\ \dot{v}_2 \end{Bmatrix} = \left\{ [M]^{-1} \left[ \left[ I - C^T (CM^{-1}C^T)^{-1} CM^{-1} \right] \{ Q - NLT(\underline{q}) \} \right] \right\} \quad (136)$$

The implicit derivative matrix  $\partial f / \partial v$  can be decomposed into four sub-matrices. The first (1,1) sub-matrix is a zero matrix and the second (1,2) sub-matrix is the identity matrix. The fourth (2,2) sub-matrix is also a zero matrix since there is no velocity dependence in the  $Q$  or  $NLT$  vectors. The third (2,1) sub-matrix consists of the derivative of the  $NLT$  vector with respect to each variable (the Jacobian matrix discussed earlier) and multiplied by  $[M]^{-1}$  and the factor  $CMULTI$  where  $CMULTI = \{ C^T (CM^{-1}C^T)^{-1} CM^{-1} - I \}$ . Calculation of the Jacobian matrix is a time consuming operation due to all the nonlinear summation terms in the model. For the parameter recovery program, the Jacobian must be calculated at each time step and the whole solution repeated each time the parameters are updated. This translates into a large amount of computer time depending on how long a time period is covered by the measurements. The implicit derivative matrix is summarized below

$$\frac{\partial f}{\partial v} = \left[ \begin{array}{c|c} 0 & I \\ \hline [M]^{-1} [CMULTI] \left[ \frac{\partial NLT}{\partial v} \right] & 0 \end{array} \right] \quad (137)$$

The explicit derivative matrix  $\partial f / \partial p$  is different, depending on the type of parameter involved in the differentiation. For the friction coefficient parameters the explicit derivative matrix is

$$\frac{\partial f}{\partial \mu} = \left\{ [M]^{-1} \left[ \begin{array}{c} \{0\} \\ [CMULTI] \left\{ -\frac{\partial Q}{\partial \mu} \right\} \end{array} \right] \right\} \quad (138)$$

The derivative  $\partial Q/\partial \mu$  for friction forces is a vector of zeros with the value  $-N \text{sign}(\dot{q})$  at the appropriate locations. The explicit dependence of the model  $f$  on the mass density parameters is in the mass matrix. The following identity is needed in the derivative

$$\frac{\partial}{\partial \rho} (M^{-1}) = -M^{-1} \frac{\partial M}{\partial \rho} M^{-1} \quad (139)$$

After several algebraic steps the explicit derivative matrix for the mass density parameters becomes

$$\frac{\partial f}{\partial \rho} = \left\{ [M]^{-1} [CMULTI] \left[ \begin{array}{c} \{0\} \\ \frac{\partial M}{\partial \rho} [CMULTI] \{NLT(q) - Q\} \end{array} \right] \right\} \quad (140)$$

All these implicit and explicit derivatives are combined and inserted into Eq. (135).

A set of parameters is used in the simultaneous numerical solutions of Eq. (107) and Eq. (135). The parameters are then updated using Eq. (133). The numerical solution and updating process is repeated until the changes in the parameters are small<sup>14</sup>.

#### *Measurement Errors*

Physical measurements of the tip locations over time will have some uncertainty or error variance associated with them. These errors are included in the parameter updating process for the free response motion using the weighted least squares approach developed in the inverse static analysis. The weight matrix will consist of the inverse error variance

associated with each measurement. The formula for updating the parameters is repeated below

$$p_{n+1} = p_n + (\Omega^T W \Omega)^{-1} \Omega^T W (\tilde{Y}_{meas} - \hat{Y}_{model}(p_n)) \quad (141)$$

The sensitivity matrix for the nonlinear finite element model variables is developed in the preceding section. The numerical solutions of the nonlinear finite element model and the derivative matrices are repeated with the updated parameters until the changes in the parameters are small.

#### *A priori Estimates*

Some of the parameters may be known within a certain confidence level and this can be reflected in *a priori* estimates and errors of these estimates. The uncertainties associated with these *a priori* estimates are used to limit the changes to the parameters so unreasonable values don't result. These uncertainties are incorporated using a covariance matrix. The *a priori* estimates can be treated as an additional measurement equation.

$$\{p_{apriori} - p_n\} = [I] \{p_{n+1} - p_n\} + e_{apriori} \quad (142)$$

The equation for the *a priori* error is combined with the error expression for the measurements in Eq. (141) yielding

$$e_{tot} = \begin{Bmatrix} \tilde{Y}_{meas} - \hat{Y}_{model}(p_n) \\ p_{apriori} - p_n \end{Bmatrix} - \begin{bmatrix} \Omega \\ I \end{bmatrix} \{p_{n+1} - p_n\} \quad (143)$$

The variance matrix for the *a priori* estimates is assumed here to have the diagonal (uncorrelated) structure.

$$\Gamma = \begin{bmatrix} \frac{1}{\sigma_{est\ p1}^2} & 0 & \dots & 0 \\ 0 & \frac{1}{\sigma_{est\ p2}^2} & \dots & 0 \\ \vdots & \vdots & \ddots & \vdots \\ 0 & 0 & \dots & \frac{1}{\sigma_{est\ p\#}^2} \end{bmatrix} \quad (144)$$

where  $\sigma_{est\ p1}$  is the estimated standard deviation of the *a priori* estimate of parameter 1, etc. The overall weight matrix is made by combining the variance matrix  $W$  of the measurements and the variance matrix  $\Gamma$  of the *a priori* estimates:  $\Lambda = \begin{bmatrix} W & 0 \\ 0 & \Gamma \end{bmatrix}$

The least squares function of the error is minimized giving the update equation for the parameter vector  $p$

$$p_{n+1} = p_n + (A^T \Lambda A)^{-1} A^T \Lambda \begin{Bmatrix} \tilde{Y}_{meas} - \hat{Y}_{model}(p_n) \\ p_{apriori} - p_n \end{Bmatrix} \quad \text{where } A = \begin{bmatrix} \Omega \\ I \end{bmatrix} \quad (145)$$

The covariance matrix for the estimated parameters  $p$  including *a priori* information is  $E_{fr} = (A^T \Lambda A)^{-1}$ .

A set of parameters is used in the numerical solutions of Eq. (107) and Eq. (135). The parameters are updated using Eq. (145) and the numerical solution is repeated until the parameters are converged. The variance of each parameter is taken from the diagonal of matrix  $E_{fr}$  and is used to decide how well the parameter is determined.

#### *Parameter Uncertainties*

The estimated parameters recovered in the static analysis can be brought forward along with their associated uncertainties and combined with the recovery of parameters

affecting the free vibration response. This will allow adjustments to be made to the statically determined parameters if they are not determined well. If the previously determined parameters are well converged, this new recovery program will maintain these values while allowing other parameters to be changed. The parameters and uncertainties recovered from the free vibration analysis are optimistic since the values of the static parameters were assumed to be known. The free vibration parameters can be further adjusted using this combined analysis. This will be achieved by using an approach similar to the one taken in the parameter recovery method with *a priori* estimates. The parameters recovered by the static deformation analysis will be represented by the vector  $p_s = (EI_1, EI_2)$ . The parameters recovered by the free vibration analysis will be represented by the vector  $p_{fr} = (\mu_e, \mu_t, \rho_1, \rho_2)$ . The statically determined parameters can be treated as an additional measurement  $\tilde{p}_s$  and an additional error equation is developed.

$$\{\tilde{p}_s - \hat{p}_s\} = [I]\{\Delta p_s\} + e_s \quad (146)$$

This equation is combined with the error expression for the free vibration measurements (similar to Eq. (38)) yielding

$$e_{tot} = \begin{Bmatrix} \tilde{Y}_{meas} - \hat{Y}_{model}(p) \\ \tilde{p}_s - \hat{p}_s \end{Bmatrix} - \begin{bmatrix} \Omega_{fr} & \Omega_s \\ 0 & I \end{bmatrix} \begin{Bmatrix} \Delta p_{fr} \\ \Delta p_s \end{Bmatrix} \quad (147)$$

The sensitivity matrix,  $\Omega_s$  which is the derivatives of the measurement variables with respect to the static parameters must be computed for the nonlinear finite element model and included in the solution process.



An overall weight matrix is made by combining the variance matrix  $W$  of the free vibration measurements and the covariance matrix  $E_s$  of the static parameters:  $\Lambda = \begin{bmatrix} W & 0 \\ 0 & E_s \end{bmatrix}$

The weighted least squares minimization yields an update for the parameters

$$\begin{Bmatrix} \Delta p_{fr} \\ \Delta p_s \end{Bmatrix} = (A^T \Lambda A)^{-1} A^T \Lambda \begin{Bmatrix} \tilde{Y}_{meas} - \hat{Y}_{model}(p) \\ \tilde{p}_s - \hat{p}_s \end{Bmatrix} \quad \text{where } A = \begin{bmatrix} \Omega_{fr} & \Omega_s \\ 0 & I \end{bmatrix} \quad (148)$$

This will allow further updates to the static and free vibration parameters to account for all the parameter uncertainties in a free vibration experiment.

#### 4.2.2 Results - Free Vibration Parameters

The set of measurements used to recover beam properties are simulated using the numerical solution of the nonlinear finite element model described in Eq. (107). The free vibration response is computed for a set of 'true' parameters. The response is due to an initial deformation shape caused by a tip transverse force of 8 N. To illustrate robustness, we consider a relatively short time interval transient solution. Of course longer time intervals would yield greater precision in the estimated parameters. The tip deflections over one period of the dominant linear mode are shown in Figure 20 and in Figure 21. The tip  $w_t$  and  $u_t$  locations are chosen as the measured variables at selected time intervals over the period of the beam deflection.

A subset of the dynamic parameters is chosen to illustrate the recovery method. This subset consists of the friction coefficients of the elbow and tip masses and the mass densities of the beams  $p_{fr} = (\mu_e, \mu_t, \rho_1, \rho_2)$ . The 'true' mass densities are listed in Table 1 and the 'true' friction coefficients are  $\mu_e=0.01$  and  $\mu_t=0.02$ . The calculations of the tip location  $u_t$  and  $w_t$  at five selected time intervals are input to the parameter recovery

program giving a total of 10 measurements. The sensitivity matrix  $\Omega$  is a  $4 \times 10$  matrix as follows

$$\Omega = \begin{bmatrix} \frac{\partial w_9(t_1)}{\partial \mu_e} & \frac{\partial w_9(t_1)}{\partial \mu_t} & \frac{\partial w_9(t_1)}{\partial \rho_1} & \frac{\partial w_9(t_1)}{\partial \rho_2} \\ \frac{\partial u_9(t_1)}{\partial \mu_e} & \frac{\partial u_9(t_1)}{\partial \mu_t} & \frac{\partial u_9(t_1)}{\partial \rho_1} & \frac{\partial u_9(t_1)}{\partial \rho_2} \\ \frac{\partial w_9(t_2)}{\partial \mu_e} & \frac{\partial w_9(t_2)}{\partial \mu_t} & \frac{\partial w_9(t_2)}{\partial \rho_1} & \frac{\partial w_9(t_2)}{\partial \rho_2} \\ \frac{\partial u_9(t_2)}{\partial \mu_e} & \frac{\partial u_9(t_2)}{\partial \mu_t} & \frac{\partial u_9(t_2)}{\partial \rho_1} & \frac{\partial u_9(t_2)}{\partial \rho_2} \\ \frac{\partial w_9(t_5)}{\partial \mu_e} & \frac{\partial w_9(t_5)}{\partial \mu_t} & \frac{\partial w_9(t_5)}{\partial \rho_1} & \frac{\partial w_9(t_5)}{\partial \rho_2} \\ \frac{\partial u_9(t_5)}{\partial \mu_e} & \frac{\partial u_9(t_5)}{\partial \mu_t} & \frac{\partial u_9(t_5)}{\partial \rho_1} & \frac{\partial u_9(t_5)}{\partial \rho_2} \end{bmatrix}$$

Estimates for the mass densities of the beams and the friction coefficient are used to start the program. The numerical solutions of Eq. (107) and Eq. (135) are solved for the time intervals specified and the parameters are updated using Eq. (133). This is repeated until the changes in the parameters are small. Table 14 summarizes the true and recovered values of the parameters assuming there are no errors in the measurements.

Table 14. Parameter recovery for perfect measurements				
	$\mu_{\text{elbow}}$	$\mu_{\text{tip}}$	$\rho_1$	$\rho_2$
True values	0.010	0.02	.5320	.5300
Starting estimate	0.015	0.01	.5603	.5437
Values after 1 iter.	0.010	0.02	.5297	.5300
Values after 3 iter.	0.010	0.02	.5320	.5300

The program rapidly converges to the true parameter values. Other numerical experiments indicate a large domain of attraction, with very reliable and practical convergence. The

parameters associated with the second beam system are recovered more rapidly than those in the first beam system, due to the larger kinetic energy effects at the tip of the system.

#### *Measurement Errors*

The simulated measurements from the free response using the 'true' parameters have errors introduced using a Gaussian random number generator. For each measurement, an error is created from a random number with zero mean and an associated standard deviation  $\sigma$ . The errors are added to the 'true' measurements which are then used to determine the best fit parameters in the model.

The tip locations  $w_t$  and  $u_t$  at nine selected time intervals that span one quarter of the deformation cycle are used for a total of 18 measurements. The standard deviations used in the errors of these measurements range from 0.0015 to 0.0006 for the  $w$  and  $u$  coordinates. The larger the standard deviation value the less weight is given to that measurement in the program and the less it affects the recovered parameters. Table 15 summarizes the results of the recovered values of the parameters.

<b>Table 15. Parameter recovery over 1/4 cycle with measurement errors</b>				
	$\mu_{\text{elbow}}$	$\mu_{\text{tip}}$	$\rho_1$	$\rho_2$
True values	0.0100	0.0200	0.5320	0.5300
Initial estimate	0.0150	0.0100	0.5603	0.5437
Recovered values	0.0109	0.0232	0.1289	0.4993
Recovered $\sigma$	0.0039	0.0115	0.4099	0.1634

The recovered values of the friction coefficients are seen to be within 16% of the true values and within one estimated standard deviation of the parameters. The mass densities are significantly different than the true values and have correspondingly larger standard deviations indicating they are not well determined by these measurements. These relatively

larger errors indicate poor observability and suggest a longer time interval experiment, or a new experiment in which these parameters play a more important role. A longer time interval of measurements is used to better estimate the mass densities. Measurements of the  $w_t$  and  $u_t$  variables for eighteen time intervals over one half of the deformation cycle are used giving a total of 36 measurements. Again the standard deviations of the measurements range from .0015 to .0006. Table 16 summarizes the parameters and the associated errors recovered for this case.

	$\mu_{\text{elbow}}$	$\mu_{\text{tip}}$	$\rho_1$	$\rho_2$
True values	0.0100	0.0200	0.5320	0.5300
Initial estimate	0.0150	0.0100	0.5603	0.5437
Recovered values	0.0084	0.0220	0.4677	0.5360
Recovered $\sigma$	0.0020	0.0026	0.1199	0.0843

The values for the friction coefficients estimated are much closer to the true values than the coefficients recovered for the quarter cycle measurements. The small error variance of these parameters indicate they are fairly well determined. The recovered value of the first beam's mass density is worse than the initial estimate and this estimated value is outside the commonly accepted density range of standard aluminum beams<sup>19</sup>. The estimated standard deviation of this parameter is consistently large compared to the value of the parameter, so at least the estimation process "knows it doesn't know". This indicates the recovery of the beam 1 density parameter cannot be trusted. The recovered value of the second beam's mass density is close to the true value and is an improvement over the estimated value. However, it still has an associated standard deviation that is large which would indicate the value of the parameter is not well determined suggesting that this convergence is fortuitous. Therefore, the densities of the beams are weakly observable

and there is little confidence in these recovered parameter values. On the other hand, the other parameters can be estimated from a very short transient response.

The mass densities of the beams are clearly difficult to recover in the presence of measurement errors. This is because they do not have a large effect on the free response behavior of the system in this particular experiment. Table 17 lists the tip locations solved at various times using the recovered parameter values listed in Table 16. The measured tip locations input to the model and the tip locations obtained using the true parameters are included in this table for comparison.

Time	$w_t$ - measured	$w_t$ - true parameters	$w_t$ - rec. parameters
0.1	.604670	.605715	.605819
0.5	.256023	.255165	.255321
1.0	-.413409	-.413560	-.413387
1.3	-.550037	-.550117	-.550549

The tip deflections using the recovered parameter values are closer to the deflections predicted by the true parameter values than the measured values. This is due to the effect of the number of measurements on the relationship between the variance of the parameters and the variance of the measurements. This improvement is seen even with the unlikely values of the beam mass densities used as part of the parameters. Again, the apparent paradox simply reflects the truth that the beam densities have such a small effect on the free response of the system over this relatively short transient motion. If there were no external forces, we can easily show that the mass densities would not be uniquely determined, so the observability is also linked to the smallness of the friction force.

### *A priori Estimates*

The starting estimates of the parameters can be known within a certain tolerance and this information can be used to limit the changes in the parameters. As was pointed out in the last section, the value of the first beam mass density recovered is below the known density range for aluminum beams having that shape. *A priori* information can be used to limit the estimates of low observability parameters to be consistent with an *a priori* estimate's uncertainty.

The tip locations for eleven time intervals over one quarter cycle of the period are input for a total of 22 measurements to the parameter recovery program. The standard deviations used for the measurements range from 0.0015 to 0.0006. *A priori* estimates of the parameters are used as the starting values in the program. The *a priori* variance values of the beam mass densities and friction parameters will have negligible impact on observable parameters, but will serve to hold poorly estimated parameters to the neighborhood of the *a priori* estimates (consistent with *a priori* estimates). The converged covariance matrix will correctly reflect the total information content of both the *a priori* information and the measurements.

The numerical solution of Eq. (107) and Eq. (135) are computed to the final time period and Eq. (145) is used to update the parameters. This recovery process is repeated until the change in the parameter values is small. Table 18 summarizes the parameters recovered and the converged parameters' standard deviations.

	$\mu_{\text{elbow}}$	$\mu_{\text{tip}}$	$\rho_1$	$\rho_2$
True values	0.0100	0.0200	0.5320	0.5300
<i>a priori</i> estimate	0.0150	0.0100	0.5603	0.5437
<i>a priori</i> $\sigma$	0.0075	0.0150	0.0532	0.0530
Recovered values	0.0081	0.0203	0.5486	0.5557
Recovered $\sigma$	0.0019	0.0042	0.0526	0.0481

Including the *a priori* variance matrix stabilized the poorly observed densities and indirectly the tip mass friction coefficient. The recovered value of  $\mu_{\text{tip}}$  is closer to the true value than the recovered value of  $\mu_{\text{tip}}$  with only the effect of measurement errors included. The value recovered for the elbow mass friction coefficient was not significantly affected. The *a priori* variance values did limit the change in the beam mass densities and kept the recovered parameters closer to the *a priori* as well as the true values. The standard deviations of the recovered mass densities are smaller compared to those obtained using only measurement errors but they remain comparable to their *a priori* values. This indicates a large range of densities can be obtained and still be consistent with the measured motion.

Since the mass densities are difficult parameters to estimate, they are removed from the parameter estimation and only the friction coefficients are estimated using the *a priori* covariance matrix. The standard deviations of the friction coefficients allows large changes of the *a priori* values. Measurements of the tip  $u$  and  $w$  locations are taken for six time intervals and similar measurement errors are used as listed in the last section. Table 19 lists the recovered friction parameters and their associated errors.

	$\mu_{\text{elbow}}$	$\mu_{\text{tip}}$
True values	0.0100	0.0200
<i>a priori</i> estimate	0.0150	0.0100
<i>a priori</i> $\sigma$	0.0080	0.0120
Recovered values	0.0093	0.0202
Recovered $\sigma$	0.0042	0.0036

The values recovered for the friction coefficients using the *a priori* variance matrix are close to the true values and well within one standard deviation of the true values. The *a priori* standard deviations of the friction coefficients are doubled to allow greater changes to the parameter values and the parameter recovery program is repeated. These results are shown in Table 20.

	$\mu_{\text{elbow}}$	$\mu_{\text{tip}}$
True values	0.0100	0.0200
<i>a priori</i> estimate	0.0150	0.0100
<i>a priori</i> $\sigma$	0.0160	0.0240
Recovered values	0.0067	0.0224
Recovered $\sigma$	0.0049	0.0041

The recovered friction coefficient values are not as close to the true values as those recovered for the more limiting variance matrix. They are within one standard deviation of the true values. A more reasonable process would be to repeat this experiment with a distribution of estimates with the *a priori* statistics. This would allow one to confirm the



truth that the estimation process is statistically consistent. However, any given experiment may look contrived because it is merely a sample from a distribution of possibilities.

The recovered friction coefficients are used in the program to determine the free response deformation shapes of the beam system. The tip transverse deflections are compared to the deflections obtained using the true coefficients and compared to the measured data used for input to the parameter recovery program. This comparison is summarized in Table 21.

<b>Table 21. Effects of <i>a priori</i> determined friction parameters</b>			
Time	$w_t$ - measured	$w_t$ - true parameters	$w_t$ - rec. parameters
0.1	.606013	.605715	.605723
0.2	.546752	.546841	.546847
0.3	.463057	.464102	.464035
0.4	.368208	.367896	.367637

The beam deformation shapes using the recovered parameters agree well with the deformation shapes using the true values. There is 3 to 4 digit accuracy between the tip values. The friction coefficients are fairly well-determined parameters and we have the means to accommodate consistently any *a priori* information available.

## CHAPTER V

### NONLINEAR FORCED VIBRATION ANALYSIS

#### 5.1 Development

Including motor effects in the modeling of the PACE two beam system is the last step in the sequential system identification process. Additions to the nonlinear finite element model are made to reflect the dynamics of a motor attached to the structure.

##### 5.1.1 Motor Modeling

The motor operation and characteristics needed for this computer simulation are taken from hardware commonly used in the Dynamics and Controls Laboratory of the Aerospace Engineering Department at Texas A&M University<sup>2</sup>. A reaction wheel motor is placed on the tip of the structure to suppress end effector vibration. A torque is applied on the tip of the structure by accelerating the reaction wheel with a DC motor. The torque of the motor is a function of the voltage sent to the motor by the power amplifier<sup>21</sup>. Since the power amplifier can be operated in current or voltage mode, we assume the power amplifier is operated in the current mode which avoids including the dynamics of the motor in the simulation. This is because our motor has a near linear torque/current relationship. The power amplifier uses an internal control law to adjust the voltage supplied to the motor to follow the desired current. The time constant of the power amplifier is sufficiently short ( $\cong 10^{-3}$  s) that the response time is neglected in this study. A Maxon DC motor outfitted with a reaction wheel is sent a current which is used to apply a commanded control torque.

$$T = K_t i \quad (149)$$

where  $K_t$  is the torque constant of the motor and equals 0.03891 N·m/amp. The linear torque/current relationship is accurate to less than 1% over a bandwidth from 0 to 30 Hz

assuming saturation conditions are not encountered. A control law to suppress end vibration is chosen and is a linear feedback damper of the form

$$T = -g \dot{\Psi}_{tip} \quad (150)$$

where  $g$  is the gain and  $\dot{\Psi}_{tip}$  is the angular velocity of the beam tip.

For the nonlinear finite element model, the torque is included in the nonconservative work term

$$\delta W_{nc} = T \delta \Psi_{tip} \quad (151)$$

Using the coordinate system established in Figure 12, the variation of the tip angle is

$$\delta \Psi_{tip} = \left[ (1 + u'_{tip}) \delta w'_{tip} - w'_{tip} \delta u'_{tip} \right] \quad (152)$$

and the velocity is

$$\dot{\Psi}_{tip} = \left[ (1 + u'_{tip}) \dot{w}'_{tip} - w'_{tip} \dot{u}'_{tip} \right] \quad (153)$$

Combining Eqs. (150) - (153) gives the following expression for the nonconservative work

$$\begin{aligned} \delta W_{nc} = & -g \left[ (1 + u'_{tip})^2 \dot{w}'_{tip} - (1 + u'_{tip}) w'_{tip} \dot{u}'_{tip} \right] \delta w'_{tip} \\ & + g \left[ (1 + u'_{tip}) w'_{tip} \dot{w}'_{tip} - (w'_{tip})^2 \dot{u}'_{tip} \right] \delta u'_{tip} \end{aligned} \quad (154)$$

The terms associated with  $\delta w'_{tip}$  and  $\delta u'_{tip}$  are included in the Q vector and the numerical solution of Eq. (107) is used to determine the system displacements over time.

### 5.1.2 Model Validation

An energy balance is done at each time step to ensure the change in the energy of the system equals the work done by the motor torque and the friction forces. The work done by the motor torque is

$$W_{nc} = \int_0^t T \cdot \frac{d\Psi_{tip}}{dt} dt \quad (155)$$

Taking the time derivative gives

$$\dot{W} = T\dot{\Psi} = -g\dot{\Psi}^2 \quad (156)$$

This equation is combined with the work equation for friction forces Eq. (122) and the result is numerically integrated over time along with the displacement variables. At each time step, the numerical value of this work should equal the change in the total energy of the system. This check indicates the motor torque has been correctly included in the finite element model.

### 5.1.3 Simulations

The nonlinear finite element model is integrated forward in time including the effects of a tip motor. The control gain  $g$  for the feedback control law must be chosen and can be determined by several methods. For example, the finite element model can be linearized and control design methods e.g. a pole placement, quadratic regulator, etc. can be used, or the gain can be chosen by trial and error to give the desired damping. For this study, the trial and error method is used since it is simpler and the main focus of this

research is the recovery of model parameters and not on control design. Several gain values are used in the nonlinear finite element model and the resulting deformation shapes compared. Figure 23 and Figure 24 show the tip  $w$  and  $u$  displacements for different values of  $g$ .

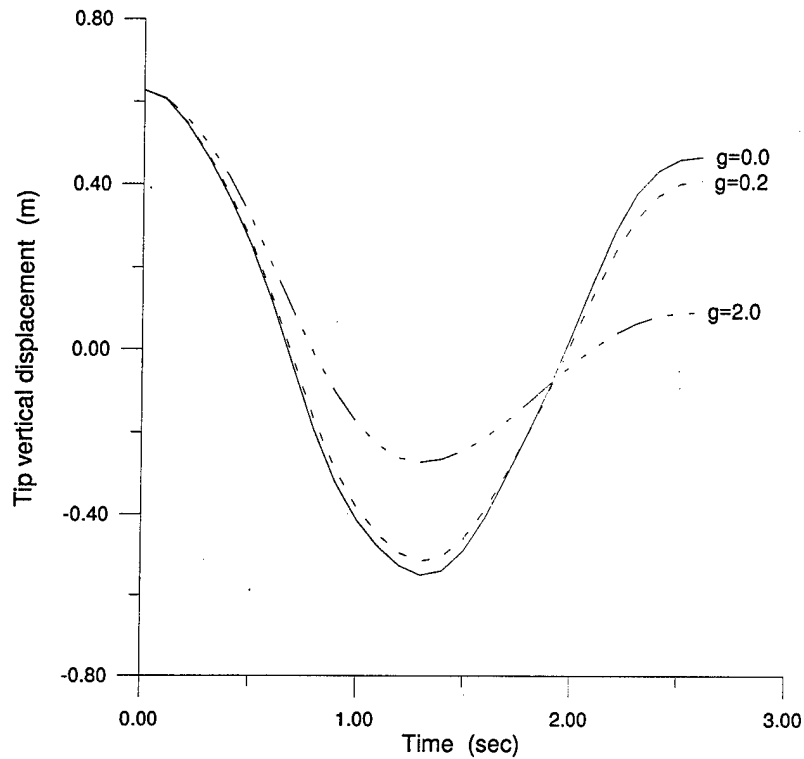
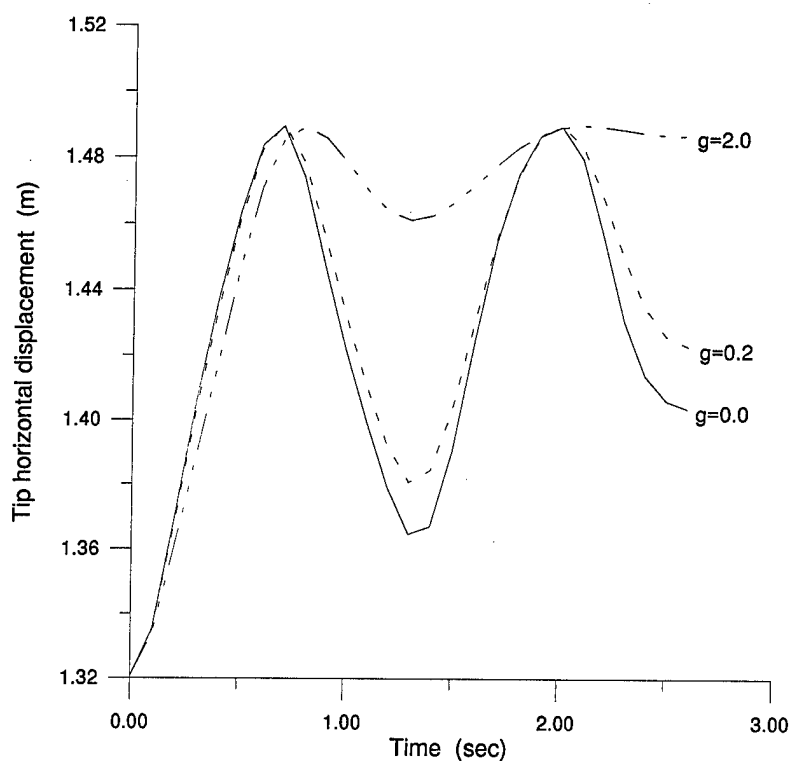
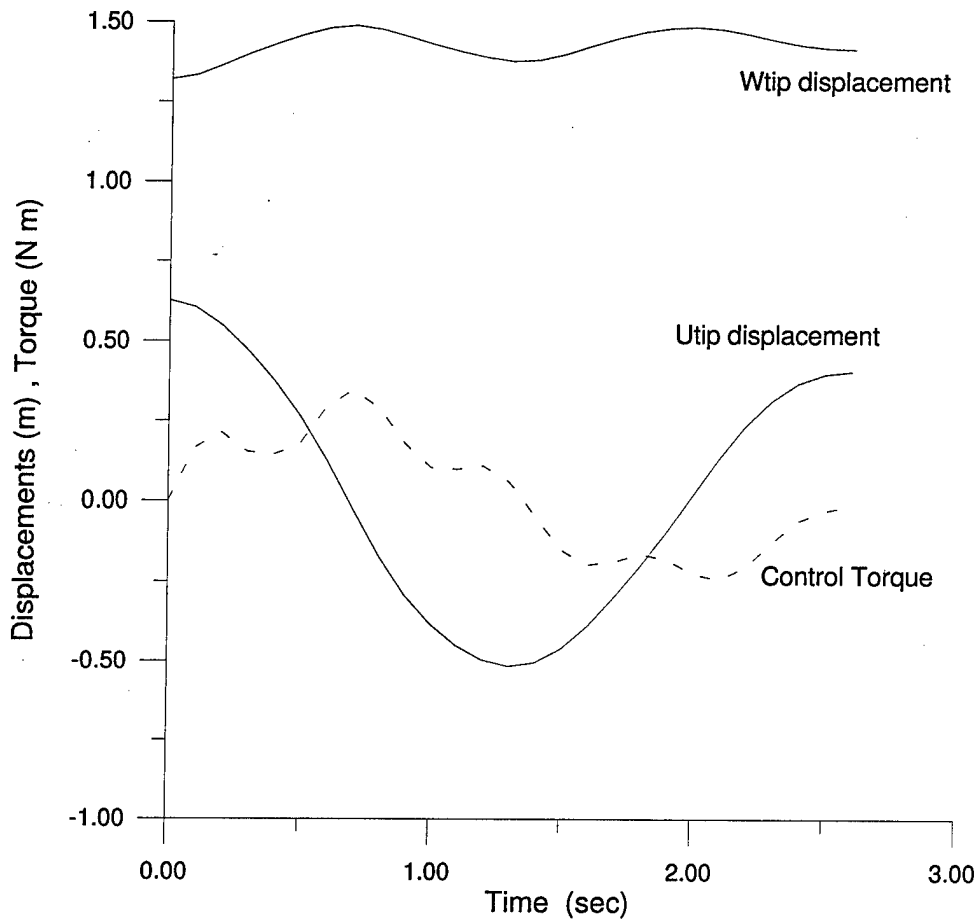


Figure 23. Effect of gain values on tip transverse displacements



**Figure 24. Effect of gain values on tip longitudinal displacements**

The higher control gain of 2.0 has the largest reductions in the tip deflections and brings the beam to rest quickly. However the torque needed to suppress the vibrations is large and beyond the operating bounds of a Maxon motor. The smaller control gain damps out the tip motions and generates torques within the bounds of the motor. The highest torque this gain requires is .35 N·m which corresponds to 49 oz-in. A plot of the tip displacements and the torque history for the control gain of 0.2 is shown in Figure 25.



**Figure 25. Control and tip displacements for control gain of 0.2**

An energy balance is performed at each integration step and the change in the total energy of the system equals the change in the work done by the motor torque and the friction forces. These values match to eight digits. The initial energy of the system is 2.2525729 N·m and after one period the energy change (and work done) equals 1.2967753 N·m.

## 5.2 Forced Vibration Parameter Estimation

The parameters affecting a forced response are related to the motor used on the system. The parameter recovered in this analysis is the ratio of the motor torque constant. If the torque constant is not well known, the torque generated by the motor is incorrect and

the effects on the recovered deformation shapes are used to recover the correct torque constant,  $K_t$ . If the torque constant is incorrect,  $\hat{K}_t$ , the current sent to the motor is incorrectly computed as

$$\hat{i}(t) = \frac{-g\dot{\Psi}}{\hat{K}_t} \quad (157)$$

The torque applied to the structure is not the desired torque, but an altered value related to the ratio of the true and estimated torque constants.

$$\hat{T} = r(-g\dot{\Psi}) \quad \text{where} \quad r = \frac{K_t}{\hat{K}_t} \quad (158)$$

This equation for the torque is used in the development of the nonconservative work done by the motor.

$$\begin{aligned} \delta W_{nc} = & -rg \left[ (1 + u'_{tip})^2 \dot{w}'_{tip} - (1 + u'_{tip}) w'_{tip} \dot{u}'_{tip} \right] \delta w'_{tip} \\ & + rg \left[ (1 + u'_{tip}) w'_{tip} \dot{w}'_{tip} - (w'_{tip})^2 \dot{u}'_{tip} \right] \delta u'_{tip} \end{aligned} \quad (159)$$

The  $\delta w'_{tip}$  and  $\delta u'_{tip}$  terms are included in the Q vector in the nonlinear finite element model represented by Eq. (107).

### 5.2.1 Least Squares Estimation

The least square procedure outlined in Chapter IV for the estimation of static parameters is used to estimate the motor torque constant ratio. The true torque constant is then estimated by a simple multiplication between  $r$  and the estimated torque constant.



To test these ideas, a set of 'true' measurements of the tip  $u_t$  and  $w_t$  deflections is simulated by integrating the differential equation in Eq. (107) including the motor model from Eq. (159) and a known value of the torque constant ratio. The recovery of the parameter  $r$  is started by estimating a value of  $r$  and integrating in time to the last measurement interval. The parameter value is updated using the sensitivity matrix and the difference between the measured and model tip deflections as developed previously.

$$r_{n+1} = r_n + (\Omega^T \Omega)^{-1} \Omega^T (\tilde{Y}_{meas} - \hat{Y}_{model}(r_n)) \quad (160)$$

The only real change in this parameter estimation process is in the calculation of the sensitivity matrix  $\Omega$ . In this case the sensitivity matrix is composed of one column since only one parameter is being recovered in this discussion. The rows are derivatives of the variables  $u_{tip}$  and  $w_{tip}$  with respect to  $r$  and evaluated at the measurement times. The sensitivity matrix is integrated in time to get the derivatives at the measurement times. The general form of the differential equation for the sensitivity matrix is the same as in Eq. (135). However, the implicit derivatives are different since including motor effects causes a dependence on the tip slopes and velocities in the  $Q$  vector. The implicit derivative matrix becomes

$$\frac{\partial f}{\partial v} = \left[ \begin{array}{c|c} 0 & \text{I} \\ \hline [M]^{-1}[CMULTI] \left[ \frac{\partial NLT}{\partial v_1} - \frac{\partial Q}{\partial v_1} \right] & [M]^{-1}[CMULTI] \left[ -\frac{\partial Q}{\partial v_2} \right] \end{array} \right] \quad (161)$$

Since  $Q$  only depends on  $w'_{tip}$ ,  $u'_{tip}$ ,  $\dot{w}'_{tip}$ , and  $\dot{u}'_{tip}$ , the derivative matrices  $\partial Q / \partial v$  are sparse matrices with few entrees. The explicit derivative matrix  $\partial f / \partial p$  is also different for the parameter  $r$ . It becomes

$$\frac{\partial f}{\partial r} = \left\{ [M]^{-1} \left[ \begin{array}{c} \{0\} \\ [CMULTI] \left\{ -\frac{\partial Q}{\partial r} \right\} \end{array} \right] \right\} \quad (162)$$

These derivative matrices are used in Eq. (135) for integrating the sensitivity matrix over time. The sensitivity matrix and the derivatives included in this matrix are checked via finite difference calculations at each time step and there is good agreement between them. This verifies the correct development and placement of the derivatives used in the integration of the sensitivity matrix. An estimate of the motor torque constant is used in the simultaneous numerical solutions of Eq. (107) and Eq. (135) with Eq. (159) used for the motor model. The parameters are then updated using Eq. (160). The numerical solution and updating process is repeated until the changes in the parameters are small.

#### *Measurement Errors*

The parameter recovery of the motor torque constant ratio can be altered to include the uncertainties in the measurement values. The same process is followed as the one used in the recovery of the static parameters. A weight matrix is included in the least square minimization function and the weights used are the reciprocal of the error variances for each measurement. The same parameter update formula is developed but the different sensitivity matrix is used in the equation as discussed in the previous section.

$$r_{n+1} = r_n + (\Omega^T W \Omega)^{-1} \Omega^T W (\tilde{Y}_{meas} - \hat{Y}_{model}(r_n)) \quad (163)$$

The measurement errors are mapped into the error in the recovered motor parameter using

$E_r = (\Omega^T W \Omega)^{-1} = \sigma_r^2$ . The error variance of the motor torque constant ratio reflects on how well determined this parameter is.

### Parameter Uncertainties

The estimated parameters and uncertainties from the previous static and free vibration analysis can be carried forward and combined with the recovery of parameters affecting the forced response. Measurement information is brought forward for a final level of parameter updating. This new recovery program will take advantage of well converged parameters and allow further adjustments to be made for ill converged parameters. The parameters are grouped by the recovery method used. The statically determined parameters are  $p_s = (EI_1, EI_2)$ , the parameters recovered by the free vibration analysis are  $p_{fr} = (\mu_b, \mu, \rho_1, \rho_2)$ , and the parameters recovered by the forced response are  $p_f = (r)$ . The previously determined parameters are treated as additional measurements

$$\begin{Bmatrix} \tilde{p}_s - \hat{p}_s \\ \tilde{p}_{fr} - \hat{p}_{fr} \end{Bmatrix} = \begin{bmatrix} \mathbf{I} & \mathbf{0} \\ \mathbf{0} & \mathbf{I} \end{bmatrix} \begin{Bmatrix} \Delta p_s \\ \Delta p_{fr} \end{Bmatrix} + \begin{Bmatrix} e_s \\ e_{fr} \end{Bmatrix} \quad (164)$$

This equation is combined with the forced vibration measurement error expression yielding

$$e_{tot} = \begin{Bmatrix} \tilde{Y}_{meas} - \hat{Y}_{model}(p) \\ \tilde{p}_s - \hat{p}_s \\ \tilde{p}_{fr} - \hat{p}_{fr} \end{Bmatrix} - \begin{bmatrix} \Omega_f & \Omega_s & \Omega_{fr} \\ 0 & \mathbf{I} & 0 \\ 0 & 0 & \mathbf{I} \end{bmatrix} \begin{Bmatrix} \Delta p_f \\ \Delta p_s \\ \Delta p_{fr} \end{Bmatrix} \quad (165)$$

An overall weight matrix is made by combining the variance matrix  $W$  of the forced vibration measurements and the covariance matrix  $E_s$  of the static parameters and the covariance matrix  $E_{fr}$  of the free vibration parameters:

$$\Lambda = \begin{bmatrix} W & 0 & 0 \\ 0 & E_s & 0 \\ 0 & 0 & E_{fr} \end{bmatrix}$$

The weighted least squares minimization yields an update for the parameters

$$\begin{Bmatrix} \Delta p_f \\ \Delta p_s \\ \Delta p_{fr} \end{Bmatrix} = (A^T \Lambda A)^{-1} A^T \Lambda \begin{Bmatrix} \tilde{Y}_{meas} - \hat{Y}_{model}(p) \\ \tilde{p}_s - \hat{p}_s \\ \tilde{p}_{fr} - \hat{p}_{fr} \end{Bmatrix} \quad \text{where } A = \begin{bmatrix} \Omega_f & \Omega_s & \Omega_{fr} \\ 0 & I & 0 \\ 0 & 0 & I \end{bmatrix} \quad (166)$$

This combined parameter update allows the measurements and covariance estimates for all the parameters to influence the final determination of the static, free vibration, and forced vibration model parameters.

### 5.2.2 Results - Forced Vibration Parameters

A set of 'true' measurements of the tip locations are simulated by integrating the nonlinear finite element model Eq. (107) using a known value of the torque constant ratio in Eq. (159). Any known value of the torque constant ratio can be used and a value of  $r = 1$  is chosen since simulated measurements are available from previous work. The values of  $w_t$  and  $u_t$  are taken at five time intervals over one quarter cycle for a total of ten measurements. The starting estimate of the parameter is made by decreasing the torque constant ratio by 20%. The nonlinear finite element model is integrated to the measurement times and the resulting model values are used in Eq. (160) to update  $r$ . Table 22 summarizes the results of the recovered torque constant ratio.

True value	1.0000
Starting Estimate	0.8000
Value after 1 iteration	0.9872
Converged value	0.9999

The ratio recovered after one iteration is very close to the true value and is essentially the same after two iterations. The 'true' torque constant is recovered quickly and accurately when measurement errors are neglected.

#### *Measurement Errors*

Errors are introduced into the simulated measurements using a Gaussian random number generator and an associated standard deviation for each value. These standard deviations range from 0.0008 to 0.0020 for the  $w_t$  and  $u_t$  measurements. The parameter recovery program is repeated using the weighted measurements. Table 23 shows the resulting torque constant ratio recovered.

True values	1.0000
Initial estimate	0.8000
Recovered value	0.9567
Recovered $\sigma$	0.0514

The torque constant ratio is recovered after two iterations and is within 4% of the true value. The standard deviation for this parameter is small and indicates this ratio is well determined.

## CHAPTER VI

### CONCLUSIONS

In this dissertation, several nonlinear static and dynamical models for large deformations of flexible body chains have been investigated. A novel formulation is introduced for nonlinear beam static deformations using arc length as the independent spatial variable. This formulation is validated by comparison to several published solutions and experiments. For transient dynamic response, a geometrically exact finite element model is developed from a static model proposed by Epstein and Murray.

The focus of this dissertation is the development of a three step approach to system identification:

1. A series of static deformation experiments are used to recover the parameters affecting the potential energy stored by the beams.
2. The beam system is released from the statically deformed position and free response measurements are used to recover the inertia type parameters.
3. A forced response experiment is used to recover actuator model parameters. Measurement and *a priori* covariance estimates can be propagated through the sequence of parameter recoveries.

Based on the results of this approach, the following conclusions are drawn.

1. The beam parameters affecting the potential energy of the system can be quickly and accurately recovered using the arc length model and a family of deformation shapes from two types of static experiments. The stiffness coefficients are well determined in the presence of measurement errors for appropriately designed experiments. The stiffness coefficient of the first beam is better determined since the portion of the system closest to the clamped boundary condition deforms the most and parameters affecting that response are more easily estimated.

2. The beam parameters affecting the free response of the system can be recovered using a nonlinear finite element model and the observed motion due to the release of the constraining wire from the static experiment. The coefficients of the friction forces between the tip and elbow masses and the supporting table are well determined with and without the presence of measurement errors. The mass density per unit length for each beam can be determined assuming perfect measurements but are difficult to recover in the presence of measurement errors unless large external (e.g. friction) forces are present. The mass densities do not have a large affect on the free, lightly damped motion of the system and are difficult parameters to determine. The parameters in the second beam are better estimated than the parameters in the first beam for this clamped/free system due to larger dynamic motion at the tip of the system.
3. The motor parameters affecting the forced response of the system can be recovered using the nonlinear finite element model and the measured response over a short transient. For the cases studied, motor torque constants are well determined in the presence of realistic measurement errors.
4. The sequential process permits the dimensionality of the estimation process to be increased as more information is available thus enhancing convergence in high-dimensional parameter estimation processes.

Several difficulties were encountered and I suggest the following issues for further investigation:

1. The arc length approach works well for the nonlinear static analysis but cannot be easily extended to the dynamic analysis under general modeling assumptions. The nonlinear finite element model could be used to recover the potential energy parameters for model consistency in bringing forward the recovered parameters and their associated uncertainties.
2. The nonlinear finite element model works well for simulating the dynamic response and recovering the free and forced vibration parameters. However, a small time step must be used for the stability of the numerical integration which

leads to a large amount of computer time for tracking the motion over a long time period. Optimization of the computer code and variable time steps could be used to shorten the amount of computer time needed. Some new method is needed to do order reduction for this class of problems.

3. A method for carrying forward the parameter estimates and uncertainties in the sequence of parameter recovery experiments has been developed. Simulation studies of this process at each step needs to be further investigated.



## REFERENCES

1. Kwak, M.K., Smith, M.J., Das, A., "PACE: A Test Bed for the Dynamics and Control of Flexible Multibody Systems," The USAF Phillips Laboratory, OLAC PL/VTSS, Edwards AFB, CA.
2. Kwak, M.K., Meirovitch, L., "New Approach to the Maneuvering and Control of Flexible Multibody Systems," *Journal of Guidance, Control, and Dynamics*, Vol. 15, No. 6, 1992, pp. 1342-1353.
3. Meirovitch, L., Lim, S., "Maneuvering and Control of Flexible Space Robots," *Journal of Guidance, Control, and Dynamics*, Vol. 17, No. 3, 1994, pp. 520-528.
4. Hinnant, H.E., Hodges, D.H., "Nonlinear Analysis of a Cantilever Beam," *AIAA Journal*, Vol. 26, No. 12, 1988, pp. 1521-1527.
5. Hodges, D.H., "Proper Definition of Curvature in Nonlinear Beam Kinematics," *AIAA Journal*, Vol. 22, No. 12, 1984, pp.1825-1827.
6. Monasa, F., Lewis, G., "Large Deflections of Point Loaded Cantilevers with Nonlinear Behavior," *Journal of Applied Mathematics and Physics (ZAMP)*, Vol. 34, Jan. 1983, pp.124-130.
7. Swokowski, E. W., *Calculus with Analytic Geometry*, Prindle, Weber & Schmidt, Inc., Boston, MA, 1975, pp. 578-580.
8. Reddy, J.N., Singh, I.R., "Large Deflections and Large-Amplitude Free Vibrations of Straight and Curved Beams," *International Journal for Numerical Methods in Engineering*, Vol. 17, 1981, pp. 829-852.
9. Epstein, M., Murray, D.W., "Large Deformation In-plane Analysis of Elastic Beams," *Computers and Structures*, Vol. 6, No. 1-A, 1976, pp.1-9.
10. Dowell, E.H., Traybar, J., and Hodges, D. H., "An Experimental-Theoretical Correlation Study of Non-linear Bending and Torsion Deformations of a Cantilever Beam," *Journal of Sound and Vibration*, Vol. 50, No. 4, 1977, pp.533-544.
11. Hodges, D.H. and Dowell, E.H., "Nonlinear Equations of Motion for the Elastic Bending and Torsion of Twisted Nonuniform Rotor Blades," NASA TN D-7818, Ames Research Center, Moffett Field, CA, Dec. 1974.

12. Romero, I., "Design, Construction and Testing of a Release Actuator for the Planar Articulating Controls Experiment," M.S. Thesis, Texas A&M University, College Station, TX (1994).
13. Junkins, J. L., *An Introduction to Optimal Estimation of Dynamical Systems*, Sijthoff & Noordhoff Int. Publishers, Alphen aan den Rijn, The Netherlands, 1978.
14. McVay, M.W., "Large Static and Dynamic Deformation of Beams: the Inverse Problem", Technical Report No. TAMU AERO 96-07-04, Department of Aerospace Engineering, Texas A&M Univ., College Station, TX, July 1996.
15. Craig, R. R., Jr., *Structural Dynamics*, John Wiley and Sons, Inc., New York, NY, 1981.
16. Greenwood, D. T., *Principles of Dynamics*, Prentice-Hall, Inc., Englewood Cliffs, NJ, 1988.
17. Skelton, R. E., "Cost Decomposition of Linear Systems with Application to Model Reduction," *International Journal of Control*, Vol. 32, No. 6, 1980, pp. 1031-1055.
18. Beer, F. P., Johnston, E. R., Jr., *Mechanics for Engineers*, McGraw-Hill, Inc., New York, NY, 1976.
19. Higdon, A., Ohlsen, E. H., Stiles, W. B., Weese, J. A., and Riley, W. F., *Mechanics of Materials*, McGraw-Hill, Inc., New York, NY, 1976.
20. Hurtado, J. E., "Experiments on Vibration Suppression of a Flexible Planar Grid," M.S. Thesis, Texas A&M Univ., College Station, TX, August 1991.
21. Koren, Y., *Computer Control of Manufacturing Systems*, McGraw-Hill Inc., New York, NY, 1983.

## VITA

Name: Matilda Wilson McVay

Address: 3107 Westchester Ave.  
College Station, Texas 77845

Family: Parents: Connie L. and Robbie T. Wilson  
Husband: Duane A. McVay  
Children: Renee C. McVay  
Paul R. McVay  
Karen J. McVay

Education: B.S., Petroleum Engineering (May 1981)  
Colorado School of Mines, Golden, Colorado

M.S., Petroleum Engineering (December 1982)  
Texas A&M University, College Station, Texas

Ph.D., Aerospace Engineering (August 1996)  
Texas A&M University, College Station, Texas

Experience: Sr. Project Engineer, Exxon Company, USA (1982-1986)